Integrated Microfluidics, Heaters, and Electronic Sensors for Lab-On-A-Chip Applications

by

Tzu Liang Loh

B.S.E. Mechanical Engineering
University of Michigan, 2002

Submitted to the Department of Mechanical Engineering
in partial fulfillment of the requirements for the degree of

Master of Science in Mechanical Engineering

at the

MASSACHUSETTS INSTITUTE OF TECHNOLOGY

May 2005 [June 2005]

Author .....
Department of Mechanical Engineering
May 19, 2005

Certified by ....
Scott Manalis
Associate Professor, Biological Engineering
Thesis Supervisor

Read by .....
Kimberly Hamad-Schifferli
Assistant Professor, Mechanical Engineering and Biological Engineering
Thesis Reader

Accepted by ....
Lallit Anand
Chairman, Department Committee on Graduate Students

Integrated Microfluidics, Heaters, and Electronic Sensors for Lab-On-A-Chip Applications

by

Tzu Liang Loh

Submitted to the Department of Mechanical Engineering
on May 19, 2005, in partial fulfillment of the
requirements for the degree of
Master of Science in Mechanical Engineering

Abstract

Microfluidics, microfabricated suspended heaters and electronic field effect sensors have been successfully integrated on a single device chip. This integration enables spatial cycling of as little as $11nL$ of reagents over different thermally isolated temperature zones, to be coupled with the field effect sensing capabilities, for label-free detection of biomolecules such as DNA. The microfluidic valves provide control over reagent flow, and flow rates of up to $1.8nLs^{-1}$ have been demonstrated with the on-chip pumps.

Initial characterization of the suspended heaters was successfully carried out using thermochromic crystals. Functionality of the heaters was shown and a rough calibration was obtained. The subsequent implementation of temperature measurement using fluorescent dyes, enabled real-time spatial temperature mapping. This method demonstrated the capability of monitoring fluid temperatures in microfluidic channels with $5°C$ accuracy at $2\mu m^2$ resolution. Thermal isolation of the suspended heaters was clearly observed from the steep gradients in the spatial temperature profiles captured. Finally, localized boiling of water in the microfluidic channels was achieved, with only $30mW$ supplied to the heaters.

In order to evaluate the sensors, tests were carried out to determine its sensitivity to surface charge. Buffer solutions of different pH were injected, and the sensors have been able to measure pH values ranging from $2.2 - 7.4$ and demonstrate sensitivity of up to $38.8mV$ per pH unit change. Highly charged poly-electrolytes were also investigated as model systems to validate sensor detection of charged biomolecules. The adsorption and layer-by-layer deposition of multiple poly-electrolyte layers to the sensor surface have been successfully detected.

This device paves the way for future integration of multiple microfluidic components, for lab-on-a-chip applications.

Thesis Supervisor: Scott Manalis
Title: Associate Professor, Biological Engineering

Acknowledgments

This thesis marks the end of my academic career (for now), through all the struggles and triumphs. It has been an unbelievable journey since I first left home more than five years ago, and I feel extremely fortunate. I am deeply grateful for the love, care and support that my parents, Wan Yin Chan and Loh Kah Yit, have lavished upon me, from half a world away. They have taught me much, directly and indirectly, and have inspired me to constantly strive forward. Thank you.

I thank my advisor, Professor Scott Manalis, for giving me this great opportunity to work in the Nanoscale Sensing Group. He has provided much support and guidance, that has greatly contributed to the success of this project.

I also thank my thesis reader, Professor Kimberly Hamad-Schifferli, for her valuable input. I greatly appreciate her support and patience throughout the process.

My time in the Nanoscale Sensing Group interacting with my amazing lab-mates, from such diverse backgrounds, has proven to be most rewarding. Dr. Nebojsa "Neebo" Milovic and Dr. Paul Ashby have been crucial in providing guidance over the course of the project. It has also been wonderful to work and have fun with everyone in the group — Dr. Leo Alexopoulos, Dr. Michel "Meekah" Godin, Dr. Andrew "xXx" Sparks, Dr. Christine Tsau, Thomas Burg, Rumi Chunara, Johnson Hou, Victor "Victoid" Lellyveld, George Porpescu, Maxim Shusteff, and Peter Russo. Without their expertise and unlimited help, the great success of the project would not have been possible.

Dr. Raj Chakrabarti, Dr. Antonia Maria Rojas, and Eugene Antipov have also provided much assistance in the project, which I greatly appreciate.

This project was a continuation of the work done for the Fall 2003, Microfabrication Project Laboratory class, together with Brian Chow, Tyrone Hill, Johnson Hou, David Kong, Manu Prakash, and Brian Tang. It was a great experience working with them, and I thank them for giving me a big boost. Professor Martin Schmidt and Scott jointly taught the class and they have provided much guidance that was vital to the project.

The contribution of the MIT Microsystems Technology Laboratories staff, particularly Dr. Vicky Diadiuk, Dr. Li-Wen Wang, Dan Adams, Bob Bicchieri, Kurt Broderick, Dave Terry, and Paul Tierny, has been invaluable. Linhvu Ho, and Chiang Juay Teo have also generously shared their experience, in helping me with the practical aspects of fabrication.

In staying in touch with my core mechanical engineering discipline, Jerry Wentworth and Mark Belanger have patiently coached me when I had to machine parts in the Laboratory for Manufacturing and Productivity machine shop.

Efficient administrative assistance, provided by Tracy Skeete, Michael Houlihan, Sherry Lassiter, Susan Murphy-Bottari, and John Difrancesco, was essential for the proper working from day to day.

This research has been funded by Hewlett-Packard Corporation.

The actual thesis typing has been made much more enjoyable with the help of Henry Choy, Andrew Sparks, and Roger Yeh, in showing me the ropes of LaTex.

Finally, I extend my sincere gratitude, to my relatives and friends, who have supported and accompanied me throughout this amazing experience — Wan Tung Han, Wan Kum Tho, Varian Lim Choon Lik, Ng Kwanjee, Quek Boon Kiat, Liew Mei Moi, Peter Wong Sheow Yit, Woon Soon Keat, Juliana Kua Shu Tan, Soo Sze Min, Mindy Teo, Seetoh Kin Choong, Elizabeth Chee, Tan Li Leng, Yeo Kuang Liang, Au Hin Meng, Poh Sec Chun, Yiling, Trevor Ng Shang Kuan, Lindsay Wai, Najib Wong, Maisy Wong, Leonard Lee, Ketty Tanizar, He Ruijie, Angela Ho Wei Ling, Palex Ang Wee Horng, all the KK crew, Lynn Chua Shu Xian, Wallace Wong Dazheng, Amanda Ang Jiaming, *and the list goes on...*

Contents

List of Figures

List of Tables

Chapter 1

Introduction

1.1 Motivation

Lab-on-a-chip devices are an appealing vision for the miniaturization of bulky test equipment into portable, hand held devices that can be used for point-of-care diagnostics as well as field applications. This has a wide range of uses from environmental monitoring, pathogenic detection in the food industry, to agriculture and military applications.

Current sensor technology for detection of biomolecules are dependent on tagging target molecules with fluorescent or radioactive labels. These methods have been well established and are highly sensitive to small numbers of molecules. However, high quality optics, which are necessary for such high sensitivity measurements, are inherently bulky. It is extremely difficult to miniaturize such systems without compromising on the fidelity of the detection system. Therefore it is extremely advantageous to develop a label-free detection method that does not require additional optics. The field effect sensors developed by Cooper [6] and Russo [16] have demonstrated the detection of the intrinsic charge of biomolecules, and the resultant electrical signal output has been successfully measured.

The next step was then to incorporate an amplification stage upstream of the sensors. This amplification would increase the overall sensitivity of the device, while acting as a initial stage filter. In particular, DNA was chosen as a target for the

device because of its wide spread biological applications. This device would be the first device to carry out amplification and label-free detection of DNA on a single chip.

The initial design was provided by work done in the *Fall 2003, Microfabrication Project Laboratory class (6.151)* [5]. The goal of this thesis was to complete the fabrication and packaging of the device, to characterize the device, and to iterate on the design, in order to improve on performance characteristics.

1.2 Background

The field effect sensors are based on the electrolyte-insulator-semiconductor (EIS) structure, which were pioneered by Bergveld [1, 2], who developed the ion-sensitive field-effect transistor (ISFET). In this structure, the modulation of the silicon depletion region is measured by the lateral conductance of the silicon below the gate region. The measurement of electrical activity in muscle fibres was demonstrated in this early use of ISFETs. Alternately, the electrolyte-insulator surface potential can be measured with an EIS capacitor, as demonstrated by Siu et al. [18]. Finally, the field effect sensors were successfully applied to detect deposition of charged polymer layers as well as DNA, by Fritz et al. [8]. This sensor was then redesigned and integrated with microfluidics by Russo [16].

The miniaturization of analytical methods by developing micro devices has been an important trend, as noted by Kricka et al. [11]. The main goal of this work is to develop a lab-on-a-chip with complete sample-to-signal solutions. In particular, much effort has been put into miniaturizing of genetic testing to carry out polymerase chain reaction (PCR) on chip.

There are two main types of PCR devices being developed. Spatially cycled PCR, in continuous-flow PCR devices, such as the one developed by Kopp et al. [10], are simple in design. Temporally cycled PCR, on the other hand is often carried out using peltier thermoelectric elements, as demonstrated by Khandurina et al. [9]. A more elaborate PCR device, incorporating on-chip pumps and valves, has also been

successfully developed by Liu et al. [14].

However, all the integrated systems that have been developed so far rely on fluorescence optical readouts as detection methods (Burns et al. [3], Lagally et al. [12]).

Therefore, there is a urgent need for an integrated device that incorporates DNA amplification with label-free detection. This would enable the coupling of a powerful amplification tool with a sensitive and direct detection method, taking one step closer to the ultimate goal of a lab-on-a-chip.

1.3 Thesis Outline

This thesis will present the integration of microfluidics, microfabricated suspended heaters and electronic field effect senors onto a single device chip. The initial work for this integrated device was carried out as part of the *Fall 2003, Microfabrication Project Laboratory class (6.151)*. The initial theory, design, and fabrication process development was completed for the class. The actual fabrication of the first batch of devices was also carried out together with Brian Chow, Tyrone Hill, Johnson Hou, David Kong, Manu Prakash, and Brian Tang. This thesis continues to progress the accomplishments of the class project. In particular, the fabricated silicon chip was integrated with microfluidics and packaged. Instrumentation was assembled and systems were developed to characterize the individual components of the device.

Details of the theory behind the suspended heaters are discussed in Chapter 2. Chapter 3 discusses the initial design of the device and the improvements implemented after initial testing. These improvements were critical to increased yield of packaging and the robustness of the final devices. The fabrication and packaging of the device is described in Chapter 4. This includes the development of tools to improve fabrication and alignment of elastomer microfluidic chips. Chapter 5 details, the experimental setups, test parameters, and results of characterizing each of the individual components for the integrated device. The implementation of real-time spatial mapping of fluid temperature in microfluidics, is also reported in this chapter. Finally, Chapter 6 summarizes the accomplishments, and possible future work is discussed.

Chapter 2

Theory

The integrated device comprises microfluidics, field effect sensors, and integrated heaters. The theory behind the microfluidic components are discussed by Unger et al. [19] and Chou et al. [4]. The theory behind the field effect sensors have also been explored by Russo [16]. This is discussed in Section 2.1 together with the simulation done to determine the required process parameters. The heaters were developed as part of the *Fall 2003, Microfabrication Project Laboratory class (6.151)* [5] and the details are discussed in Section 2.2.

2.1 Field Effect Sensors

The sensors are a pair of lightly doped silicon field effect capacitors, where the capacitance of each sensor is determined by the sum of the oxide thickness and the depletion width in the silicon. Since the depletion region can be modulated by the charge on the sensor surface above the silicon oxide layer, the change in capacitance can be used to measure the change in surface potential. As shown in Figure 2–1, the binding of charged molecules can modulate the depletion region. Therefore this binding event can be directly detected by monitoring the capacitance of the sensors.

Simulation on SUPREM was carried out in the *Fall 2003, Microfabrication Project Laboratory class (6.151)* [5] to determine the process parameters that would result in the desired doping concentrations for both the sensors and heaters. The $P++$ boron

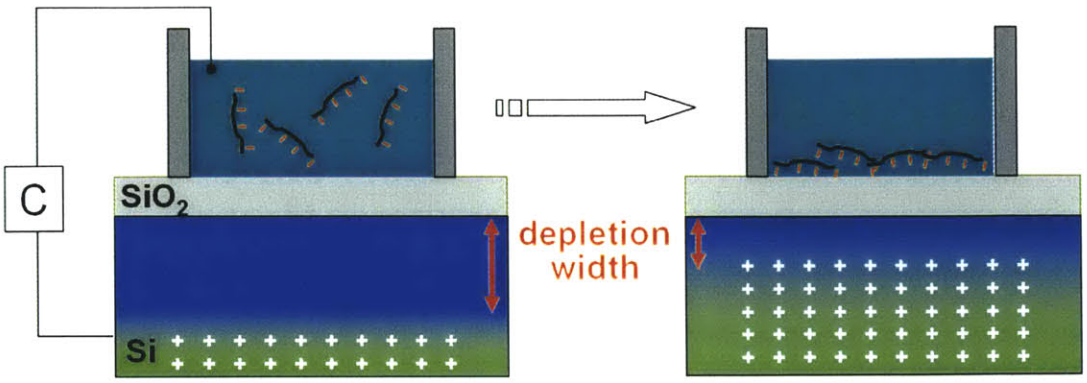

Figure 2–1: Schematic of the field effect sensors in an EIS structure, showing low capacitance with no binding of charged molecules(left) and higher capacitance and thus detection of molecular binding (right).

doping had to be above $5 \times 10^{19} cm^{-3}$ for the implanted heaters to serve as an etch stop. Conversely, the P implant for the sensors had to be low in order to increase the sensitivity and dynamic range of the sensors. The post-anneal implant profiles of the dopants are shown in Figure 2–2, and the process parameters are shown in Table 2.1. The annealing was carried out at $1050°C$ for $70min$, in an inert nitrogen environment.

Implant Species	**Dose**	**Energy** $[keV]$	R_p $[\mu m]$
Boron, $P++$	1×10^{16}	100	0.3
Boron, P	5×10^{12}	100	0.3
Phosphorous, $N++$	5×10^{15}	125	0.2

Table 2.1: *Implant Parameters for Silicon Doping*

2.2 Suspended resistive heaters

The resistive heaters are fully suspended on a $1\mu m$ thin nitride membrane to maximize the heat transfer to the reaction mixture, and to reduce the heat loss to the substrate. This allows for well defined temperature zones, while reducing the power required to be supplied to the heaters. A variety of heater designs were modeled to determine the optimal geometry.

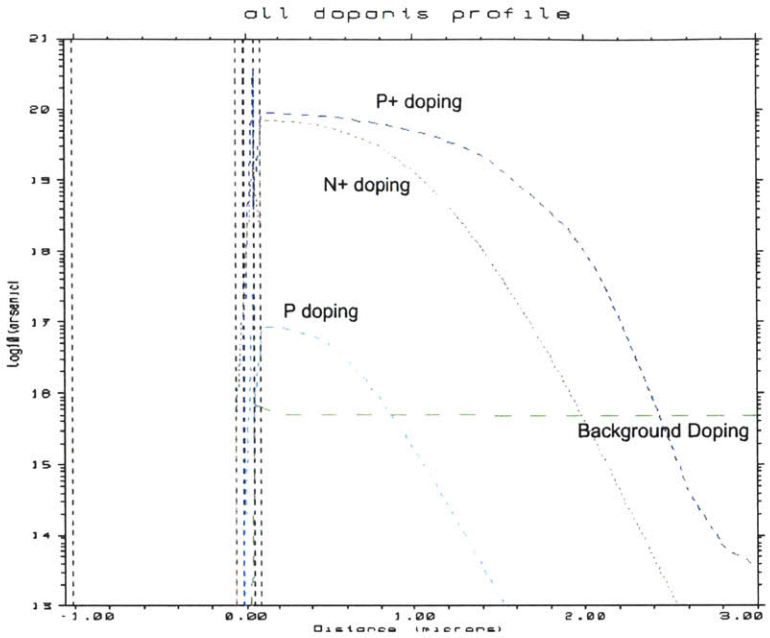

Figure2–2: Simulated doping profiles.

Lumped thermal modeling was carried out to determine the transient response of the heaters. Radiation was ignored in the analysis and the equations used in the analysis are shown below:

$$C_t = C_m l w t \rho_m \tag{2.1}$$

Where C_t is the heat capacity, l is the length, w is the width, t is the thickness, ρ_m is the mass density, and C_m is the specific heat capacity.

$$R_t = \frac{L}{K \cdot A} \tag{2.2}$$

Where R_t is the thermal resistance of the material block, L is the length of the structure, K is the thermal conductivity, and A is the cross sectional area.

$$T = I^2 R_e R_T \tag{2.3}$$

Where T is the temperature, I is the heat flux, R_e is the electrical resistance of the system, and R_T is the total thermal resistance.

The equivalent circuit of the lumped thermal model was constructed, as shown in Figure 2–3. The material thermal properties used are shown in Table 2.2, and the resultant lumped capacitance and resistance values used in the model are shown in Table 2.3 .

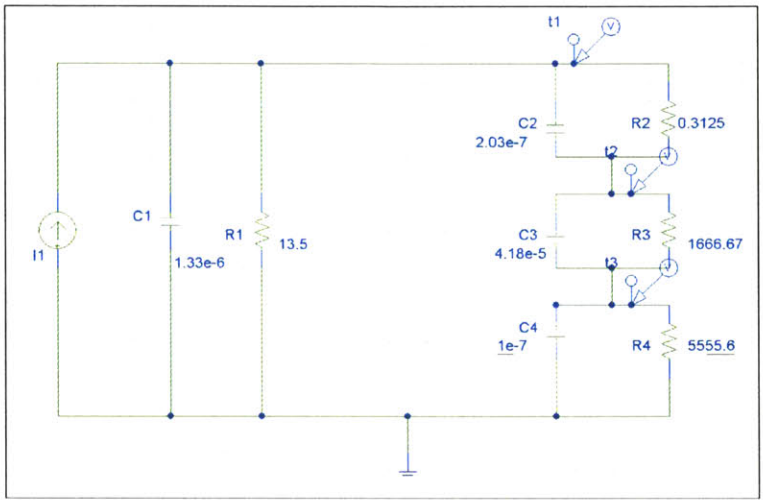

Figure 2–3: Equivalent circuit of the lumped thermal model. C_t and R_t represent the heat capacity and thermal resistance of the materials.

Material	**Thermal Conductivity,** $K\ [Wm^{-1}K^{-1}]$	**Specific Heat Capacity,** $C\ [Jkg^{-1}K^{-1}]$
Doped Silicon	148	712
Silicon Nitride	32	750
Water	0.6	4184
PDMS	0.18	705.6

Table 2.2: *Material thermal properties*

The model was subjected to a heat flux of $200\mu s$ square wave of $20 - 87°C$. The results of the lumped model simulation revealed extremely fast response time constants for the heating and cooling of the fluids, at $6.3\mu s$ and $6.4\mu s$ respectively. The heater and nitride membranes had similar response time constants at $5.9\mu s$ for heating and $6.5\mu s$ for cooling. The full response is shown in Figure 2–4.

FEMLAB and ANSYS were used for finite element modeling. The complete 3D geometry was modeled, and a 2D cross section profile is shown to represent the

Element	Value
C_{heater}	1.6×10^{-8}
R_{heater}	67.6
$C_{nitride}$	2.03×10^{-8}
$R_{nitride}$	3.12
C_{water}	4.18×10^{-7}
R_{water}	1.6×10^{3}
C_{PDMS}	6.7×10^{-7}
R_{PDMS}	5.55×10^{5}

Table 2.3: *Lumped model element values*

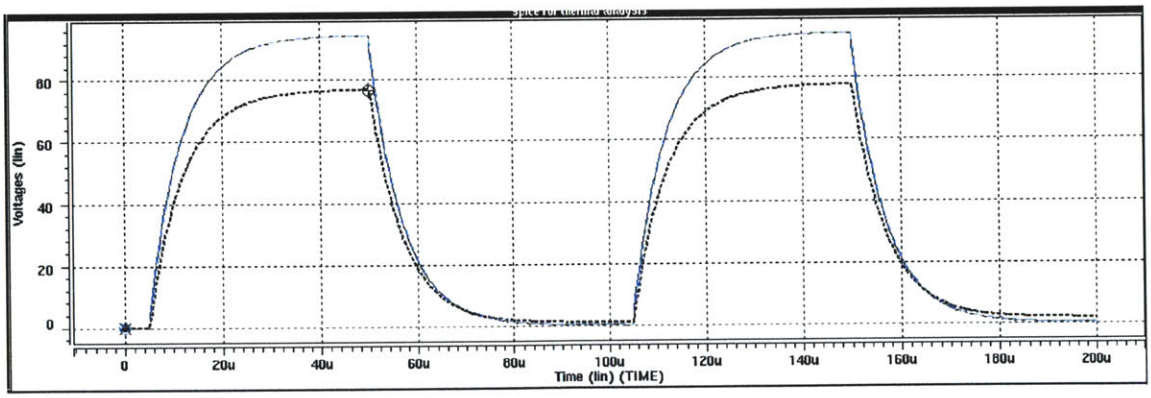

Figure2–4: Transient response of the lumped thermal model for the heaters, showing the heater temperature in blue (top) and the fluid temperature in black (bottom).

temperature profile. The fluid flow was ignored, in order to simplify the simulation. The thermal analysis considered fluid convection and radiative heat loss from the nitride membrane. As a result, a steady state thermal profile was obtained.

The resultant temperature profile for the design with heaters aligned perpendicular to the flow axis is shown in Figure 2–5. The profile along the flow axis reveals a highly non-uniform profile with large temperature gradients along the flow axis. Therefore, the fluid would be exposed to this fluctuation in temperature as it flows across the heaters, which is undesirable.

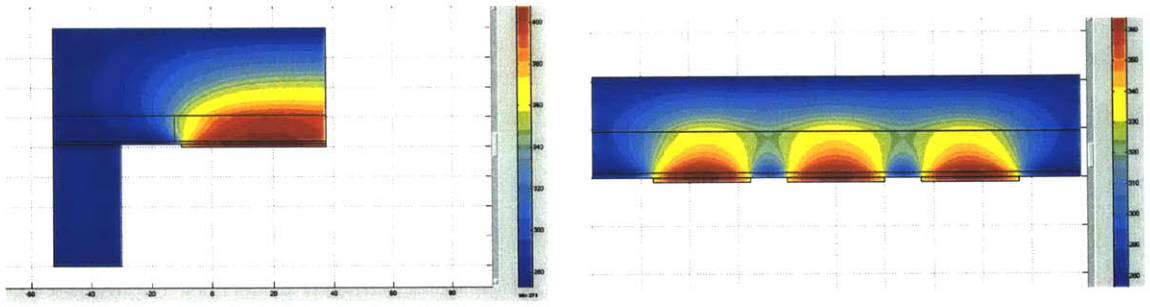

Figure 2–5: Simulated temperature profiles for heaters that lie across the flow axis. The cross section of the channel is shown on the left and the profile along the flow axis is shown on the right.

A design with heaters aligned parallel to the flow axis was subsequently chosen. The temperature profile along the flow axis would be more uniform since the heaters lay on the same axis. Although there is temperature variation across the cross section of the channel, each element of fluid flowing over the heaters would see a uniform temperature. This would be more ideal compared to the previous design. The temperature profile for the design with three heaters aligned parallel to the fluid flow axis is shown in Figure 2–6.

The results from the simulation have helped to determine that the heaters should lie along the flow axis. This was applied to the design of the heaters for the device.

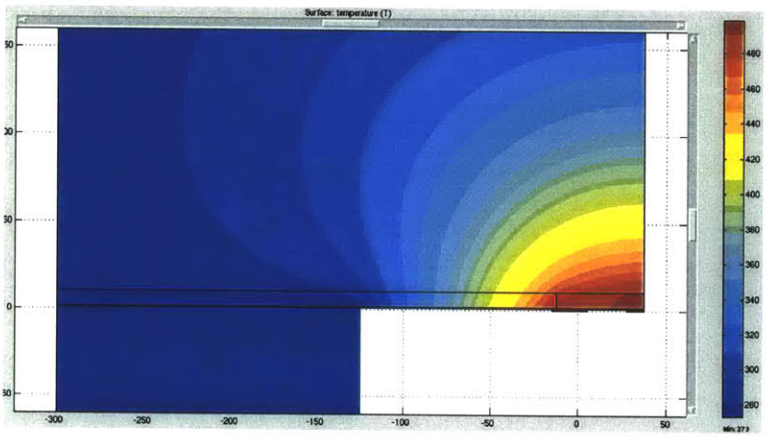

Figure2–6: Simulated temperature profile for heaters parallel to flow axis.

Chapter 3

Device Design

The integrated device incorporates microfluidics (channels, valves, and pumps), suspended resistive heaters, and electronic field effect senors on a single chip. The architecture was inherited from the *Fall 2003, Microfabrication Project Laboratory class (6.151)* [5], and modifications have been made to improve the device characteristics, as well as to increase ease of assembly and packaging.

3.1 Microfluidics

Integrated microfluidics allows flowing and manipulating fluids on the integrated device. The microfluidic dies are first fabricated independently and then integrated with the silicon chip afterwards.

3.1.1 Initial design

The microfluidic devices consist of a double layer PDMS stack. The fluidic channels are in the bottom layer, with channel heights of about $10\mu m$. The control channels are in the top layer and are about $100\mu m$ tall. The two layers are separated by a thin membrane of $10\mu m$ thickness.

All the channels were $100\mu m$ wide and are spaced at least $100\mu m$ apart. The layout of the devices are shown in Section B.1.1.

3.1.2 Improved design with on-chip degassing

During the initial tests of the microfluidic systems, the permeability of air in PDMS became evident. Once the valves or pumps were pressurized, air bubbles would start to form in the fluidic channels at the membranes. This bubble formation would render the device completely useless because the presence of air in the sample loop would most likely disrupt the PCR reaction. Air bubbles would also cause spikes in the signal detected by the sensors and the measurements would then be inaccurate.

In order to arrest the problem of bubble formation in the fluidic channels, the control lines were filled with degassed water. However this only delayed the formation of bubbles. Basically, the air defuses into the column of water during pressurization. However when the pressure is released, the dissolved air does not completely defuse back out. Over time, the plug of dissolved air travels down the column of water and eventually gets released into the fluidic channel.

Therefore, additional channels were added to both layers. These channels act as vacuum lines such that the plug of dissolved air can escape out of the water before it reaches the fluidic channels.

Also, pressurized helium is used in place of nitrogen. Helium was chosen because the solubility of helium in water is lower than most other gasses, as demonstrated by Leach et al. [13]. The mole fraction solubility of helium is 0.708×10^{-5} as compared to 1.177×10^{-5} for nitrogen, as summarized by Scharlin et al. [17]. It also defuses faster through water and PDMS. This allows the helium to escape into the vacuum lines effectively.

The addition of channels in the valve layer also allows on-chip degassing of the sample fluids, when a vacuum is applied. The layouts are shown in Section B.1.2.

Implementation of the design improvements solved the problem of bubble formation. However, there were some shortcomings to the design. The additional lines added to degas the fluidic layer were large windows of thin membranes. These membranes were very flexible and contribute to variation of the volume of fluid under the membranes. This variation affected the optical properties during fluorescent mea-

surements. Also, the large membranes were the most susceptible to failure when the device is exposed to large pressure build ups.

Another problem was that the vacuum lines for degassing the valve layer were placed too close to the fluidics lines. This made the device more susceptible to delamination and failure of the PDMS-silicon nitride bonding.

3.1.3 Final design

The final design for the microfluidics aimed maintain the improvements of the design, while resolving the problems observed during initial testing.

The functionality of on-chip degassing of sample fluids was sacrificed in order to improve the robustness of the device as well as to maintain optical clarity for fluorescence detection. The sample fluids can be degassed off-line before injection into the device.

The use of helium significantly helps to reduce bubble formation. Therefore, the vacuum lines could be moved further away from fluidic channels, closer to the injection ports, to allow for the escape of the helium. The design of the vacuum lines was also significantly simplified, with less number of ports required.

Injection ports were spaced further away from metal lines that were also re-designed. This helped to improve the strength of the PDMS-nitride bond around the injection ports. This is necessary because the PDMS around the ports is subjected to very large stresses when tubing is inserted. The number of critical alignment areas was also reduced. The final result was avoidance of shorting out the metal lines, which occurred when the bond failed and water contacts the gold lines.

Lastly, the widths of the valves were increased to width of 200μm to improve sealing when actuated. A combination of 200μm and 100μm wide valves used for the pumps, to ensure good sealing of the sample loop.

The final designs are shown in Section B.1.3.

3.2 Silicon Device

The initial design of the silicon chip was carried out in the *Fall 2003, Microfabrication Project Laboratory class (6.151)* [5]. Process modeling simulations were carried out on SUPREM to determine the implant parameters, as discussed in Section 2.1. Heat transfer modeling was carried out to simulate the thermal isolation of the thin membranes and to determine the geometry of the heaters. The design incorporated both the suspended heaters as well as the field effect sensors developed by Russo [16]. Layouts of the initial design are shown in Section B.2.1, and the layout of the sensor region is shown in Figure 3–1. The cross section profile of the sensors and heaters is shown in Figure 4–17.

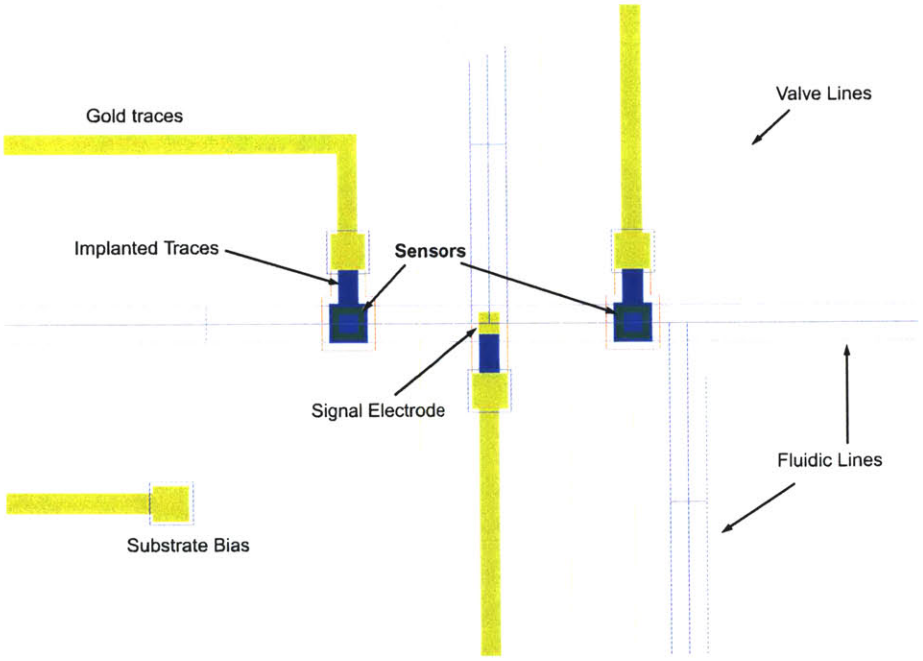

Figure3–1: Schematic layout of the sensors.

After initial testing of the fabricated devices, design changes were implemented to improve the yield, quality and ease of assembly and packaging of the devices. In particular, modifications were made to the gold traces.

The traces in the sensor area were rearranged so that there was more space between the metal lines and the microfluidic channels. More spacing was also allowed around

the microfluidic ports. This improved the bonding of the PDMS to the nitride and reduced the occurrence of leakage that would short the device.

Due to the large number of ports required to control the on-chip valves and pumps, the PDMS chip requires significant real-estate on the device and the edge is very close to the bond pads. During wire bonding, the thickness of the PDMS blocks the view of the bond pads, increasing the complexity of wire bonding the device. The resultant wire bonds are often weaker and break easily. Therefore the bond pads were extended closer to the edge of the die. This improved the visibility of the bond pads, and increased the area for bonding. The result was an increase in the ease of wire bonding process and the improvement in the quality and strength of the bonds.

The final layouts incorporating these design improvements are shown in Section B.2.2.

Chapter 4

Fabrication and Packaging

4.1 Microfluidic fabrication

The microfluidic dies are fabricated by casting silicone elastomer on a mold. The elastomer used, polydimethylsiloxane (PDMS), is a two part mixture that cures after mixing . Upon curing on the mold, the PDMS is then diced and cored to complete the fabrication process. The whole process from start to finish was carried out in the Manalis Lab.

4.1.1 Wafer layout

The design of individual dies are replicated on a wafer to create the wafer layout. This exploits batch processing in the fabrication.

In the initial layouts, the dies were placed adjacent to each other, as shown in Figure 4–1. However this made the preparation after curing very difficult. There was very little space for alignment and there was no clear marking for dicing.

After a few iterations, the final layout incorporated improvements that resulted in increased yield and the quality of the microfluidic dies fabricated. The final layouts for both layers are shown in Figure 4–2.

Firstly, the dies are spaced $1.6mm$ apart in the layout for the valve layer. This allows for ease of dicing the PDMS on the wafer, without damaging the mold. It

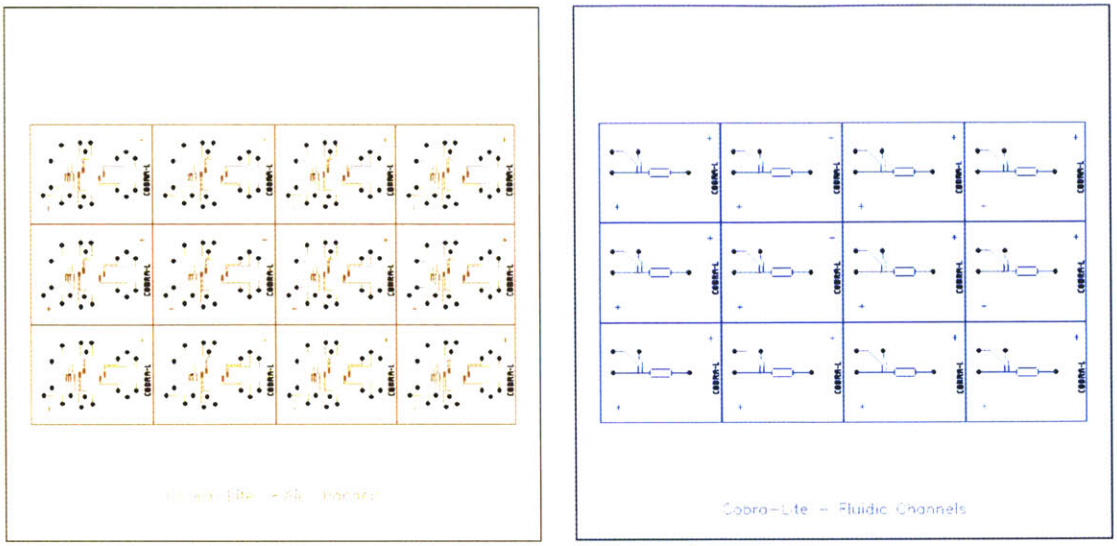

Figure4–1: Initial layouts for the valve and fluidic layers.

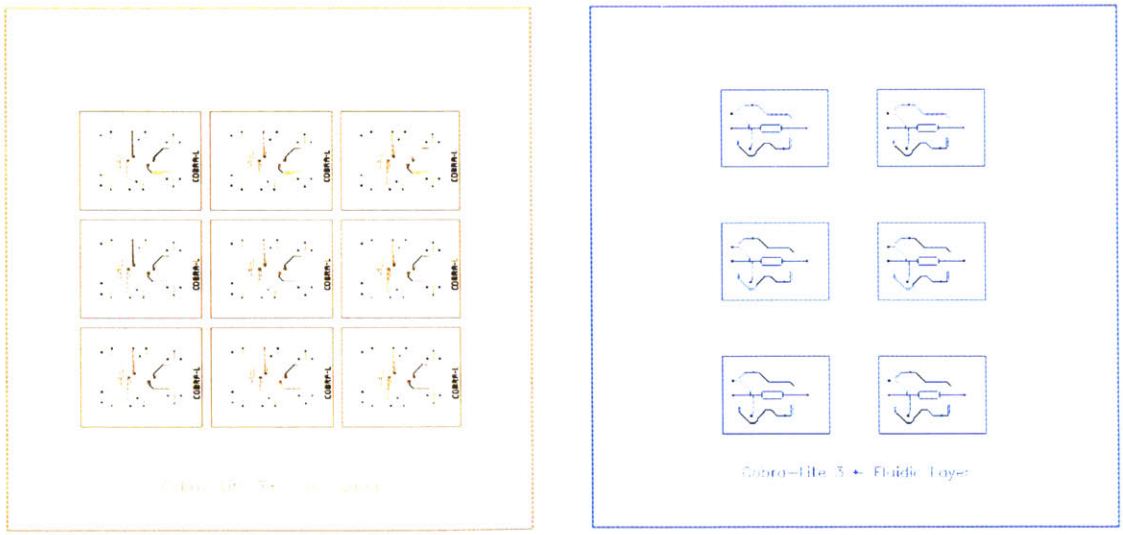

Figure4–2: Final layouts for the valve and fluidic layers.

also allows for unused dies to be kept in contact with the wafer, thereby helping to prevent contamination of the dies.

Secondly, the die outline for the control layer is about $2mm$ larger than that for the fluidic layer. This ensures that there is enough excess material to allow for a smooth trimmed edge after bonding.

Finally, there are only six dies on the layout of the fluidic layer. The $7mm$ space between the dies to allows for maneuverability of the control layer during alignment.

4.1.2 Mold making

The mold for casting the PDMS is fabricated by patterning photoresist on a 4 inch silicon wafer using standard lithography techniques. The masks are printed from the wafer layout, at 1.5% larger than the actual size, to account for the shrinkage of PDMS when curing at elevated temperatures.

The mold for the valve layer is fabricated by patterning SU8-50 (MicroChem Corp.), a negative photoresist. The process steps are listed below:

1. Rinse wafer with acetone, isopropanol, and water
2. Dehydrate the wafer — Bake in oven for $10min$ at $120°C$
3. Spin coat SU8-50 photoresist — Dispense SU8-50, ramp to $1500rpm$, and spin for $30s$ (P6204 Portable Precision Spin Coater, Speedline Technologies)
4. Pre-exposure bake — Bake on hotplate for $10min$ at $65°C$ followed by $30min$ at $95°C$
5. Exposure — $40s$ at 50% intensity (Intelli-ray 400, Uvitron International Inc.)
6. Post-exposure bake — Bake on hotplate for $1min$ at $65°C$ followed by $10min$ at $95°C$
7. Develop — develop in SU-8 developer for about $10min$, until development is complete

8. Rinse with isopropanol and dry with air gun (continue developing if there is undeveloped white residue remaining)

9. Hard bake — Bake in oven for $10min$ at $150°C$

The wafer should be allowed to cool down after the post-exposure bake step, before the development step. This reduces the formation of cracks in the SU8 due to stress concentrations at the corners. The final hard bake also helps to anneal some of the defects.

In order to prevent T-topping of the features, a Schott glass filter (BG-12) was used to filter off wavelengths below $350nm$ from the broadband UV-light source. The result was straight side walls of the valve channels, as shown in Figure 4–3. It is also important to note that the post-exposure bake is rather sensitive to time. Over baking could result in under-developed features. The final SU8 mold for valve layer is shown in Figure 4–4.

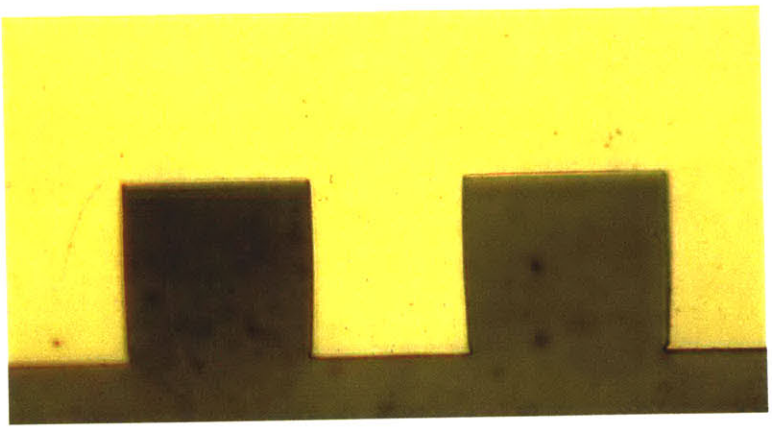

Figure4–3: Cross-section of $100\mu m$ wide valve channels in PDMS, showing straight side walls.

The mold for the fluidic layer is fabricated by patterning AZ-4620 photoresist (AZ Electronic Materials). The photoresist has a glass transition temperature, that allows the reflowing of the resist after development. This results in the desired semicircular cross-sectional profile in the fluidic layer required for complete sealing of the valves. The process steps are listed below:

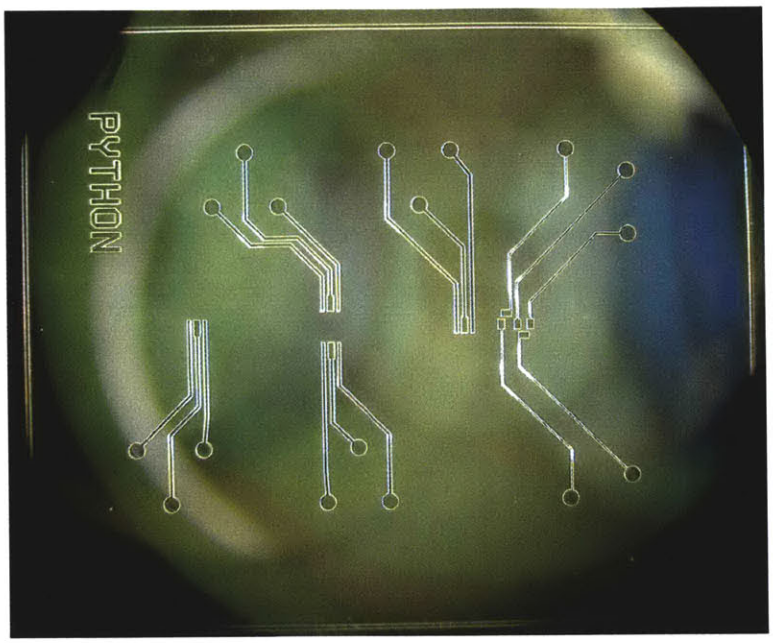

Figure4–4: A die on an SU8 photoresist pattern for a valve layer mold.

1. Rinse wafer with acetone, isopropanol, and water
2. Dehydrate the wafer — Bake in oven for $10min$ at $120°C$
3. Spin coat hexamethyldisilazane (HMDS) — Dispense while spinning above $1000rpm$ and continue spinning until evenly coated (Rainbow colors appear on the wafer and fade away)
4. Spin coat AZ-4620 photoresist— Dispense Az-4620, ramp to $1500rpm$, and spin for $50s$ (P6204 Portable Precision Spin Coater, Speedline Technologies)
5. Pre-bake — Bake in oven for $60min$ at $90°C$
6. Exposure — $20s$ at 50% intensity (Intelli-ray 400, Uvitron International Inc)
7. Develop — develop in AZ-440MIF developer for about $2 - 3min$, until development is complete
8. Rinse with water and dry with air gun
9. Reflow — Bake wafer upsidedown in oven for $60min$ at $150°C$

The rounded profile of the photoresist pattern resulting from the reflow process step is shown in Figure 4–5. Using this process, the desired semicircular cross-section for the molded PDMS channels was achieved and it can be observed in Figure 4–6. The final AZ-4620 mold for the fluidic layer is shown in Figure 4–7.

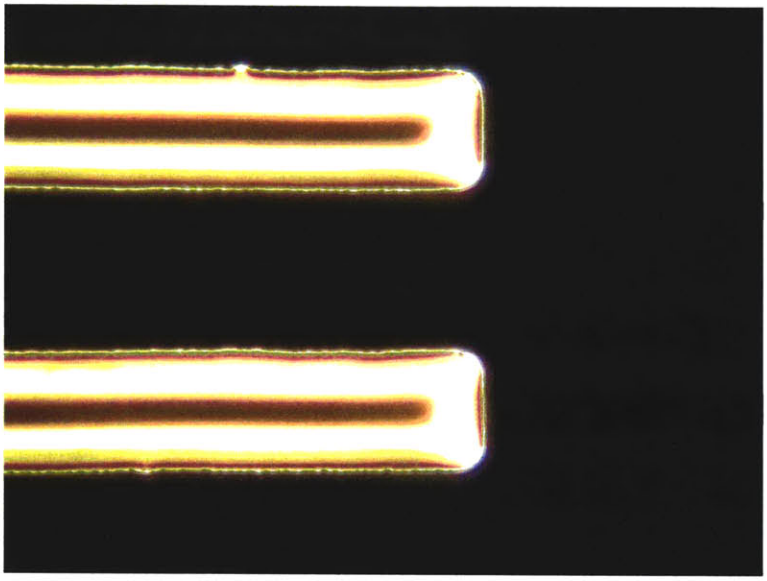

Figure4–5: The rounded edges of the reflowed photoresist pattern can be observed from its dark field image.

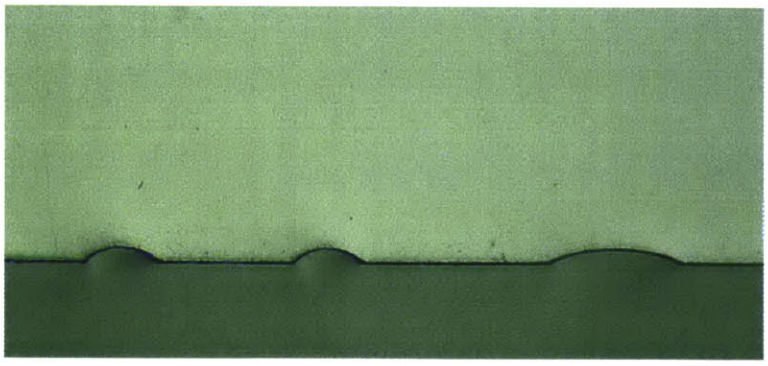

Figure4–6: Cross-section of fluidic channels in PDMS, showing the desired semicircular profile.

The height of the microfluidic channels is determined by the thickness of the photoresist, which in turn is determined mainly by the parameters of the spin coating

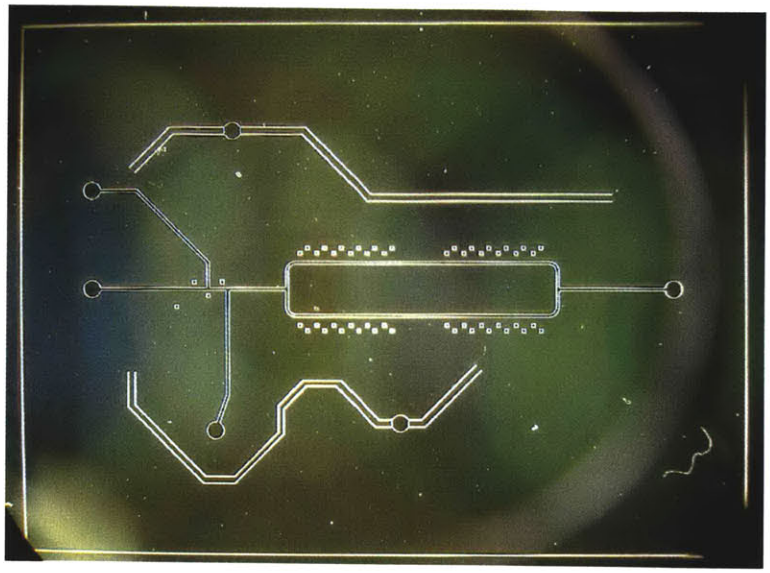

Figure4–7: A die on an AZ-4620 photoresist pattern for a fluidic layer mold.

step. Therefore a series of characterization wafers were processed, to relate the measured thicknesses to the spin coating parameters. An average of three measurements at different parts of the wafer were used to determine the thickness of the patterns.

The thicknesses of the AZ-4620 patterns were measured on a Detak 3 profilometer (Veeco Instruments Inc.) The results are summarized in Table 4.1.

Spin Speed $[rpm]$	**Post-Development** $[\mu m]$	**Post-Reflow** $[\mu m]$
1500	10.3	12.9
2000	9.3	10.3
2500	8.1	9.9
3000	7.3	9.8

Table 4.1: *Average thicknesses for AZ-4620 photoresist characterization*

The SU8 patterns were more than $50\mu m$ thick which exceeded the range of the profilometer. However since the thicknesses did not require high tolerances, they could be measured on the Nikon trinocular microscope, using its scaled focusing knob. By focusing on the top and bottom edges of the pattern, at 100x magnification, the step height could be read off the scale. The estimated $\pm 2\mu m$ accuracy was sufficient for the control layer, and the results are summarized in Table 4.2 below.

After the molds have been made, the final step is to silanize the wafer to allow the

Spin Speed [rpm]	Average Thickness [μm]
1000	94
1500	70

Table 4.2: *Average thicknesses for SU8-50 photoresist characterization*

release of PDMS from the mold after curing. The wafers are placed in a aluminum boat, with two drops of (tridecafluoro-1,1,2,2-tetrahydrooctyl)trichlorosilane on the boat, facing the backside of the wafers. The boat is loaded into a desiccator, which is then kept under vacuum for two hours. Under the low pressure, the silane vaporizes and reacts with the mold to form a monolayer of silane, terminating the free radicals. This prevents the PDMS from reacting with the wafer as it cures, thereby allowing the cured PDMS to be released.

4.1.3 Materials and preparation

There are two types of PDMS currently used for microfluidic devices — Sylgard 187 from Dow Corning, and RTV 615 from GE Silicones. Both elastomers come in two part mixtures, consisting of the base and a curing agent. The recommended standard mixture is one part curing agent to ten parts base (1:10). After thorough mixing, the elastomer is the cured at elevated temperatures. The molds have to be kept level during curing in order to produce dies that have parallel surfaces. This is import for successful for alignment and bonding steps later in the process.

The final stiffness of the cured PDMS has been observed to be inversely related to the viscosity of the mixture. This is because the curing agent is less viscous than the base. However when comparing the RTV and Sylgard silicones this relationship still holds true. RTV elastomer is more viscous than Sylgard elastomer during mixing, and upon curing the RTV elastomer is observed to be less stiff than the Sylgard elastomer. Therefore it is desirable to use the RTV elastomer for the double layered devices to reduce the actuation pressure required. However, the polyethylene tubing (Intramedic, Becton Dickinson & Co) used to interface with the device spontaneously pop out of the ports of the RTV devices. Therefore a combination of materials is used to fabricated the double layered devices — Sylgard for the valve layer, and RTV

for the fluidic layer.

The double layered devices are fabricated by bonding two separately molded layers. The PDMS for the valve layer is mixed with an excess of curing agent (1:7, Sylgard 187). To obtain a $5mm$ thick valve layer, $10g$ of curing agent is mixed into $70g$ of the base. The PDMS for the fluidic layer is mixed with an excess of base (1:20, RTV 615), $10g$ of curing agent and $20g$ of the base is sufficient for spinning on to the mold wafer. The thoroughly mixed PDMS then has to be degassed in vacuum until all the bubbles have been removed. The individual layers are then partially cured, until they have just solidified and can be diced and cored. The two layers are then processed, aligned, placed in contact with each other and allowed to completely cure. The resulting bond of a successful process is extremely strong.

However, success of bonding relies heavily on how much the two layers have been cured prior to being placed in contact with each other. Ideally the layers should be minimally cured — just sufficient for handling, dicing, and coring. Also, cure times vary depending on each batch of elastomer. Therefore it is important to track the curing progress of the elastomer. The curing times have been observed to be about $9min$ for the valve layer using Sylgard elastomer, and about $10min$ for the fluidic layer using RTV elastomer. Once the PDMS returns to room temperature, the curing rate reduces significantly and there is ample time to process the PDMS without detriment to the bond quality.

The thicknesses of spin-on PDMS for the fluidic layer was characterized to determine the thickness of the thin membrane between the valve and fluidic channels. This thickness determines the actuation pressure required to seal the valves. If the membrane is too thick, high actuation pressures would be required. Conversely, if the membrane is too thin, the valves would be slow to reopen, or even stay adhered to the channel floor, after the release of pressure.

A series of experiments was carried out, whereby PDMS (1:20 mixture) was spun onto separate wafers over a range of spin speeds. After curing, a part of the thin membrane was torn off, and the step height was measured on a Detak 3 profilometer

(Veeco Instruments Inc). Three measurements were taken for each sample and the average of the measurements determined the required parameters for the spin coating step. The results of the characterization experiments are summarized in Table 4.3.

Spin Speed $[rpm]$	Average Thickness $[\mu m]$
2000	35
2500	26
3000	21
3500	19
4000	16

Table 4.3: *Average thicknesses for characterization of spin-on PDMS*

4.1.4 Alignment and bonding

The alignment of the two PDMS layers can be based on cross hairs designed into the mold, or based on the alignment of critical features on each die. For this device, the critical area of the sensor valves was chosen as the alignment feature.

An alignment stage was assembled for the purposed of aligning the two PDMS layers as well as for alignment between the completed PDMS dies and the silicon device. The stage included custom designed and machined parts, such as the vacuum chuck turntable, and various acrylic plates for mounting the PDMS dies, and is shown in Figure 4–8.

As mentioned in Section 4.1.3, successful bonding is dependant on the curing times. However it is also highly dependant on the cleanliness of the surfaces. Moreover, large particles can land on the dies and cause clogging or leakage.

Therefore, the PDMS should be thoroughly cleaned, after dicing and coring the valve layer, before bonding to the fluidic layer. This involves washing with detergents, such as Micro-90 (International Products Corp.), followed by rinsing with water and ethanol. The final step is to blow dry with an air gun.

The actual alignment step is then carried out in the fume hood, as shown in Figure 4–9. The filtered airflow through the hood helps to reduce particulate contamination. However, care must still be taken to keep samples covered, and to manipulate the samples with the critical surface facing down.

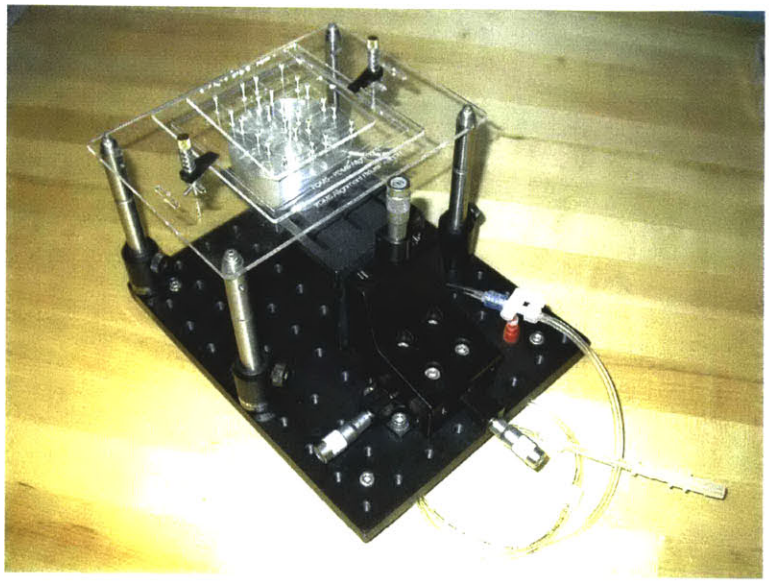

Figure4–8: Alignment stage.

Figure4–9: Alignment for PDMS bonding or packaging is carried out in the fume hood to reduce particulate contamination.

The result of successful alignment and bonding is shown in Figure 4–10. The cross section of the double layered stack is shown in Figure 4–11.

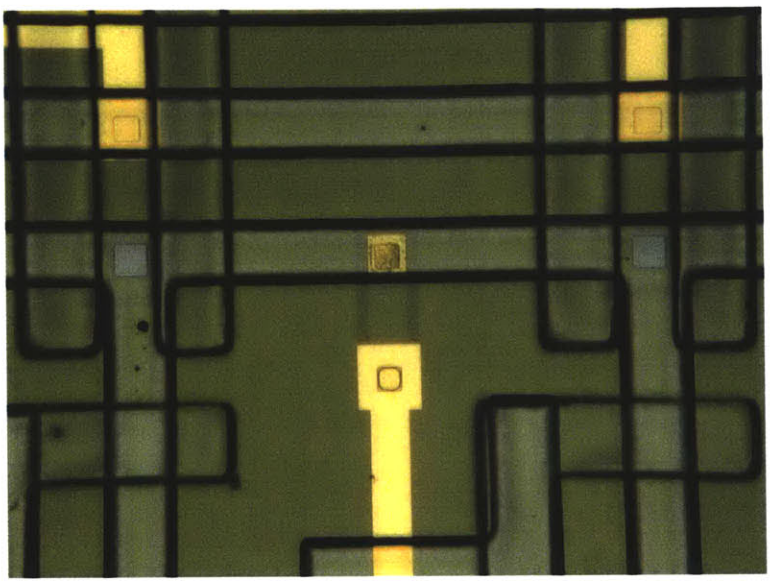

Figure4–10: Successful alignment for both PDMS-PDMS and PDMS-device alignment steps.

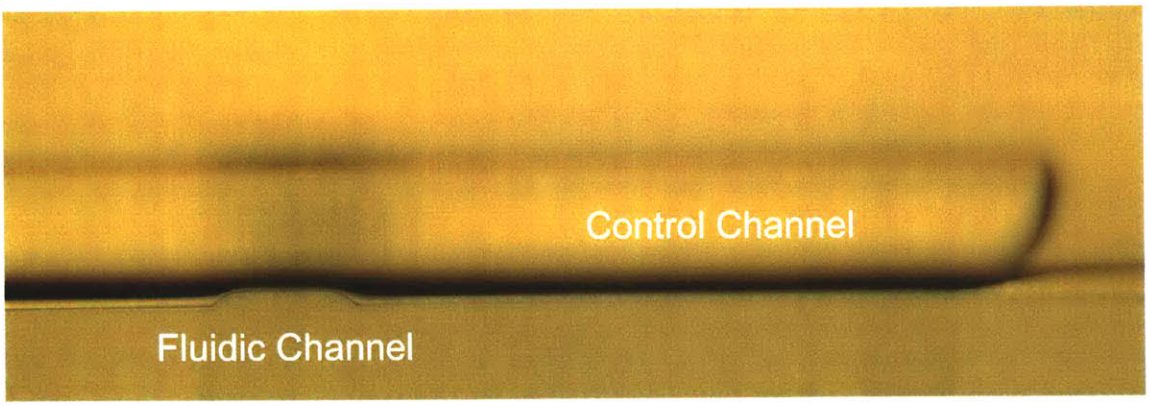

Figure4–11: Cross section of a double-layer PDMS stack.

4.1.5 Dicing and coring

There are many ports that are closely packed on the microfluidics die. Although there is ample spacing between ports to prevent leakage, it was important to ensure

that the ports were vertical. Dicing and coring was initially carried out completely manually with razor blades and sharped needles. Therefore, it was difficult to achieve the desired standards.

The "Micro-Guillotine" was designed, machined and assembled for this purpose, and is shown in Figure 4–12. It consists of a fixture for securing a razor blade as well as a needle, onto a linear translation stage. This allowed ports to be cored vertically. It also produced vertically trimmed sidewalls that were optically clear, allowing for easy lateral observation of the device. This is useful for observing the inserting of tubing as well as introducing fluid into the channels, as shown in Figure 4–13.

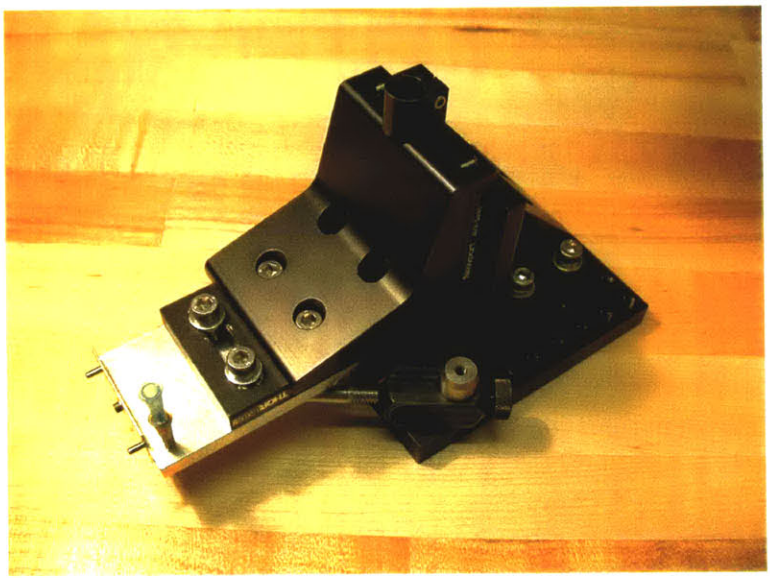

Figure4–12: "Micro-Guillotine" for dicing and coring microfluidic dies.

The ports were cored using needles ranging from $18 - 20ga$, depending on the external diameter of tubing used. Initially, a luer stub adaptor (Becton Dickinson & Co), which is basically a needle with a flat tip, was used to core the ports. However, this produced rough edges and side walls, leading to frequent tearing of the ports when inserting tubes. These tears often caused leakage of fluids.

To improve the quality of coring, the needles were hand sanded to sharpen the edges, as shown in Figure 4–14. The ports cored with these sharpened needles had very smooth edges and sidewalls, as shown in Figure 4–15. This improved the quality

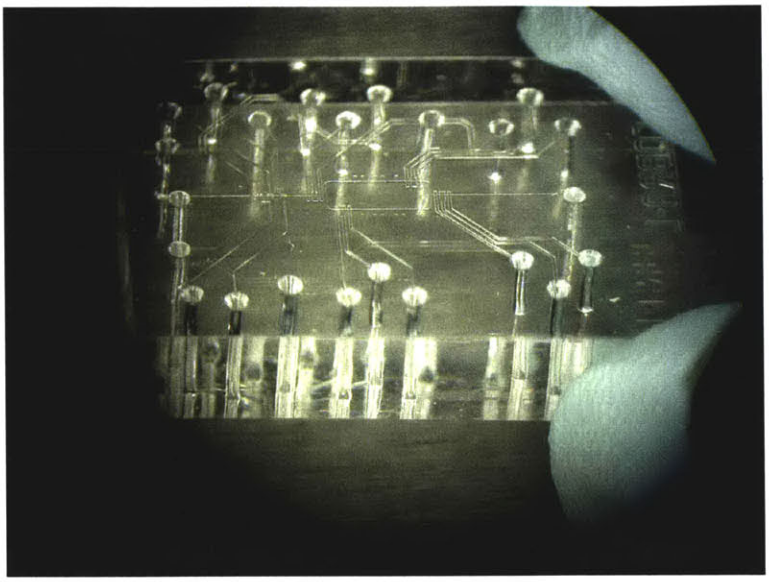

Figure4–13: Vertical port and clear side walls of a device that was diced and cored with the "Micro-Guillotine".

of the seal between the port and tubing, hence improving the yield of the microfluidic devices fabrication process.

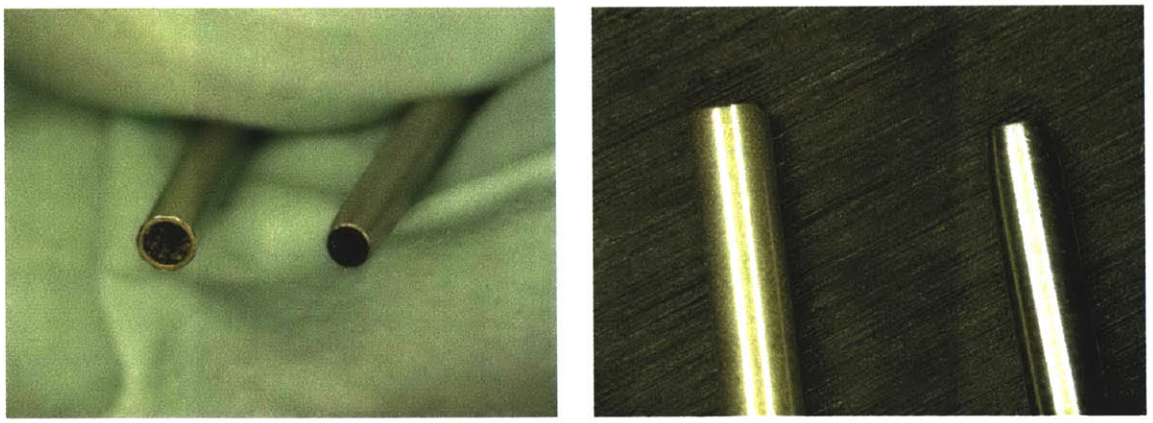

Figure4–14: The coring needle is significantly sharper after hand sanding.

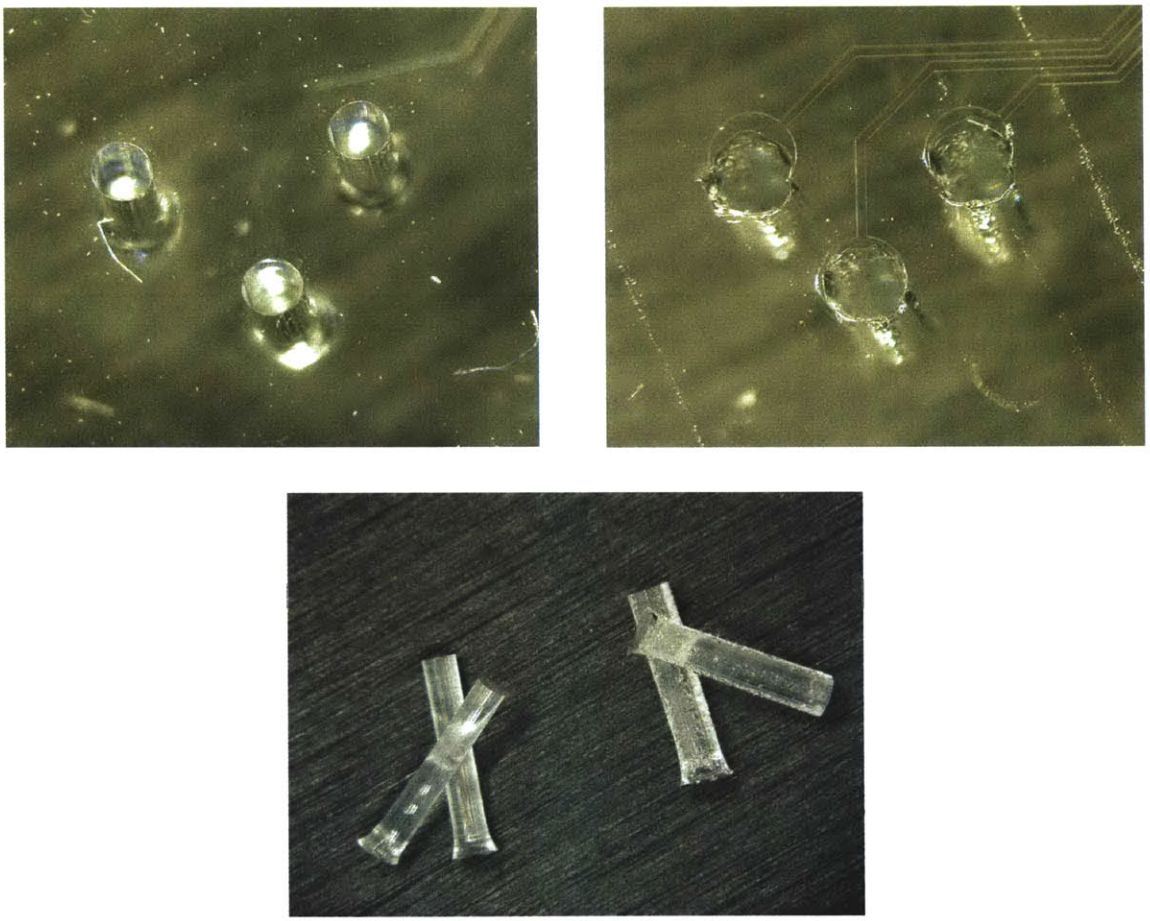

Figure 4–15: The ports cored with a sharpened needle (left) have a smooth round edge compared to the jagged edges of the ports cored with a blunt needle (right). The respective core samples are shown on the bottom.

4.2 Silicon Device Fabrication

The silicon processing was carried out mainly in the MIT Microsystems Technology Laboratories (MTL). Some steps were completed in the Manalis Lab, and the implant steps were out performed by Innovion Corp.

The devices were fabricated on $< 110 >$, n-type, 6" wafers. The substrate resistivity was measured at $50 - 75\Omega cm$, and the wafer thicknesses are $600 - 650\mu m$.

A micrograph of the microfabricated integrated device, with heaters and sensors is shown in Figure 4–16 below.

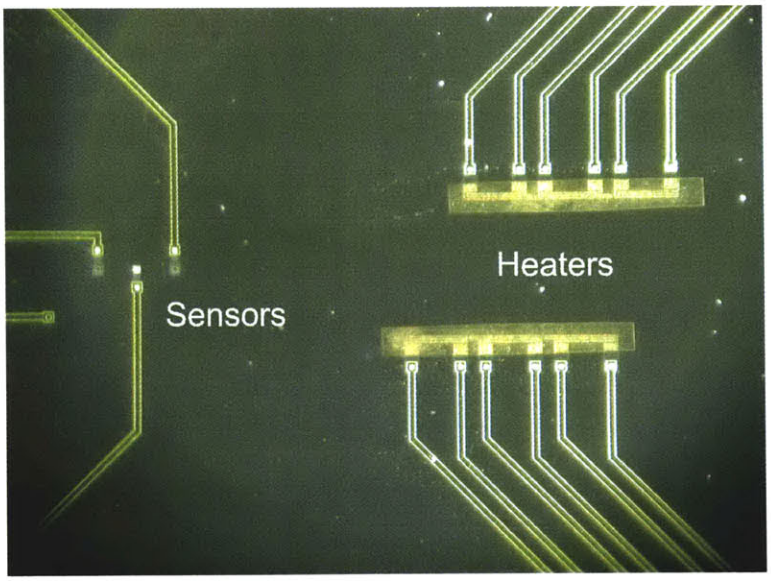

Figure4–16: Micrograph of a Cobra-Lite silicon device, showing the integrated field effect sensors and suspended heaters.

4.2.1 Initial process

The first batch of silicon devices were fabricated as part of the *Fall 2003, Microfabrication Project Laboratory class (6.151)* [5], and the process flow is shown in Appendix A. After the initial batch of wafers were packaged and tested, the results revealed several improvements to the process that were required to improve device quality and yield.

Firstly, the yield of functional heaters was also rather low. All the resistive heaters that worked had significantly higher resistances than the theoretical values. These resistances were determined by measuring the I-V curve of the heaters. Many of these curves were erratic and barely reproducible. Often, the resistances of these devices could not even be measured on a multimeter. This applied even to optically intact heaters, that had not been over-etched by potassium hydroxide.

Secondly, only one device, out of the many tested, had functional sensors. The devices that failed had either signals with a largely attenuated range or had hardly detectable signals that were close to the noise floor. This observation was consistent with contact issues. The electrical contacts from the instruments all the way to the metal traces were tested and were determined to be functional and robust. Also the contact for the substrate bias was demonstrated to be working. This elimination process isolates the problem with the sensors themselves.

After considering both issues, both problems were attributed to over-etching during the nitride etch step for exposing up the sensors and contact holes (Step 28, Appendix A). During fabrication, the nitride etch was timed longer, in order to ensure good electrical contact between the metal lines and the doped silicon. However, given the chemistry used, the etch selectivity for doped silicon is similar to that of nitride. Since the thickness of the nitride and the implant depth were both about $1\mu m$, it was likely that over-etching had occurred.

In the case of the heaters, the contact area could be reduced by ten times due from $40\mu m^2$ to about $4\mu m^2$. This is also consistent with the observation of overly high resistance and poor I-V curve characteristics. Also, the decomposition of PDMS starting from the gold-silicon interface indicated that a large amount of heat was generated at that interface, which is consistent with a large contact resistance.

For the sensors, this meant that the sensor itself had been etched away either partially or completely. This is consistent with the small signals observed.

Both cases are illustrated in Figure 4–17.

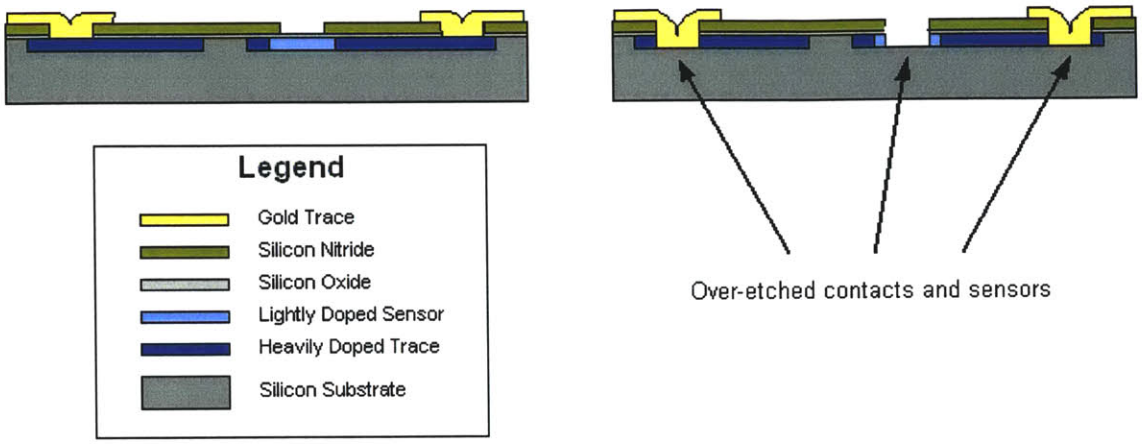

Figure4–17: A comparison of schematic cross-sections, between an ideal device (left) and a device that was over-etched during the nitride etch step (right).

4.2.2 Process improvements

Several process changes were implemented to increase the fabrication yield, and improve device performance.

In order to avoid over-etching into the device layer, the nitride etch step was carried out in the Lam Autoetch 490b (Lam Research Corp). This machine was chosen because it is capable of detecting the reaction endpoint. Also, all wafer handling is carried out mechanically with out any vacuum system that could damage the thin nitride membranes. Also the simple handling system is more robust and have a higher capacity to accept mounted wafer stacks, if a handle wafer should be necessary. When a wafer is loaded into the etch chamber, it is first placed on four raised pins, before being lowered onto the chuck. These pins are situated close to the location of the thin nitride membranes. As such, a handle wafer was required to prevent the possibility of breaking the membranes.

Mounting the device wafer on a handle was also advantageous in eliminating the need for the custom mechanical chuck, which used in the initial process. This allowed the wafer to be coated on the spin coater using a teflon vacuum chuck, resulting in a more even coat of photoresist. This even coat of resist helped to eliminate earlier problems faced during the subsequent exposure step.

However, mounting the device wafer on a handle is an intricate process. Photoresist is used to glue the two wafers together. If too little resist is used, the wafer stack could delaminate, especially during the spin coating process. Conversely, if too much resist is used, the resist would spread and coat the whole wafer, making it extremely difficult to completely bake out the solvents. These solvents would eventually vaporize during etching, due to the heat generated, and the outgassing would dislodge the device wafer. This would result in uneven etching, and possibly even catastrophic damaged to the device. This delamination was often observed by large spikes in the readout for the optical end point detection.

Previously, thin resist (OCG825) was used as the adhesion layer to ensure levelness of wafer for accurate alignment and good mask contact during exposure. However, the thin resist is very fluid and will spread easily. *It is therefore highly recommended to try using thick photoresist (AZ-4620) as the glue for wafer mounting, for the etch step.* The viscosity of the thick resist would help avoid the spreading of resist, and therefore allow the solvents to be baked out before the etch process. It would also be worthwhile to try a test pattern on dummy wafers to ensure that there are still vents to aid complete evaporation of solvents.

The process for mounting the device wafer on a handle is listed as follows:

1. Apply photoresist — Sparingly spot photoresist evenly across the back side of the device wafer using a swab

2. Affix handle — Align the flats of the handle and device wafers and gently press the wafers together

3. Soft bake — Bake for $15min$ at $90°C$

4. Patterning — Proceed to spin coating, exposing, and developing

There a couple of important caveats to note. After the $15min$ soft bake, the adhesion is strong enough for the wafer stack to be patterned conveniently. However, there will probably still be solvents in the adhesion layer that would outgas if the

stack is put through any processes with elevated temperatures. This could cause the wafers to separate.

Also, if the wafer stack is put through a complete lithography process, developer will seep between the wafers during the development step. This would significantly compromise the adhesion. Therefore, the wafers should be carefully separated using a razor blade, and the mounting process can then be repeated to renew the adhesion.

The Lam Autoetch 490b is a RF dry etcher using sulfur hexafluoride (SF_6) and oxygen (O_2) chemistry to etch the nitride windows. The general recipe is listed below and details can be found on the MTL website.

- SF_6 — $190sccm$
- O_2 — $19sccm$
- Pressure — $300mT$
- RF power — $130W$
- Sessions — $3 \times 4min$
- Helium cooling
- Optical endpoint detection

The endpoint detection uses an optical readout to monitor the gas composition in the chamber. For detecting end point of etching nitride, the readout drops when oxide is exposed and rises when silicon is exposed. The change in signal is only about $10 - 20\%$

The SF_6 etch chemistry has only a slightly higher etch selectivity for nitride as compared to oxide. Therefore, there is only a window of about $30s$ before the $300\mathring{A}$ of oxide is etched away, and the underlying silicon starts getting attacked. Therefore, it is important to monitor the optical read out and stop the etching in case the endpoint is not successfully detected.

There is also an alternative method to determine if the nitride has been completely removed. By putting the wafer stack into a Buffered Oxide Etch (BOE), the wetability of the etch windows would indicate if there was any nitride remaining. The only drawback is that this method is time consuming, and it would take additional time to reload the wafer if the etch has not been completed.

In order to characterize the etch rates for the wafer stack, the backside windows on the device wafer were etched with the same process. The etch rate was determined to be about $900 \mathring{A} min^{-1}$ and the reaction endpoint was successfully detected.

However, during the etching of the sensors and contact holes on the actual wafer, endpoint not detected and etch was terminated at $13 min$. This could be attributed to the small total area of nitride being etched, therefore reducing the amount of signal for detection. Also, when the chamber was opened to unload the processed wafer, wafer stack had delaminated and was caught in the doorway of the chamber. Fortunately the machine was stopped in time, and the wafer was successfully salvaged.

At this point, the wafer was put through BOE, and it was observed that all the nitride had been removed from the windows. Also, the BOE stripped of the thermal oxide, allowing a fresh native oxide to grow in its place. This thin native oxide helps to improve the sensitivity of the senors. Optical inspection of the etched windows reveal that some of the windows had developed a rough surface, indicating that over-etching could have occurred. The difference between a smooth and rough sensor surface is shown in Figure 4–18.

Despite the difficulties, the move to use Lam Autoetch 490b for the nitride etch step was a success. The yield and quality of both heaters and sensors improved dramatically. Almost all the sensors and heaters tested were functional. Detailed results of the characterization are discussed in Section 5.2.1 and Section 5.3. The main cause for the remaining dysfunctional devices, was due to defects during the KOH etch, resulting in shorting of metal traces to the biased substrate.

The final improvement to the fabrication process was the refinement of the KOH etch process. After a bulk of the nitride membranes have been released, there was still

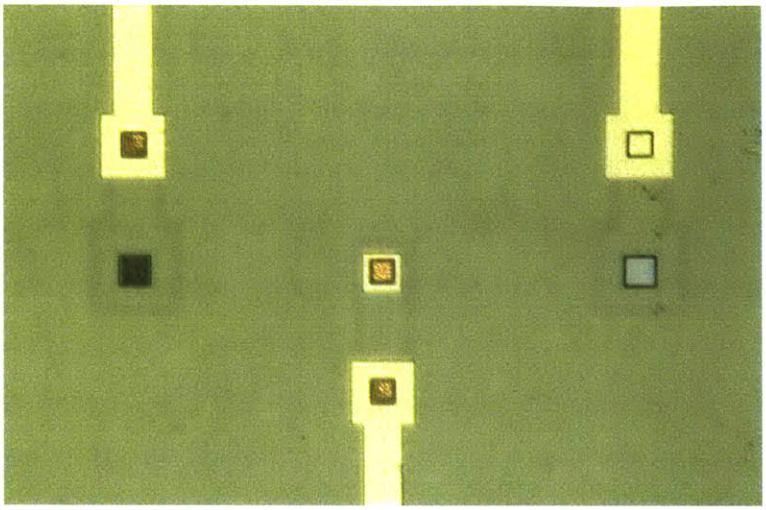

Figure4–18: Surface roughness observable (right sensor) after nitride etch, indicating possible over-etching.

much residue remaining. This residual silicon changes the electrical characteristics of the heaters and consequently, the heating profile. This was the result of using single side polished wafers.

The ideal KOH etch process has a very stable and even etch rate. However, in order to cleanly release the implanted heaters, the starting surface has to be flat and smooth. Since single side polished wafers were used for the process, the surface roughness on the backside of the wafers propagated down to the nitride membrane during the KOH etch. This resulted in an uneven surface that required additional attention to complete the etch. This could potentially be avoided by using double side polished wafers. The use of double side polished wafers would also help to improve the uniformity of the heaters, thereby increasing the quality of the devices.

To ensure the complete release of the heaters, a final KOH etch was carried out at room temperature after the wafer had been diced. The etch time for one of the dies was about $3.5hrs$, but the etch rate is slow and the endpoint can be determined optically. However, it is important not to let the solution dry as that would increase the concentration of the solution, thus increasing the etch rate. Also, it is important to ensure that the KOH solution does not overflow and start etching the sensors on the front side of the wafer.

The process steps for this final KOH etch is listed below:

1. Prepare solution — 22.5% KOH solution
2. Load die face down on a glass petri dish
3. Dispense solution — $10 - 20\mu m$
4. Observe to determine endpoint
5. Rinse die with water and dry with air gun

The additional KOH step was successfully carried out, as shown in Figure 4–19. Significant improvement in resistance uniformity across heaters on the same device was obtained, as a result. Details on the heater characterization are discussed in Section 5.2.1.

4.3 Integration and Packaging

Integration of the microfluidics to the silicon device involves alignment and bonding of the two parts. Plasma treatment can be used to permanently bond the PDMS to nitride or oxide. First the plasma treatment creates free radicals on both the PDMS and nitride surface. After surface activation, the two parts are aligned on the alignment stage (Figure 4–8) and brought into contact with each other. A final bake step helps the covalent bonds to form. Details of the procedure are listed below:

1. Clean silicon device — rinse silicon device with solvents and water
2. Clean PDMS — rinse with Micro-90 solution (International Products Corp.) and water, and dry with an airgun
3. Plasma activation — load samples facing up in the plasma chamber
4. Start plasma treatment — Plasmod Plasma Etcher, GCM-200 Gas Control Module (March Instruments Inc.)

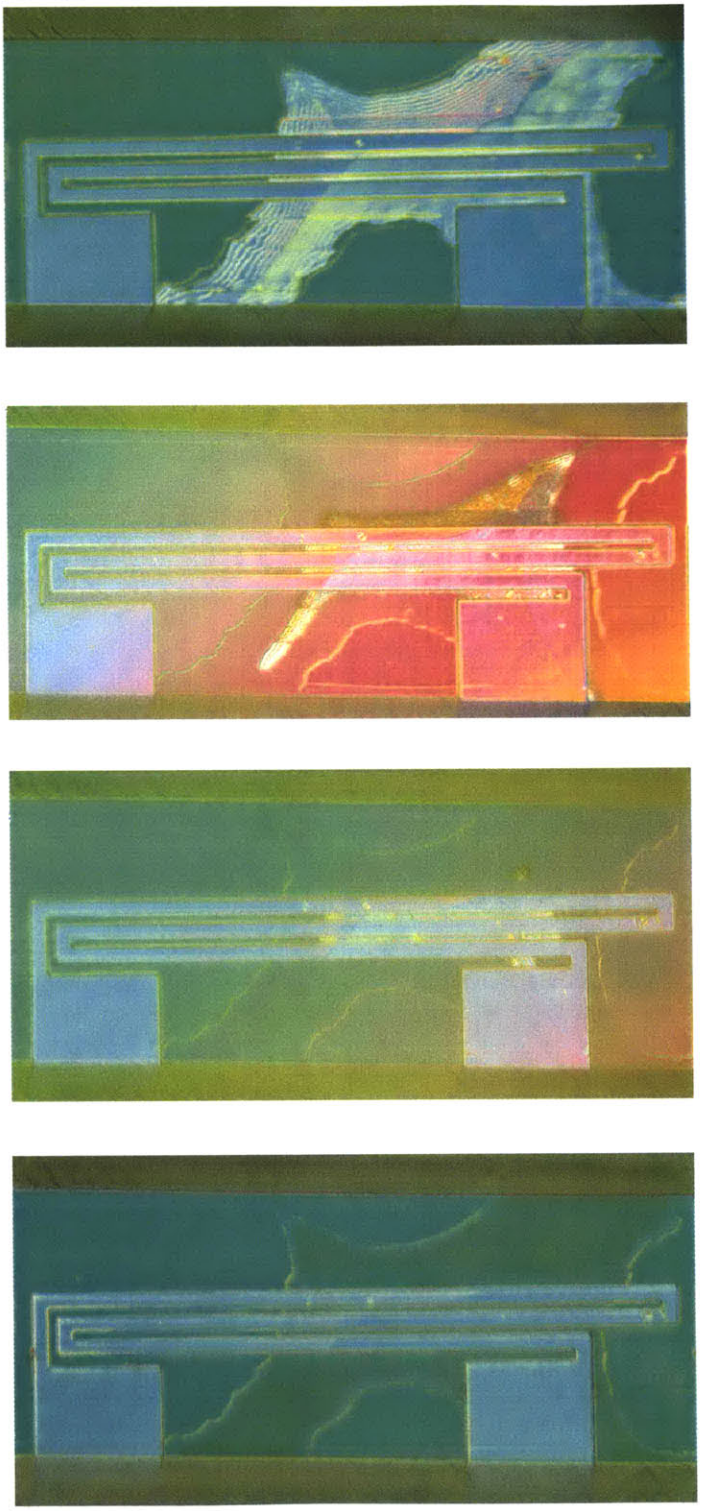

Figure 4–19: The residual silicon initially around the heater (top), is gradually removed by KOH at room temperature, until the heater is completely released (bottom.)

5. Power — $15W$
6. Pressure — $1Torr$
7. Time — $30 - 60s$
8. Check the plasma stays on throughout the activation
9. Remove samples for alignment and bonding
10. Bake — $2hrs$ at $90°C$

The bond strength and quality depends greatly on surface cleanliness. Also, it is important to completely cure the PDMS, because residual unpolymerized oligomers can defuse to the surface before bonding and affect the bonding.

One improvement to the packaging process was to extract the unpolymerized oligomers from the PDMS. This is because the oligomers were a source of contamination, which affected the surface chemistry that was being carried out on the sensors. However, the cleaning method has also proven to improve the quality of the bonds. The extraction process is listed below:

1. Hexane — soak in hexane, while stirring, for one day, exchange hexane at least once
2. Ethanol — exchange the hexane with ethanol and soak while stirring, for one day, exchange the ethanol at least once more
3. Water — exchange the ethanol with water, and soak while stirring, for one day, exchange the water at least once more
4. Dry PDMS — dry in vacuum overnight

An alternative packaging process is to use temporary adhesion. Clamps, springs, and an acrylic plate are used to secure the PDMS onto the silicon device, as shown in Figure 4–20. The springs help to regulate the clamping force and allow for even application of pressure across the whole chip.

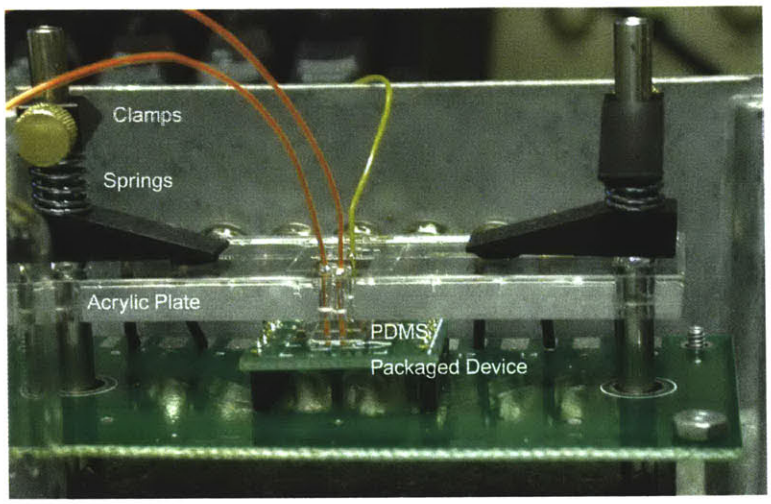

Figure 4–20: Clamping scheme for temporarily securing PDMS on to the silicon device.

In order to test the integrity of the seal, a fluorescent dye was flowed through the system at a high flow rate of $100\mu Lmin^{-1}$ for $60min$. There was no leakage observed as shown in Figure 4–21, proving that the clamping method is viable.

This packaging scheme is more flexible as it allows for swapping of fluidics for different flow profiles. It also allows for the replacement of the PDMS in the case of malfunction. The scheme is mainly used for flow through systems during sensor tests.

The assembled device is next mounted on a printed circuit board (PCB). The PCB is custom designed and sent out to Advanced Circuits Inc. to be manufactured. The traces on the PCB are plated with gold to allow for wire-bonding. These traces are aligned to the bond pads on the device to facilitating wire-bonding.

Finally the device is wire-bonded using a 747677E Utrasonic Bonder (West Bond Inc.) to complete the electrical connections. A final packaged device is shown in Figure 4–22

With the batch process used to fabricate most of the components, it is actually possible to mass produce this device. The fabrication of the microfluidic components is currently done manually in a laboratory setting. However this tedious process could conceivably be automated to increase throughput. The bottle neck of mass

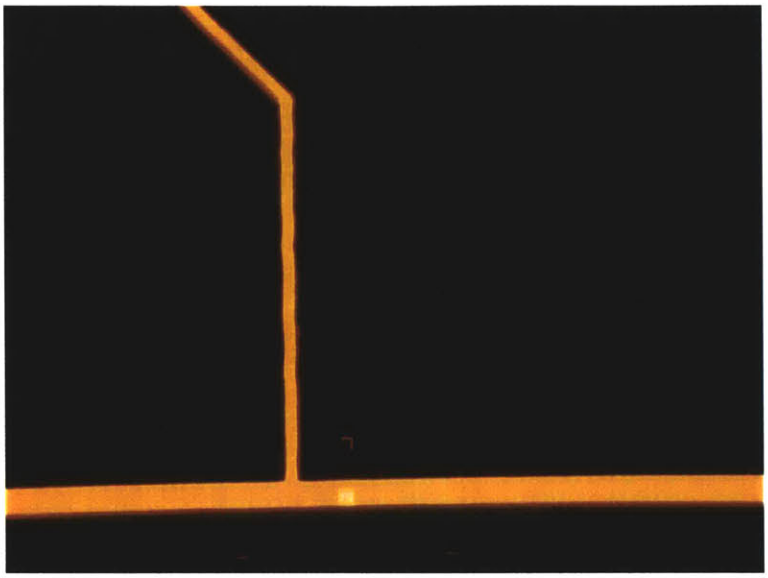

Figure4–21: Clamping is robust since no leakage is observed while flowing fluorescent dye through the fluidic channels.

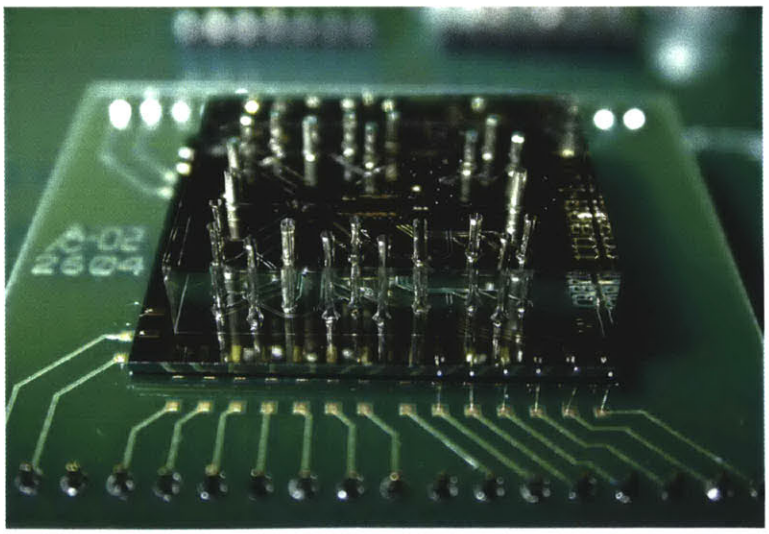

Figure4–22: Complete packaged device.

producing this device would probably be the critical step of aligning and bonding the microfluidics to the silicon die. However, with current technology in digital imaging and image processing (as shown in the electronics fabrication), it could be possible to automate this step. The main drawback remains to be high initial costs required to setup a production facility, that could carry out such a complicated fabrication and packaging process.

Chapter 5

Results

5.1 Microfluidics

The microfluidic devices were successfully characterized. Both valve and pump characterization allowed the consistent operation of the fluidic devices. Tests were also carried out to explore working with PCR samples and optical detection of the samples on-chip.

5.1.1 Experimental setup

The microfluidic devices are operated by pressurization and de-pressurization of the control channels, as discussed in Section 3.1. The control lines are exposed to a pressurized working fluid when turned on and released to atmospheric pressure when turned off. The experimental setup to control the system, is shown in Figure 5–1.

Pressurized helium is used to actuated the column of water in the connecting tubes. Helium has a lower solubility in water than most gasses, as discussed in Section 3.1.2. Also, it diffuses faster in wafer than other gasses. Together, this allows the helium in the water column to defuse out quickly into the vacuum lines before reaching the fluidic lines. Outgassing into the fluidic lines can therefore be avoided.

The main tank of helium is regulated at $80psi$, which is then stepped down by another regulator just before the valves. During the operation of the pumps, the

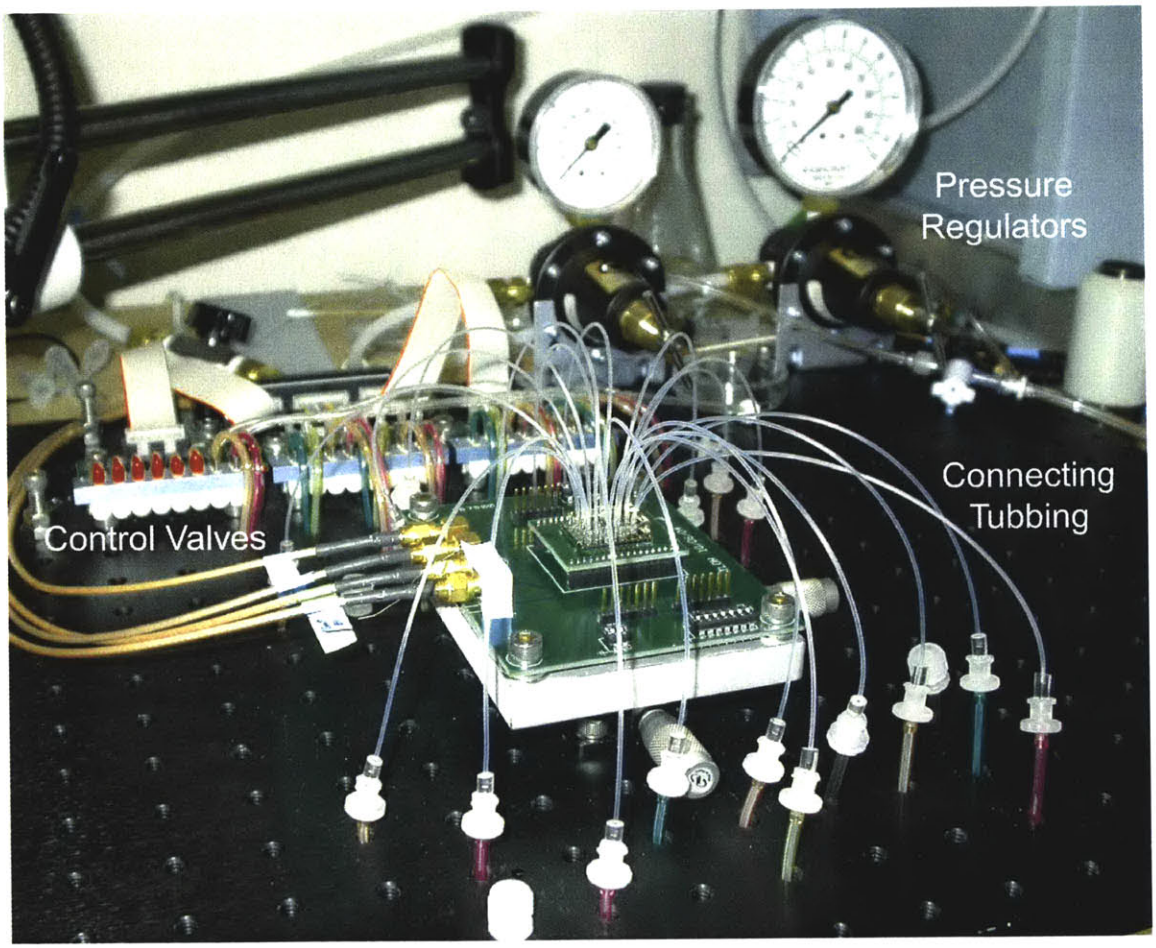

Figure5–1: Experimental setup for microfluidics.

pressure of the line fluctuates constantly. This fluctuation can affect the operation of the valves, and may lead to leakage. Therefore, the pressurized helium is split into two lines, just before the valves, and separately regulated. This allows for separation of the gas flow supplying the valve lines and the pump lines, and helps to reduce the variation in pressure for the valves lines.

A Labview program was written to control the whole fluidic system. It allows for switching of each valve, as well as to control the operation of the pumps. The console is shown in Figure 5–2.

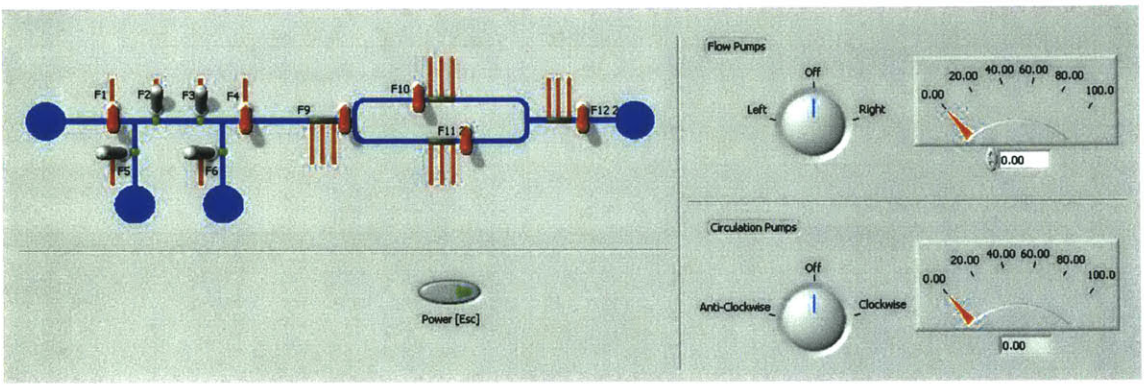

Figure5–2: Microfluidics control console.

The valves used, LHDA1223111H (The Lee Co.), could take a maximum pressure of $30psi$. However, they would heat up significantly when turned on for long periods of time. Therefore, since the control lines are usually turned off, the default position was set at the high pressure.

There is a need to fill the control lines with water to prevent outgassing into the fluidic lines, as mentioned in Section 3.1.2. This is done by filling the tubes that connect to the ports of the microfluidic device. Vacuum is applied to the vacuum lines to accelerate the process. The procedure is listed below.

1. Prepare filling fluid — degas DI water in vacuum

2. Fill an interconnecting tube using a syringe

3. Insert the filled tube into microfluidic port and connect with tubbing upstream

4. Repeat steps 2 and 3 until all the lines have been connected

5. Pressurize lines and apply the vacuum, until the air in the control lines have been replaced with water.

6. Check for valve and pump functionality

5.1.2 Fluidic valve characterization

The performance on the fluidic valves was successfully characterized. Experiments were carried out to determine the actuation pressure required to completely seal the valves. The quality of the seal can be determined visually through the microscope, as shown in Figure 5–3

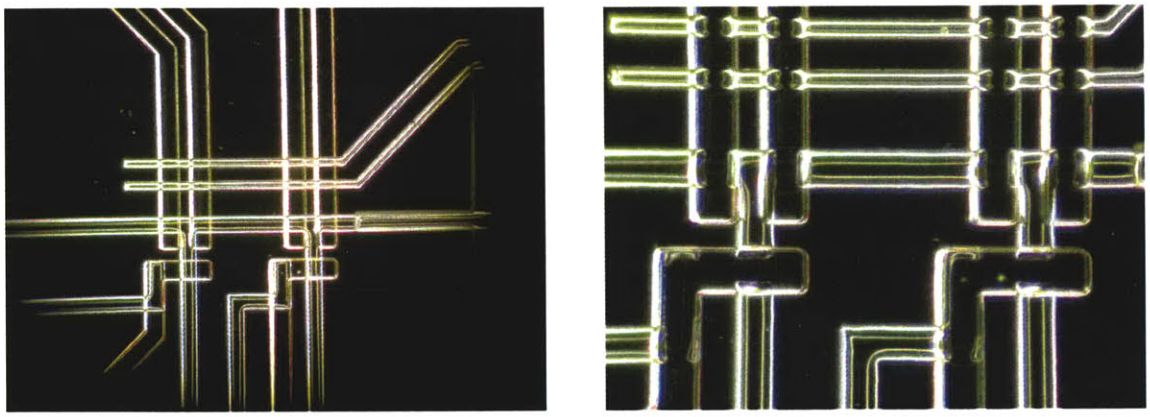

Figure 5–3: Fluidic valve characterization: Depressurized, open valves (left), and pressurized, completely closed valves (right).

The first set of tests were carried out on a static system, with no pressure through the fluidic lines. The actuation pressure was increased and the valves were observed under a stereo microscope. The sealing pressure was determined to be $4psi(30kpa)$.

The second set of tests were carried out with a $5psi(35kPa)$ line pressure. Partial closing of the valves were observed, starting at $5psi(35kPa)$ actuation pressure. The final sealing pressure was determined to be $10psi(69kPa)$

Therefore, to ensure that the valves were properly sealed, actuation pressures of $15psi$ were used to operate the microfluidic valves and pumps. The higher pressure

ensured complete valving despite pressure spikes in the fluidic channels. In later experiments, the proper sealing also helped to reduced evaporation and prevent refluxing of the reagents what were being heated in the fluidic channels.

5.1.3 Fluidic pump characterization

The pumping of fluids in the channels have been successfully characterized. Pumping is a consequence of actuating three adjacent valves in a certain sequence. This sequence determines the actual pumping characteristics — duty cycle, smoothness of flow, pump strength (against line pressure), and pump rate. Another factor is also the thickness of the valve membrane, which determines the optimum actuation pressure required for successful pumping.

The peristaltic pumps can be actuated in a few different sequences. One or a combination of the sequences can be used to pump fluids in the channels. The duty cycle of a sequence, is a fraction of the actual steps which are pushing fluid over the total number of steps. If there is a valve exposed to the line on both sides opening, the space is assumed to be filled evenly from both sides. This results in a -0.5 flow cycle. Conversely, closing a valve exposed on both sides will result in a $+0,5$ flow cycle.

All the experiments were carried out on pumps from the initial design, where all the valves had and identical $100\mu m$ width. A typical actuation pressure of $15psi$ was used. The characteristics of each sequence and its utility is described in detail below. An open valve is denoted by ◯, and a closed one is denoted by $\times$.

The "Two Down" sequence (Table 5.1), seals the chamber well, and therefore has good resistance to line pressure. However, it only has a duty cycle of 1/3, making the flow very choppy.

1.	◯	$\times$	$\times$
2.	$\times$	◯	$\times$
3.	$\times$	$\times$	◯

Table 5.1: *Pump sequence: "Two Down"*

The "Drumming Fingers" sequence (Table 5.2), creates the smoothest flow, having

a high duty cycle of 2/5. However, it has low resistance to line pressure because the channel is completely open in one of the steps. Therefore it is ideal for circulating fluid in the loop during the reaction, but not for pumping fluids across the device.

1.	○	×	×
2.	○	○	×
3.	○	○	○
4.	×	○	○
5.	×	×	○

Table 5.2: *Pump sequence: "Drumming Fingers"*

The "Moving Chamber of II" sequence (Table 5.3), is a nice compromise, combining resistance to line pressure with smoother flow. The duty cycle is 1.5/4. Therefore, this sequence was chosen for the pumping of fluids across the device.

1.	○	×	×
2.	○	○	×
3.	×	○	○
4.	×	×	○

Table 5.3: *Pump sequence: "Moving Chamber of II"*

Initial tests showed that the peristaltic pumps do not hold up well to line pressure. If there was an imbalance in line pressure, it would significantly affect the flow rate. Therefore the pump rate experiments are all carried out in the PCR loop closed off by the valves. Bubbles were used to visualize the flow of the fluid.

The pump rate was characterized for the "Moving Chamber of II" sequence, using devices from the initial fluidic design (Section 3.1.1. A bubble was pumped around the loop and the time taken for the bubble to travel a complete loop was timed with a stop watch. The results are summarized in Table 5.4. The maximum pump rate obtained, for a sample loop of $11nL$ estimated volume, was $1.8nL^{-1}s$.

The microfluidics from the final design layout (Section 3.1.3) were tested successfully. The increased width of the valves helped improve the sealing, and the functionality of the pumps was validated. However more test would need to be carried out to fully characterize the sealing pressures and pump flow rates.

Pump Frequency $[Hz]$	Loop Time $[s]$
100	6
50	12
20	26
10	49

Table 5.4: *Pump rate characterization for "Moving Chamber of II" sequence*

5.1.4 Fluorescent detection of PCR products in microfluidic channels

In order enable the independent characterization of successful PCR in the channels, the fluorescent detection of PCR products in the fluidic channels was investigated.

The PCR reagents were prepared in the following concentrations, and then divided into $100\mu m$ aliquots. SYBR Green I (Invitrogen Corp) was added to the reagents at $10000\times$ as prescribed.

- DNA template — $4nM$
- dNTPs — $0.2mM$
- Primer 1 — $6.8\mu M$
- Primer 2 — $6.8\mu M$
- Taq polymerase — $5u/100\mu L$
- PCR buffer — $1\times$
- Water

PCR was then carried out on a PTC-100 Peltier Thermal Cycler (MJ Research). The protocol took into consideration that the fluid would see room temperature between cycles, as it moves over the regions that are over bulk silicon. The protocol used was 40 cycles of $40s$ at $94°C$, $52.5°C$, $20s$ at $72°C$, and $40s$ at $25°C$

The SMZ-1000 stereo microscope (Nikon), a P-FLA Fluorescence Attachment (Nikon) with a 31001 FITC filter (Chroma Technology Corp), an X-Cite 120 Fluorescence Illumination System (Exfo), and a MicroMAX 1300YHS CCD Camera

(Princeton Instruments, Roper Scientific Inc.) was used to detect fluorescence. The parameters are listed below:

- Camera exposure — $30s$
- Microscope zoom — $2\times$
- Light source intensity — Maximum (100%)

The products were verified using gel electrophoresis. The results of the gel confirmed that PCR was carried out successfully.

The Matlab script, `acqback.m` (Section C.1.1), was used to acquire the background noise floor of the CCD. `imfocus.m` (Section C.1.2) was then used to monitor and save images of the intensity profile. The intensities are measured on a 16-bit linear scale. The baseline level was found to be 35 with a standard deviation of about 5, with water in the channels.

Firstly, the pre-PCR reagents were first pumped into a fluidic channel dummy (fluidic layer on nitride dummy) and allow to sit, and imaged. The average intensity was found to be 470.44 with a standard deviation of 10.1. The resultant image is show in Figure 5–4.

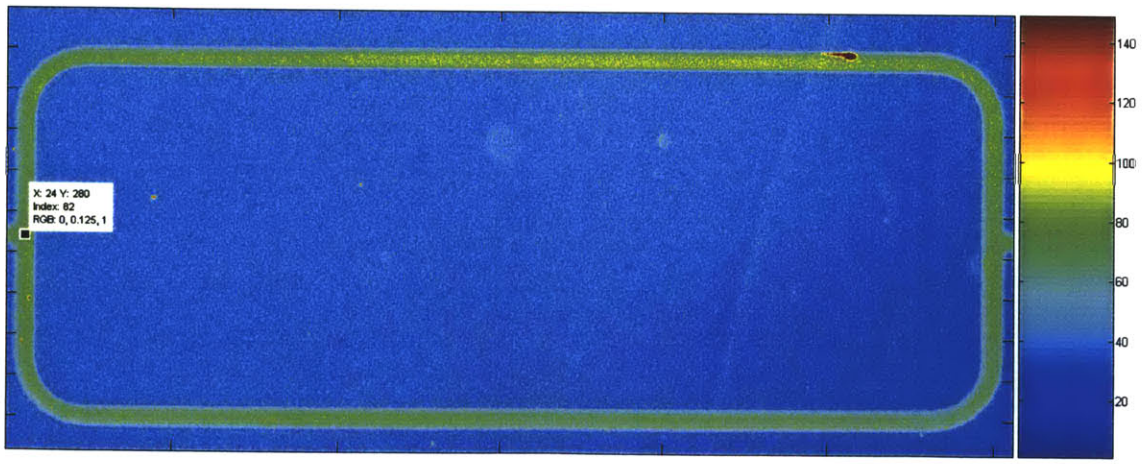

Figure5–4: Fluorescent intensity profile of pre-PCR reagents.

Secondly, the loop is flushed with water and imaged. The intensity profile returned

to the initial background. This shows that there is undetectable residual DNA or reagents left in the fluidic channels. The image is shown in Figure 5–5.

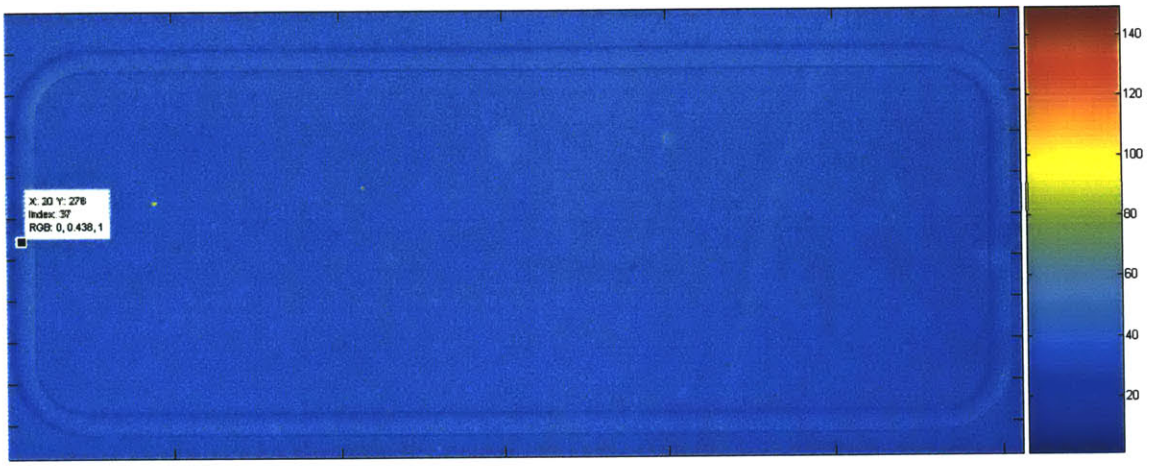

Figure5–5: Fluorescent intensity profile after flushing out reagents.

Thirdly, the post-PCR product was pumped into the loop and imaging was carried out. The average intensity measured was 93.43, and the standard deviation was 17.06. This was a 65% increase in intensity compared to the pre-PCR reagents. The image is shown in Figure 5–6.

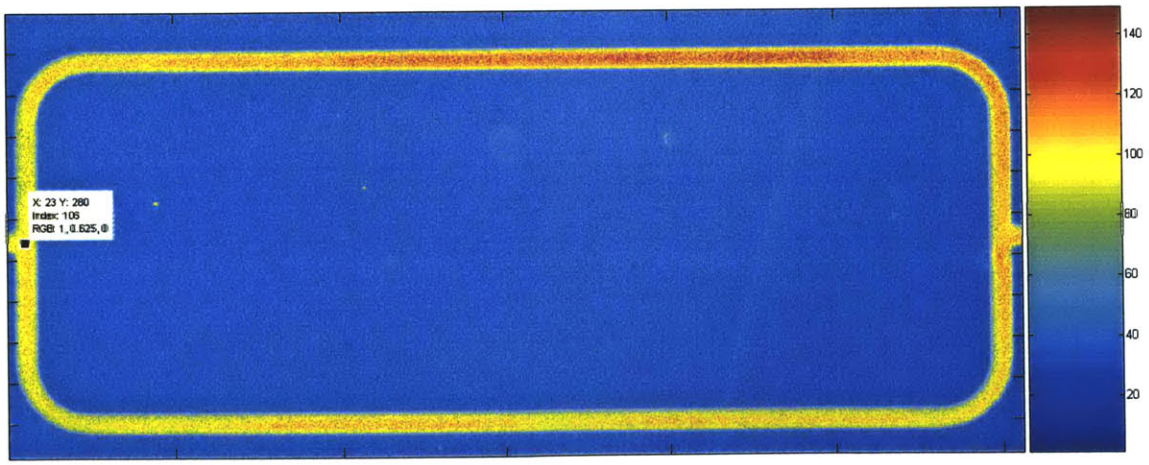

Figure5–6: Fluorescent intensity profile of post-PCR products.

Finally, the fluidic channel loop is flushed yet again, to show that the intensity profile returned to the baseline again. The image is shown in Figure 5–7.

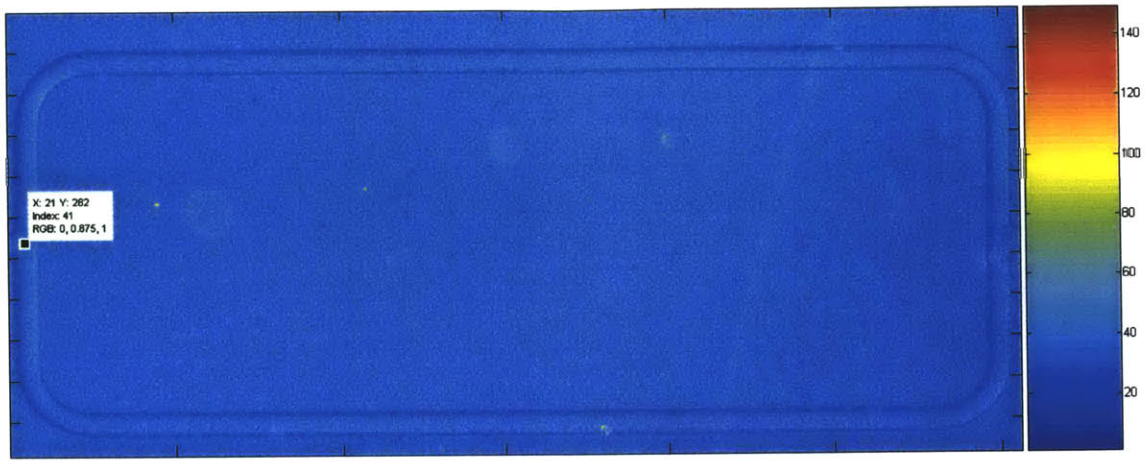

Figure5–7: Fluorescent intensity profile after final rinse.

In conclusion, the PCR product was successfully detected in the fluidic channels using the fluorescent dye SYBR Green I. Therefore, this method can be applied to validating successful on-chip PCR reactions.

5.2 Implanted Heaters

The implanted heaters were successfully characterized. The results obtained from heaters fabricated using the improved process, as discussed in Section 4.2.2, showed significantly improved characteristics, that were more consistent and closer to the theoretical predictions.

5.2.1 Electrical characterization

The electrical characterization consisted of measuring the resistance of the heaters and determining the actual I-V curves. An amplifier circuit was build to amplify the signal output from a NI-DAQ PCI-MIO-16XE-50 card (National Instruments). This was used to step through voltages while a 428 Current Amplifier (Keithley Instruments Inc.) was used to measure the current passing through the heater. This shows the linearity of the I-V curves and the resistance can be obtained from the slope of the curve. Figure 5–8 shows the curves of all the heaters on one of the Cobra-Lite

dies with $20\mu m$ wide heaters.

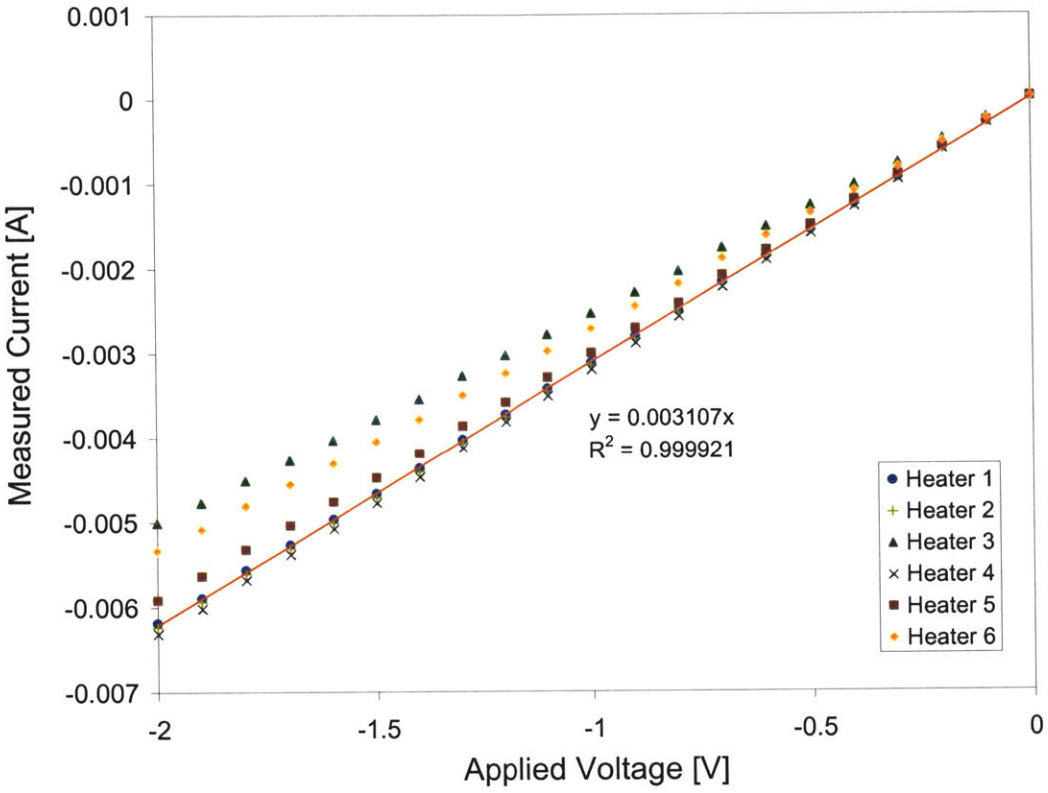

Figure 5–8: I-V curves of six resistors on a single device after using the improved fabrication process.

Characterization of devices from the initial fabrication run revealed heaters with extremely high resistances. Often it was not possible to measure the resistances on a multimeter. However, devices fabricated from the improved fabrication process (Section 4.2.2) showed much better attributes. The resistance of the heaters were actually measurable using a multimeter, and Table 5.5 shows the comparison between the derived resistance from the I-V curves and the measurements obtained using a multimeter.

The electrical characterization of the heaters has been completed successfully. The heaters from the new process were much more consistent, with resistances that varied by only $\pm 10\%$ within the same device.

Resistor #	Ohm Meter [Ω]	Curve fit from I-V Curves [Ω]
1.	315.8	321.9
2.	312.7	319.2
3.	387.5	396.8
4.	308.1	314.9
5.	328.6	336.0
6.	362.5	371.8

Table 5.5: *Comparison of resistance measurements*

5.2.2 Temperature measurements using thermochromic crystals

Thermochromic liquid crystals (TLC) were initially used to characterize the temperature profile in the channels. The TLC changes temperature with temperature, depending in the bandwidth of the type of crystals. The NSL-33 Liquid Crystal Slurries (Liquid Crystal Resources, L.L.C.) used had bandwidths of $5°C$. One starts to change color at $38 - 43°C$ and the other at $90 - 95°C$. Both samples were tested in the microfluidic channels.

After flow the crystals through the fluidic channels, initial temperature profiles were obtained and the heating of fluids could be observed as voltage supplied to the heaters was increased. The images captured are shown in Figure 5–9.

However, the size of the crystals vary between $5 - 15\mu m$ in diameter. They readily clog up the device and cannot be removed. Therefore, the device cannot be used after the characterization.

Moreover, the spatial resolution of the crystals is rather bad. Since coverage of the surface is inversely related to the amount of water in the channels, the difference in physical properties might reduce the accuracy of the measurements

Finally, the measurement is based on color, which is difficult to quantify. Therefore, a better method was needed to carry out the temperature characterization.

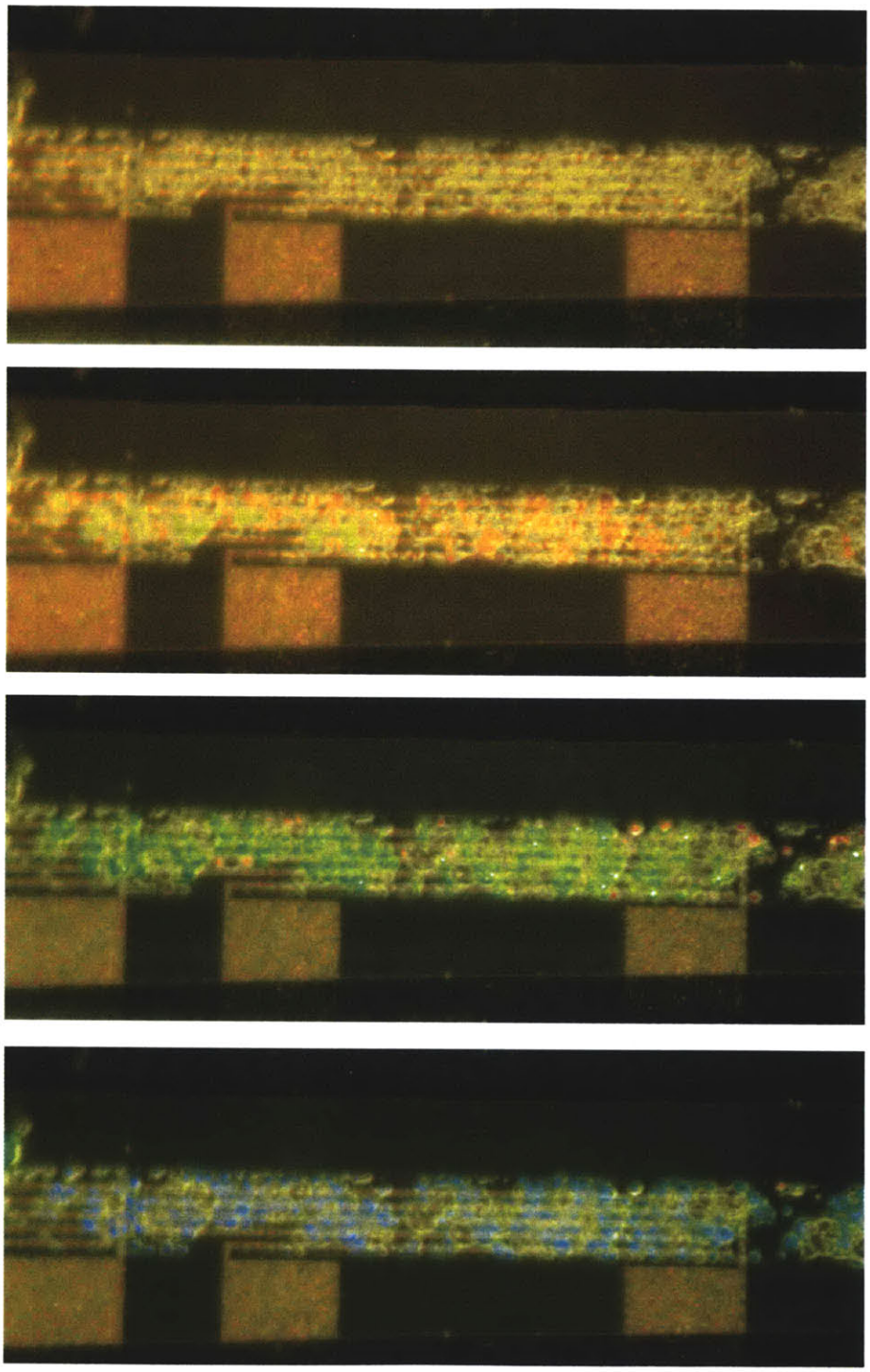

Figure 5–9: The color change of thermochromic dyes as temperature increases in the fluidic channels is shown. These crystals are colorless at below $90°C$ (top) and as temperature increases, they turn red, then green, and finally blue at $90°C$ (bottom).

5.2.3 Temperature measurements using a fluorescent dye

The use of a temperature sensitive fluorescent dye to determine the spatial temperature profile in the microfluidic channels has many advantages. This method has been demonstrated both in the macro by Finegan [7] and the micro scale environment by Ross [15].

This method allows the temperature of fluid in the channels to be measured accurately because the fluorescent dye is dissolved in a water based buffer. Therefore the thermal characteristics of the system will be similar to that for the actual reactions. Also the dye can be easily flushed out of the channels without any clogging. Finally, the fluorescence of the dye continuous and therefore spatial resolution is limited by the optics and camera resolution.

The dye used, D-1824, Dextran-rhodamine B Conjugate, $10000MW$ (Molecular Probes Inc.), has a good linear response in the temperature range of interest. It has an absorbtion peak at $570nm$ and an emission peak at $590nm$.

However, the fluidic channels have a semicircular cross-section (Figure 4–6). Therefore the distribution of the dye across the channel is not constant. Imaging from vertically above, there is more dye in the center of the channel than at the sides. It can also be observed that there is significant variation in the height of the channels that would affect the fluorescence intensity readout. Therefore a ratiometric approach is needed, in order to eliminate the spatial distribution of dye concentration. An initial image is taken at room temperature and the subsequent images taken are divided by the initial image to normalize the intensity. The normalized intensity is then converted to temperature using an empirically determined calibration curve.

The SMZ-1000 stereo microscope (Nikon), a P-FLA Fluorescence Attachment (Nikon) with a 41002 TRITC filter (Chroma Technology Corp), and an X-Cite 120 Fluorescence Illumination System (Exfo) was used to excite and capture the fluorescence of the dye. The filter set allowed an emission spectrum of $510 - 560nm$ and absorbtion spectrum of $572.5 - 647.5nm$.

Initial measurements were carried out with a Coolpix 4500 Digital Camera (Nikon).

The data confirmed the temperature dependance of the Rhodamine-B dye, however it was not sufficient for quantitative characterization of the heaters. The images obtained had poor spatial resolution of about $10\mu m^2$. Also the low sensitivity of camera required the use of long exposure times to actually detect any fluorescence. Finally, the built-in image processing of the camera resulted in non-linearity of the image intensities. Therefore, a scientific grade CCD camera was required for quantitative measurements.

The MicroMAX 1300YHS CCD Camera (Princeton Instruments, Roper Scientific Inc.) was used in place of the digital camera. The increased sensitivity, linearity to intensity and resolution made it possible for the spatial mapping of the temperature in the fluidic channels. The experimental parameters are listed below:

- Dye concentration — $0.5mM$ in $7.2pH$ PBS buffer
- Camera exposure — $500ms$
- Camera temperature — $-20°C$
- Microscope zoom — $2\times$
- Light source intensity — Maximum (100%)

The initial data was captured using the camera's proprietary software WinView32 ver 2.5.8.1 (Roper Scientific Inc.), which was then imported into Matlab (The MathWorks) for data analysis. This was slow and cumbersome.

Using drivers provided by Roper Scientific Inc., Matlab scripts were written to communicate with the camera controller, thus allowing images to be acquired directly into Matlab. This allowed for the realtime update of images using the `imfocus.m` script (Section C.1.2).

An image centering script, `imcenter.m` (Section C.1.3), was written to align the image captured with the image of the initial intensity, when calculating the intensity ratio. This helped to eliminate spatial variation through vibrations and small shifts in the microscope of equipment. The program accounts for lateral shifts in the x

and y directions but rotation about the $z - axis$ is assumed to be negligible. Due to the semicircular profile, the fluorescence intensity is greatest at the middle of the channel. Therefore, by searching for the maximum intensity from the middle of the image, across the sum of the rows and columns, the image can then be accurately centered. Implementation of the script significantly reduced the noise and was critical in achieving measurements with temperature accuracy of $1 - 5°C$.

The temperature calibration curve was empirically determined. A dummy fluidic device is clamped to a hotplate, and the fluorescent dye is flowed into the channels. T-type thermocouples were clamped to the surface of the chip and a HH506R Digital Thermometer (Omega Technologies Co.), was used to monitor the temperature.

First, 20 consecutive background images are taken with all shutters closed, using the script `acqback.m` (Section C.1.1) The background is an image of the intrinsic noise of the camera and the average image of the 20 will be subtracted from all images taken.

Next the temperature of the hotplate is slowly ramped up, and images are taken at every $5°C$ interval. At each temperature, the system is allowed to equilibrate for a $5min$. The shutter for the light source is then opened and 20 consecutive images are taken. The temperature reading from the thermocouple is noted. This was carried out from room temperature ($23.5°C$) to $85°C$, in $5°C$ steps and then back down to room temperature again.

The data obtained was then processed with `imratio.m` (Section C.1.4). The script loads a target directory and automatically does the background subtraction, and ratiometric calculations to determine the actual intensity ratio and related statistics. A threshold is imposed to filter out all pixels that are outside of the fluidic channels and only pixels with intensities above the threshold are considered for the analysis. The result is a good ratiometric temperature measurement with a $5°C$ accuracy, as shown in Figure 5–10.

However, since the temperature measurement is based on an initial intensity profile, the calibration curve is only valid for the particular initial temperature. There-

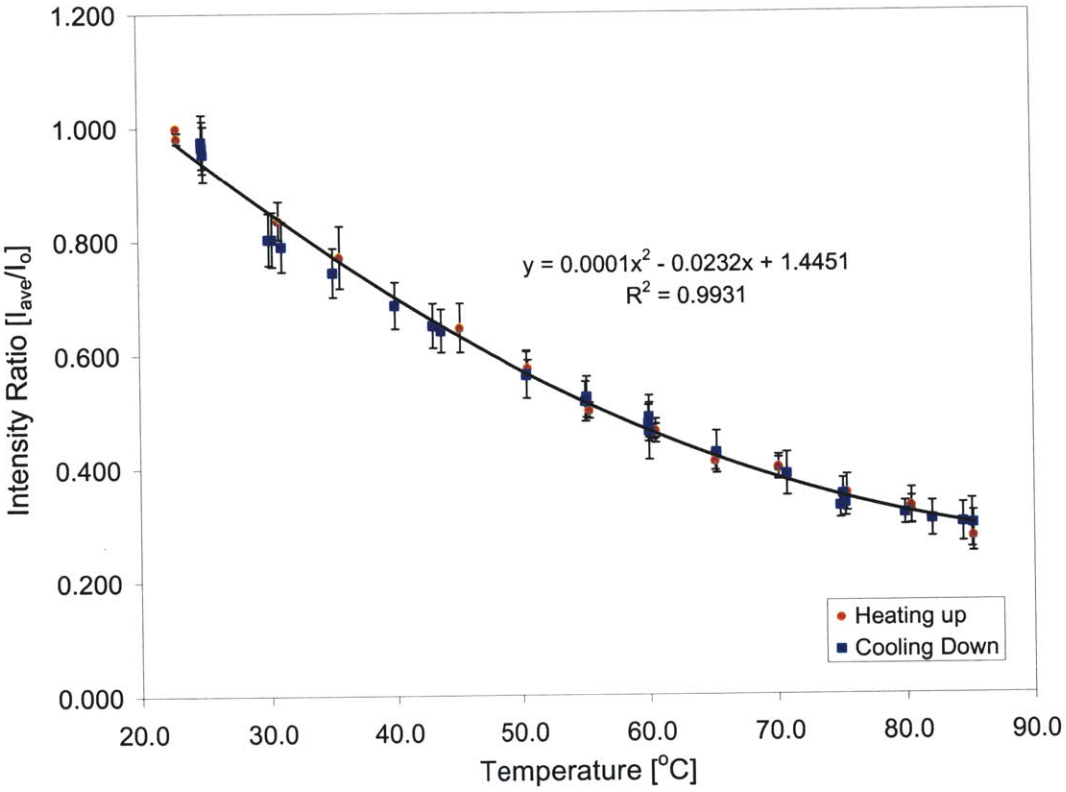

Figure 5–10: Fluorescence thermal measurement for temperature mapping, using rhodamine-B.

fore, the calibration curve needs to be shifted to account for differences in room temperatures. The derivation of the conversion factor is shown as follows:

$$IR_T^m = \frac{I_T}{I_{To}} \tag{5.1}$$

Where IR_T^m is the measured intensity ratio, I_T is the intensity at temperature T, and I_{T_o} is the initial intensity at room temperature.

$$IR_T = f(T) = C_2T^2 + C_1T + C_0 \tag{5.2}$$

Where the intensity ratio is a function of the temperature, $f(T)$, as determined empirically (Figure 5–10). However, when the room temperature is shifted to T_{o_2},

$$IR_T^m = \frac{I_T}{I_{To_2}} \tag{5.3}$$

The new conversion function, $g(T)$ can be expressed as,

$$g(T) = \frac{I_T}{I_{To_2}} = \frac{I_T}{I_{To}} \cdot \frac{I_{To}}{I_{To_2}} = \frac{f(T)}{f(I_{To_2})} \tag{5.4}$$

Therefore, the conversion factor is simply $1/f(T_{o_2})$. The temperature can then be determined from the inverse function,

$$T = g^{-1}(IR_T^m) \tag{5.5}$$

`tempccurve.m` (Section C.2.3) was written to automatically calculate the inverse function and scale it for the actual room temperature.

Once the calibration curve had been determined, `tmap.m` (Section C.2.2) was written to run the real-time temperature mapping, in Matlab. The experimental setup is the same as that for the dye calibration experiments. First an average background is taken using `acqback.m` (Section C.1.1). Next, the average reference image at room temperature is taken using `acqio.m` (Section C.2.1). Once the initial reference data has been obtained, the real-time temperature mapping can be carried out. The image refreshes at $2Hz$, and the program allows the image to be stored.

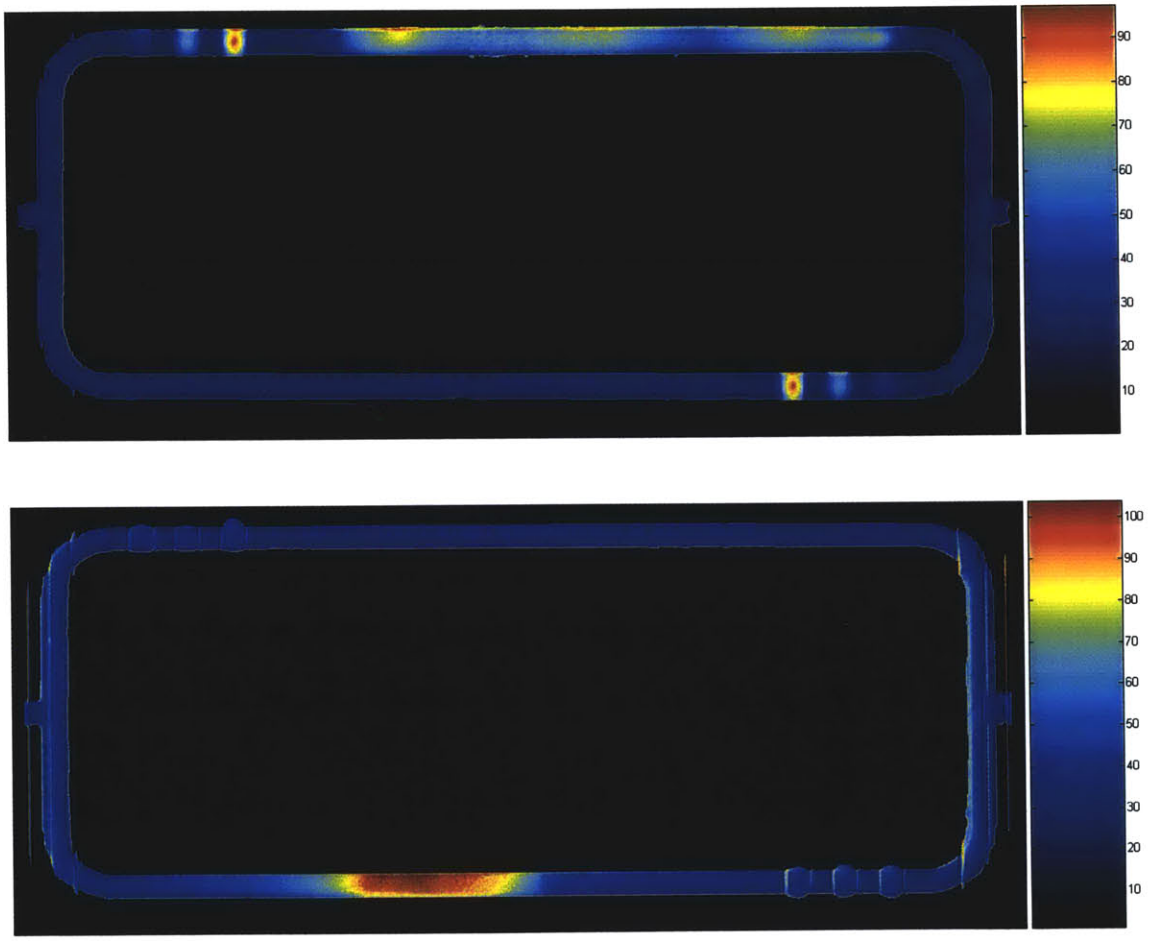

Figure5–11: Images saved from real-time temperature mapping, showing the spatial temperature profile in the microfluidic channels.

The real-time spatial temperature mapping of the microfluidic channels was achieved. However heating causes the water in the channels to evaporate and diffuse into the PDMS. When this happens, the PDMS becomes cloudy, which reduces the actually fluorescence detected. This would cause the temperature reported to be higher than the actual temperature in the channels. Therefore, more optimization of the heaters will have to be carried out for actual reactions.

During all the characterization, it became evident that the thermal isolation of the suspended heaters was excellent, as seen in Figure 5–11. Even when the fluid is heated to high temperatures, it falls off rapidly in the channels, and substrate still remains at room temperature. As a result of the thermal isolation, the power required in heating up the fluids is very low due to the small thermal mass. Only $30mW$ at $5V$ was required to boil water in the channels.

Another advantage of the thermal isolation was the fast response of the heaters as a result of the small thermal mass. The temperature response of the fluid, to changes in the voltage supplied to the heaters, was virtually instantaneous in both heating up and cooling down. This observation is consistent with the results of the transient response from the lumped thermal model in Section 2.2.

5.3 Electronic Field-Effect Sensors

The field-effect sensors were characterized using a flow through system. This allows the injection of all types of reagents. The sensors successfully detected buffer injections of different pH as well as the deposition of poly-electrolyte layers.

5.3.1 Experimental setup

The packaged device is plugged in to a PCB that breaks out the connections allowing connections to the various equipment. The substrate of the device is biased at $2V$, using a E3615A DC Power Supply (Agilent Technologies). The signal electrode is driven at $4kHz$ ($10mV$ signal about $0V$) with a DS345 Synthesized Function Generator (Stanford Research Systems Inc.). And each sensor is connected to a 428

Current Amplifier (Keithley Instruments Inc.). The current amplifier allows control over the bias voltage on the backside of the senor, while it measures the current flowing through the sensors. The output of the current amplifiers are sent to SR830 DSP Lock-In Amplifiers (Stanford Research Systems Inc.) and the signals are read using Labview.

The sensors are very sensitive to both light and other disturbances. As such, silver-silver chloride ground electrodes are introduced into the flow path, before and after the device to isolate it from ambient disturbances. Also, the device is shielded from light during experiments.

A running buffer is constantly pumped over the sensors using a "Genie" syringe pump (Kent Scientific). The flow rate can be accurately controlled, and typical flow rates are $2 - 20\mu m$. An AS-4000 Intelligent Auto Sampler (Hitachi) is then programmed to inject a plug of reagent, with a designated volume $(5 - 100\mu L)$into the flow. Peek tubing (Upchurch Scientific) of various inner diameters are inserted directly into the PDMS to deliver the fluids into the device. The fluidic channels used are single layered PDMS with $100\mu m \times 100\mu m$ channels.

5.3.2 Buffer injections

The sensors were first characterized by injecting buffers of different pH. The difference in charge in the buffer can be detected by the sensors and there is no surface binding involved. This is the most basic test of for the sensors, and is used as an initial evaluation of performance for new sensors.

The running buffer used is $10mM$ phosphate citrate buffer. This buffer allowed the injection of buffers with the same ionic strength but different pH, thereby isolating the solution effect that was being measured.

The pH sensitivity of the sensors were good, and a typical injection curve is shown in Figure 5–12. The signal to noise ratio is good and the sensitivity of $38.8mV$ per pH unit.

The detection range of the sensors was also tested by injecting consecutive buffer injections of pH ranging from $2.2-7.4pH$ at $0.4pH$ intervals. The sensors successfully

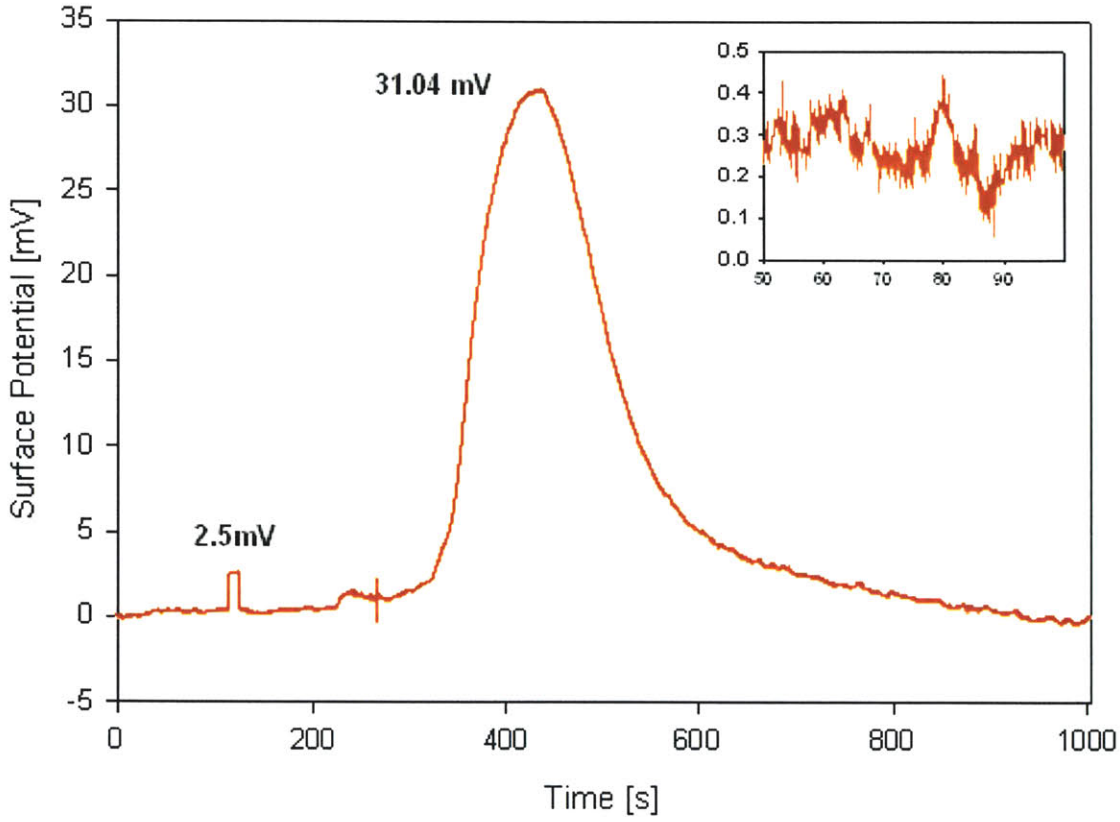

Figure 5–12: The sensor has a good sensitivity of $38.8mVpH^{-1}$, to an injection of $+0.8pH$, with good signal to noise ratio as shown in the insert.

detected the whole range of pH, as shown in Figure 5–13.

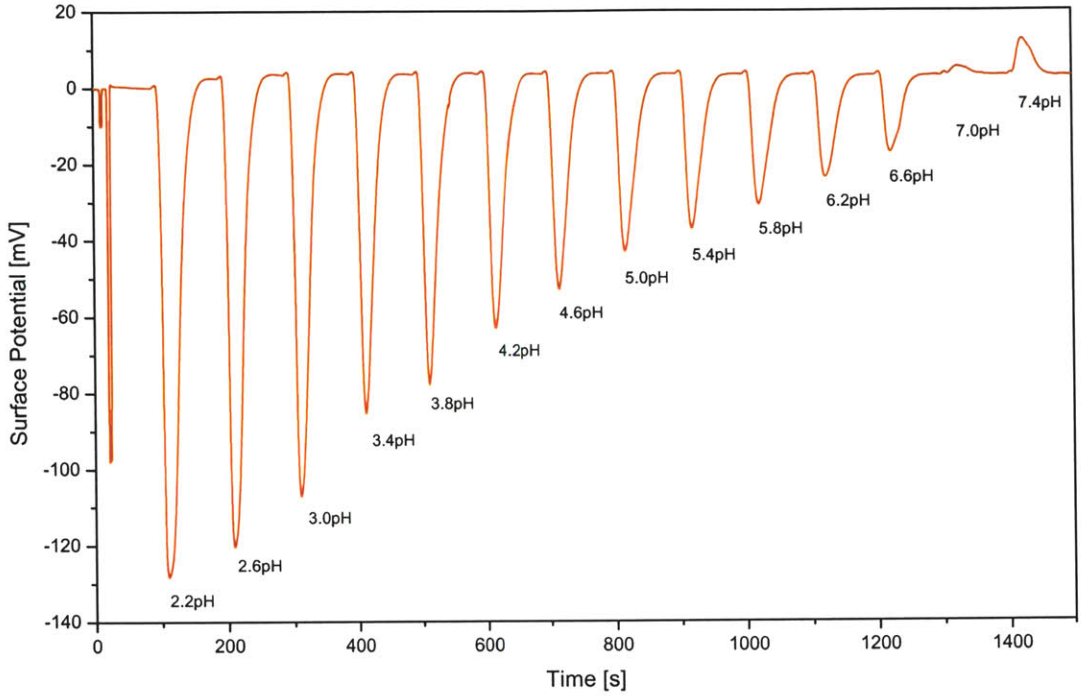

Figure 5–13: Sensor response to multiple buffer injections from $2.2pH$ to $7.4pH$, showing an even response over a large pH range.

Over the course of using buffer injections to evaluate sensors, it was discovered that the weak buffers age when left in glass vials for too long. This effect depends greatly on the buffer capacity, and it is therefore prudent to mix fresh samples from concentrates. Figure 5–14 clearly shows the distinction between buffer that was allowed to sit for a day and buffer that was freshly prepared. Consecutive injections of the aged buffer, followed by an injection of freshly prepared buffer, proves that the buffer does indeed deteriorate. It also shows that the sensors are extremely sensitive and can detect minute changes.

After more detailed tests, it was determined that plastic inserts were more inert than the glass vials. When using glass vials for weak buffers, it is important to rinse the vials with the buffer before filling them with the actual sample. However, plastic inserts are more suitable for sensitive measurements.

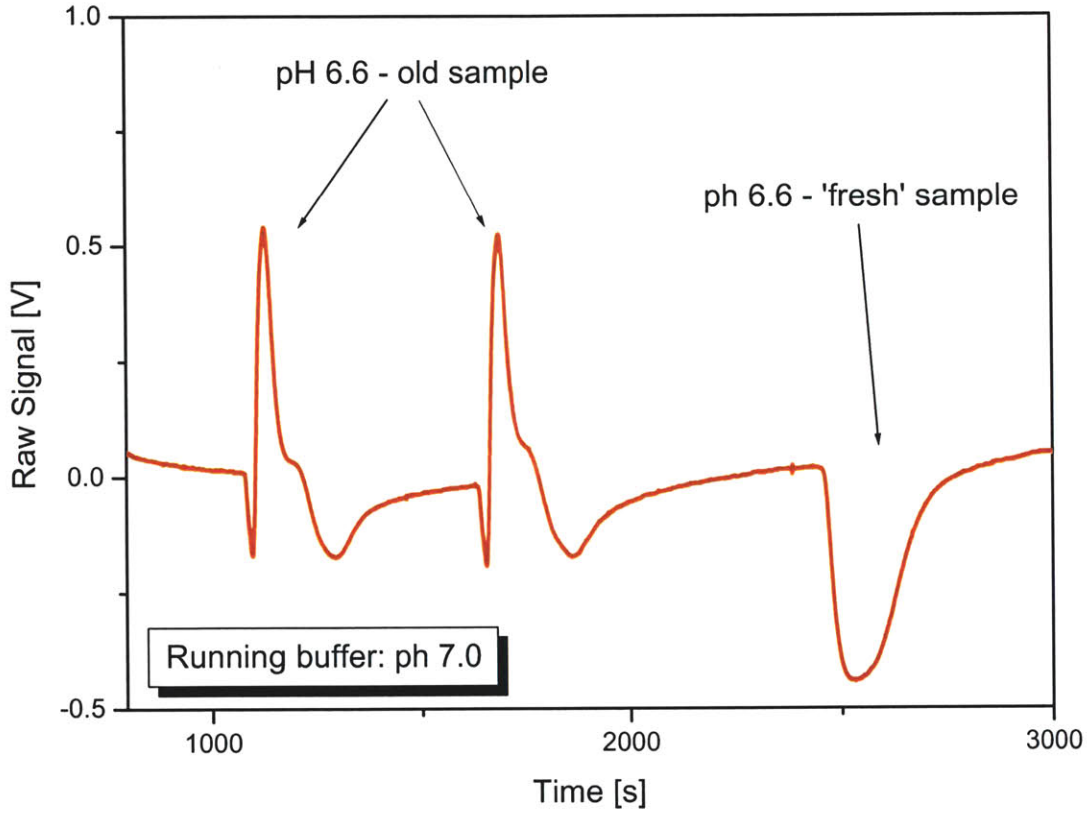

Figure 5–14: The sensor response to old buffer versus the freshly prepared buffer, has shown that weak buffers will age in glass vials.

The characterization of sensor with buffer injections has been completed and the sensitivity of the sensors to detecting changes to solution has been successfully demonstrated.

5.3.3 Poly-electrolyte injections

The detection of deposited charged layers on filed effect sensors has been demonstrated with previous generation sensors by Cooper [6] and Fritz et al. [8]. The deposition of the poly-electrolytes, such as poly-l-lysine (PLL) and poly-l-glutamatic acid (PLG), on the sensor surface cause the surface charge to change and this can be detected by the field effect sensor. Also, the charged layers could potentially be used as non-specific binders for detection of molecules or as control surfaces.

The poly-electrolytes are prepared by dissolving them in the flow buffer at a concentration of $0.1 mgmL^{-1}$. This eliminated any other effects that could be detected by the sensors. The buffer flow rate was $5\mu L min^{-1}$ and the sample injection was $50\mu L$, allowing a surface exposure of $10 min$.

The sensors are first tested with buffer injections to determine functionality and sensitivity of the sensors (Section 5.3.2). The clean silicon oxide surface is then exposed to an injection of PLL. The highly positive PLL adsorbs to the surface, and after the plug is flushed off, the remaining PLL on the surface modulates the depletion region of the sensor, and it shows as a shift in the baseline, as shown in Figure 5–15 On injecting a second plug of PLL, there is no baseline shift after the plug has been flushed away, since there is no additional binding of PLL to the surface.

The surface of the sensor are now saturated with the highly positively charged PLL. Therefore on injecting the negatively charged PLG, it adsorbs to the surface and this can be observed in Figure 5–16, as the base line shift. Once again, the injection of the second plug shows no baseline shift.

The curves also allow the visualization of the two effects during the injection of poly-electrolytes. The first effect of the charged molecules binding to the surface can be seen in the baseline shift after flushing off the initial injection. However on the second injection, there is still a signal observed during the injection. This is the effect

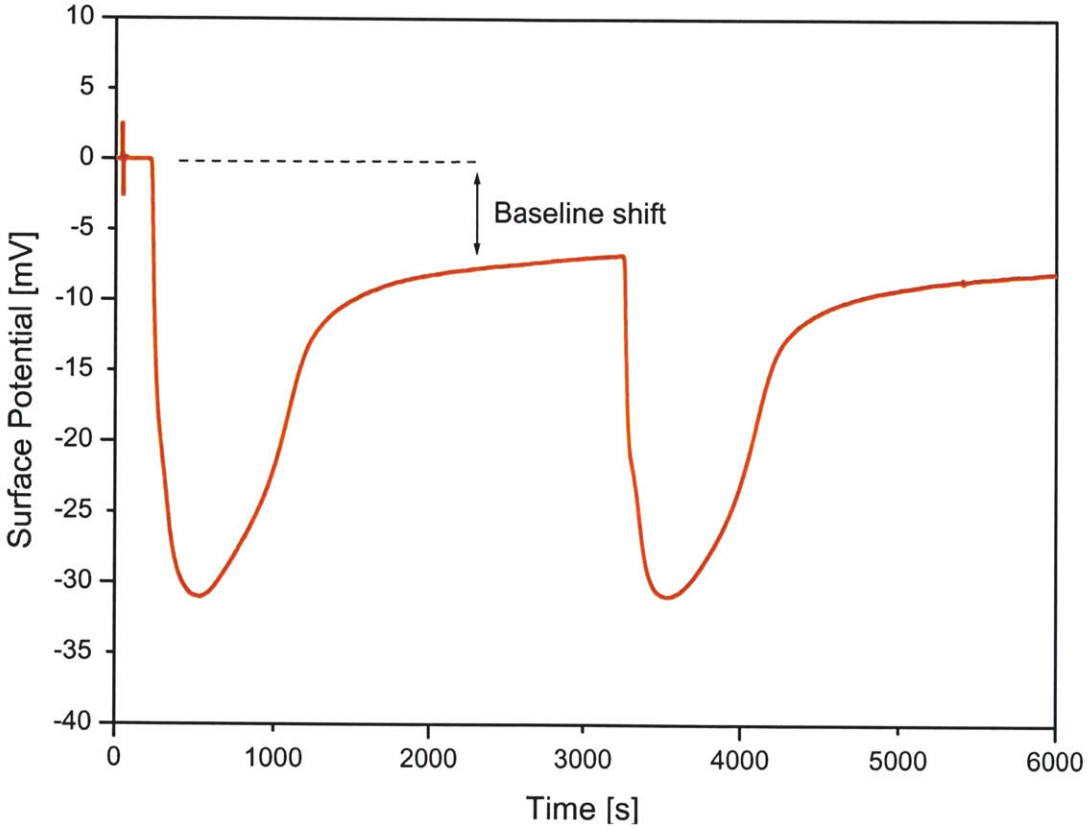

Figure 5–15: Sensor response to injection of poly-lysine onto silicon oxide surface, showing binding on the first injection and no binding on the second injection.

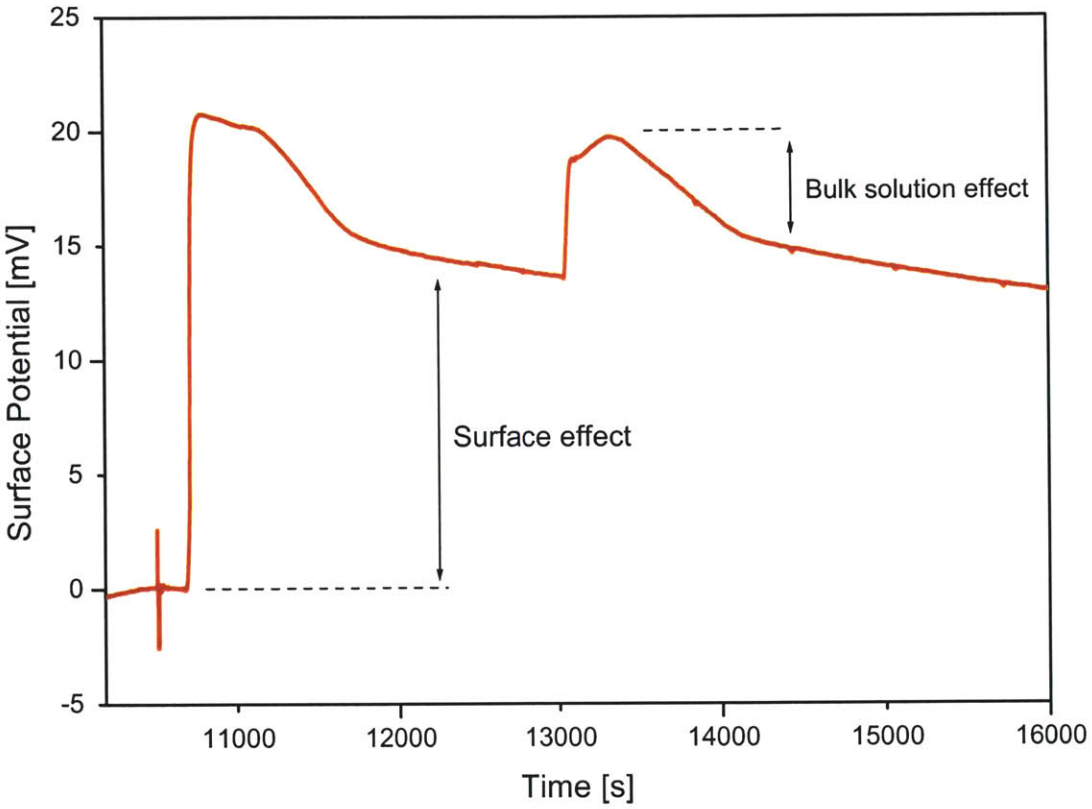

Figure5–16: Sensor response to injection of poly-glutamate onto a poly-lysine coated surface, showing the combination of surface binding and bulk solution effects on the first injection and only the bulk solution effect on the second injection.

of the poly-electrolyte in the bulk solution. After flushing, the baseline remains the same and there is no surface effect observed, as consistent to no binding of molecules to the surface.

The detection of binding of charged molecules has been successfully demonstrated on the sensors. Therefore, the sensors are ready for more complicated surface modifications and specific detection of charged molecules.

Chapter 6

Conclusion

This thesis has explored the integration of microfluidics, on-chip heaters, and field effect sensors, for such applications. In particular, the device was designed for the purpose of integrated amplification and label-free detection of DNA.

The good thermal isolation of the heaters has many benefits, such as reduced power consumption. Also, this device allows for good control over the temperature zones. The multiple heaters available on the different designs also allow for better resolution control of the the temperature profiles. However this comes at a cost of having thin membranes that are fragile, which significantly increases the complexity of device fabrication. The calibration of the heaters can also be tedious depending on the quality of heaters fabricated.

Finally, the most notable contribution of the device is the integration of field effect sensors, that allow direct electrical readout of fluidic monitoring, with on-chip fluidic manipulation and thermally isolated heaters. This device paves the way for future integration of multiple microfluidic components, for lab-on-a-chip applications.

6.1 Thesis Contributions

The integration of microfluidics, heaters and sensors has been successfully accomplished. The inherited fabrication process was updated and the improvements implemented have greatly increased both the yield of functional devices and the quality of

the devices.

Characterization of microfluidic valves and pumps in PDMS allow accurate manipulation of fluids on chip. The successful optical detection of PCR products on-chip provides a platform for validating the device for the actual PCR reaction.

The electrical testing of the heaters was carried out and it showed that the modified fabrication process improved the yield and quality of the heaters. Temperature measurements using thermochromic crystals was explored and determined to be inadequate for the system. The measurement of fluid temperature in microfluidic channels, using fluorescent dyes was then successfully implemented. This allowed for realtime spatial imaging of the temperature profile in the microfluidic channels.

Finally, the functionality of the sensors were validated using buffer injections. The sensors showed good sensitivity and signal to noise ratios. They were then applied successfully to detect the absorption of poly-electrolytes to sensor surfaces.

6.2 Future Work

Through working with engineering the device, there are a few challenges that have become evident for future work to explore. Currently, the different components and setups have been developed and are fully functional. However significant work will still be required to get the integrated device running as a complete system, in order to carry out the amplification and detection of DNA.

The microfluidic setup using PDMS is versatile, but it does not provide chemical robustness that is required for use with harsh chemicals during sensor surface cleaning and regeneration. Integration of the device with glass fluidics could be an option to be explored to improve on this aspect.

Although the device was designed for a specific purpose, there are other relevant applications such as chemical synthesis. It would be most beneficial to explore these other opportunities and broaden the applicability of the integrated platform that has been developed.

Appendix A

Initial Fabrication Process

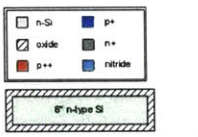

Wafer Info:
50-75 ohm-cm
600-650um thickness

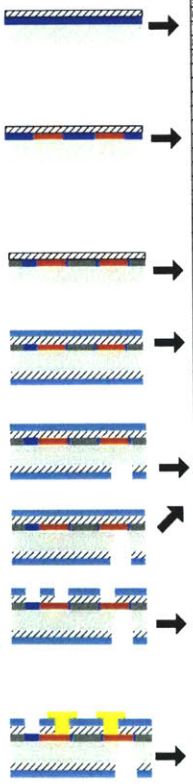

	Process	Where	Machine	Notes
1	HMDS	ICL	coater6	Alignment Marks
	spin-coat 2um photoresist	ICL	coater6	
	prebake	ICL	coater6	
	photolithography – mask 0	TRL	EV1	
	develop	TRL	photo-wet-l	
	postbake	TRL	postbake	30mins @120C
2	etch Si, 5000A	ICL	LAM490B	selectivity ~ 5:3; black silicon recipe, 8100A measured
3	ash photoresist	ICL	asher	3mins
4	clean w/ Piranha	ICL	pre-metal	
5	RCA clean	ICL	rca	
6	300A thermal oxide	ICL	5B-anneal	1050C
7	p+ ion implantation	-	Innovion	dose=5e12 energy=100kev
8	Piranha x2	TRL	acid-hood	
9	HMDS	ICL	coater6	
	spin-coat 2um photoresist	ICL	coater6	
	prebake	ICL	coater6	
	photolithography – mask 1	TRL	EV1	p++ mask
	develop	TRL	photo-wet-l	
	postbake	TRL	postbake	30mins @120C
10	p++ ion implantation	-	Innovion	dose=1e16 energy=100kev
11	Piranha x2	TRL	acid-hood	
12	ash photoresist	ICL	asher	4 mins
13	HMDS	ICL	coater6	
	spin-coat 2um photoresist	ICL	coater6	
	prebake	ICL	coater6	
	photolithography – mask 3	TRL	EV1	n+ mask
	develop	TRL	photo-wet-l	
	postbake	TRL	postbake	30mins @120C
14	n+ ion implantation	-	Impant Science	dose=5e15 energy=125kev
15	Piranha x2	TRL	acid-hood	
16	ash photoresist	ICL	asher	4 mins
17	BOE	ICL	oxEtch-BOE	60sec (etch rate ~700A/min)
18	RCA clean	ICL	rca	
19	300A thermal oxide	ICL	5B-anneal	1050C 440A in center, 320A at edge measured.
20	Dopant Drive/Long anneal	ICL	5B-anneal	1050C in N2 for 70 mins.
21	10,000A nitride	ICL	VTR	9100-9350A measured
22	HMDS	ICL	coater6	Coated both sides of wafer for this photo step
	spin-coat 2um photoresist	ICL	coater6	
	prebake	TRL	prebakeoven	30 minutes @ 90C
	photolithography – mask 4	TRL	EV1	
	develop	TRL	photo-wet-l	touch up with Q-tip
	postbake	TRL	postbake	30mins @ 90C
23	etch nitride (backside)	ICL	AME5000	
24	ash photoresist	ICL	asher	4 mins 2x on each side
25	KOH backside etch	ICL	Manalis lab	
26	Piranha x2	TRL	acid-hood	This step was accidentally skipped
27	HMDS	TRL	HMDS	
	spin-coat 10um photoresist	TRL	coater	Thick resist. AZ4620. Recessed chuck
	prebake	TRL	prebakeoven	
	photolithography – mask 5	TRL	EV1	No vacuum
	develop	TRL	photo-wet-l	
	postbake	TRL	postbake	30mins @120C
28	etch nitride	Manalis	RIE	O2 / CF4 mixture
29	Piranha x2	TRL	acid-hood	remove photoresist
30	HMDS	TRL	HMDS	
	spin-coat 2um photoresist	TRL	coater	Recessed chuck. Image reversal resist.
	prebake	TRL	prebakeoven	30mins @ 90C
	photolithography - mask 6	TRL	EV1	20s
	flat bake	TRL	hotplate	90s @ 120C
	flood exposure	TRL	EV1	45s
	develop	TRL	photo-wet-l	
31	ash photoresist	TRL	asher	descum
32	BOE	TRL	acid-hood	30sec (pre-clean for metal)
33	evaporate 200A Ti, 5000A Au	TRL	e-beam-Au	200A Ti, 1000A Au
34	Ti/Au liftoff w/ acetone	TRL	photo-wet-Au	

Appendix B

Fabrication Masks

B.1 Microfluidic Fabrication

B.1.1 First generation microfluidic dies and mask layouts

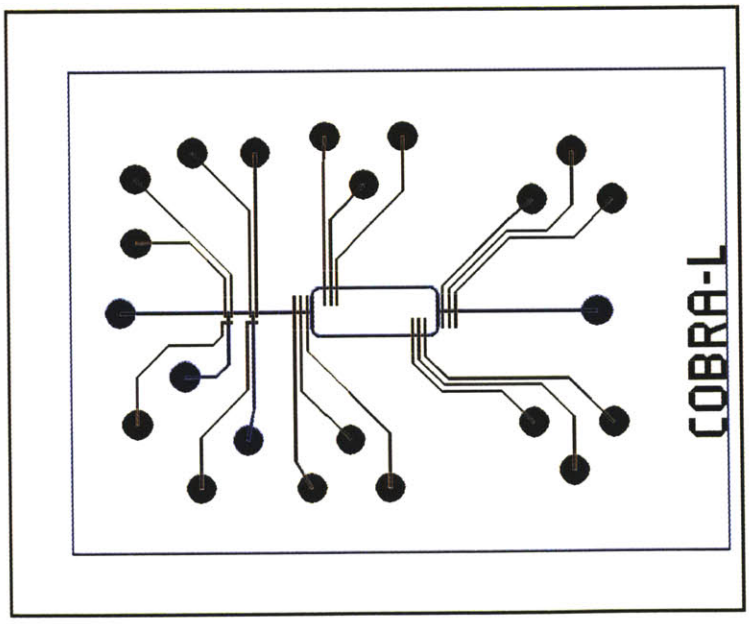

FigureB–1: Cobra-Lite Microfluidics

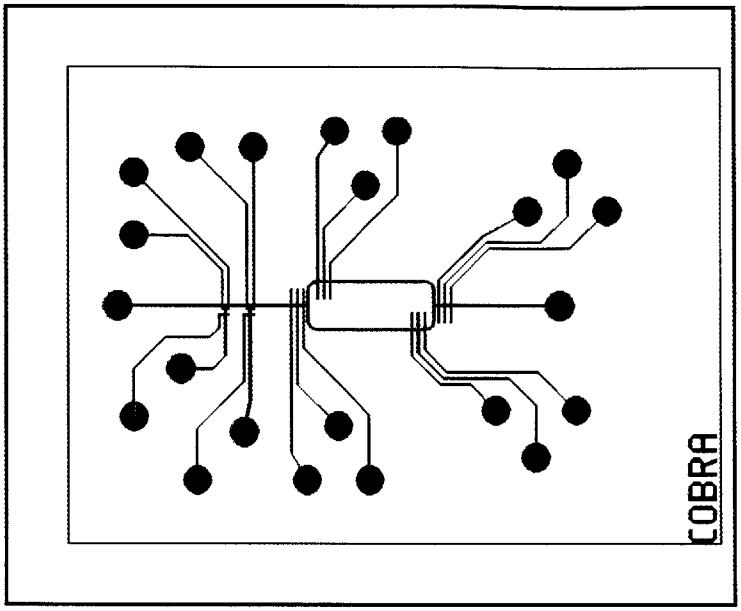

FigureB–2: Cobra Microfluidics

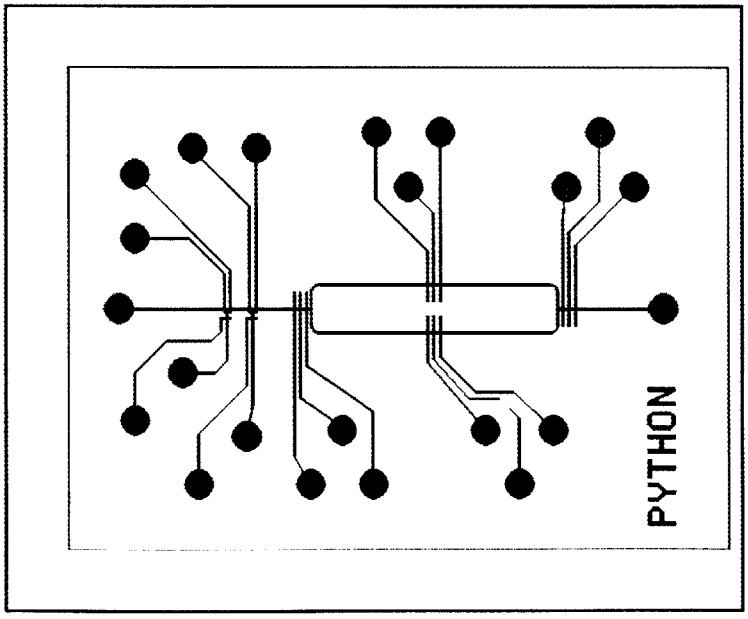

FigureB–3: Python Microfluidics

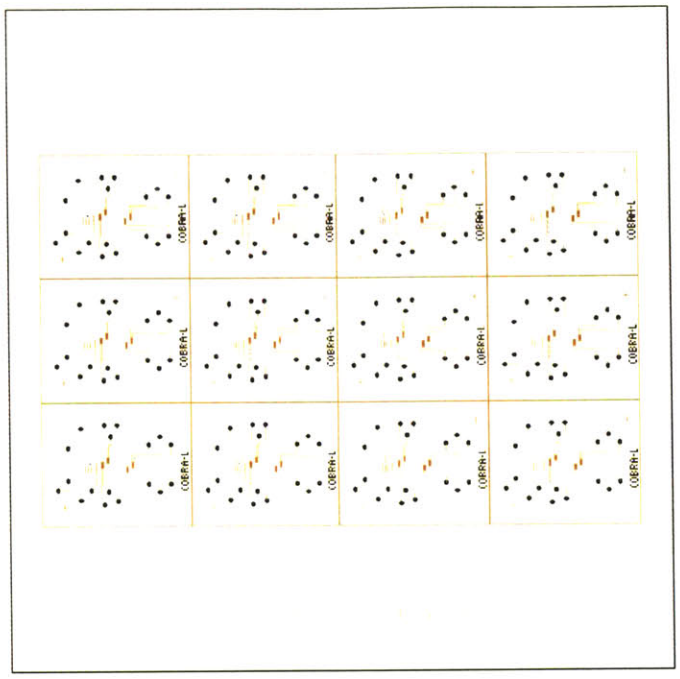

FigureB–4: Cobra-Lite Controls Layer Mask Layout

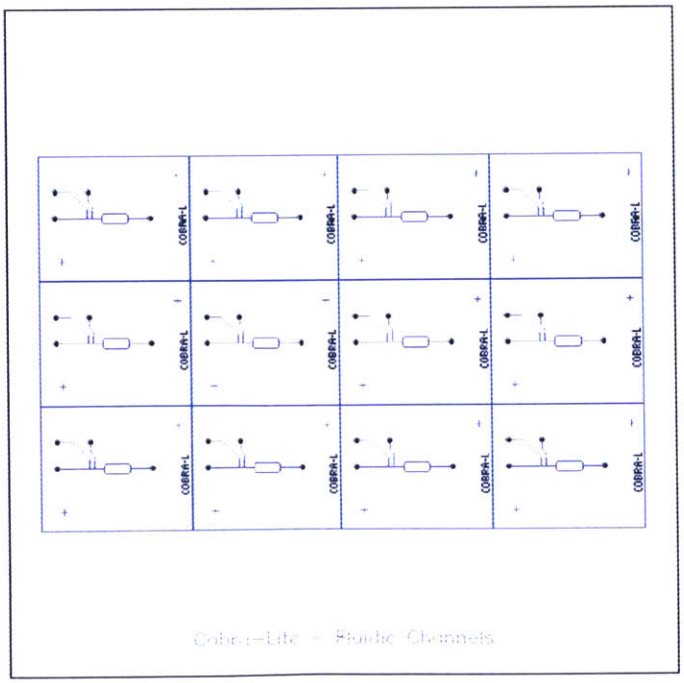

FigureB–5: Cobra-Lite Fluidic Layer Mask Layout

B.1.2 Second generation microfluidic dies and mask layouts

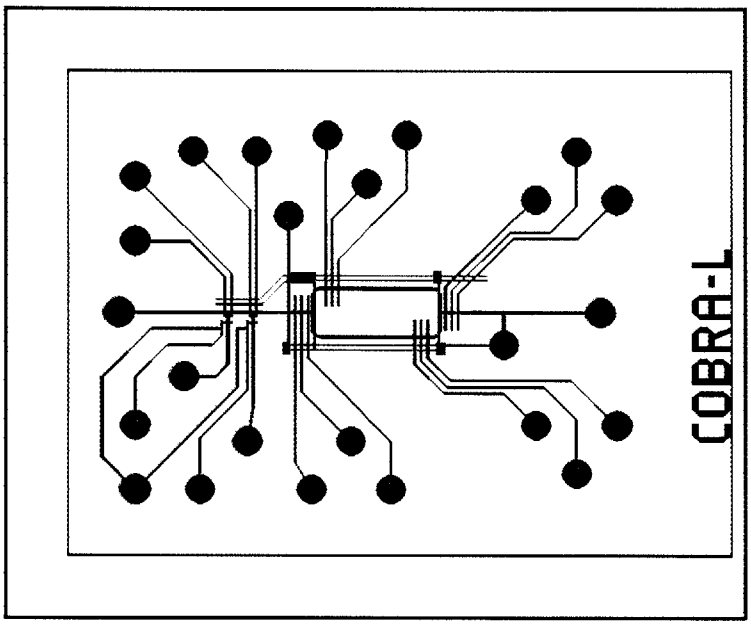

FigureB–6: Cobra-Lite Microfluidics II

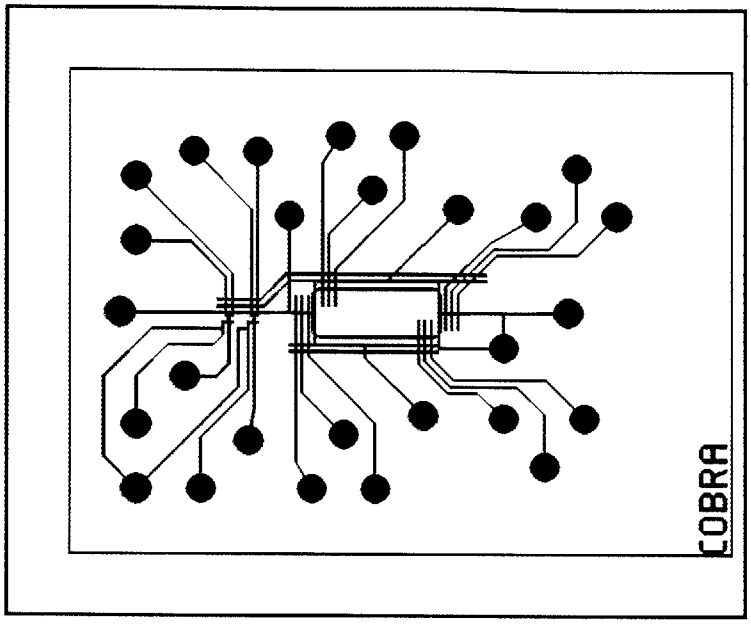

FigureB–7: Cobra Microfluidics II

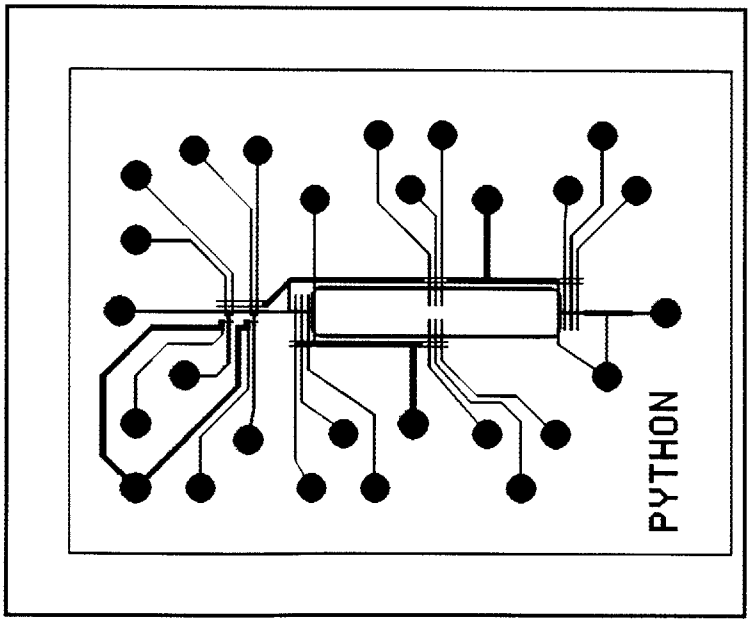

FigureB–8: Python Microfluidics II

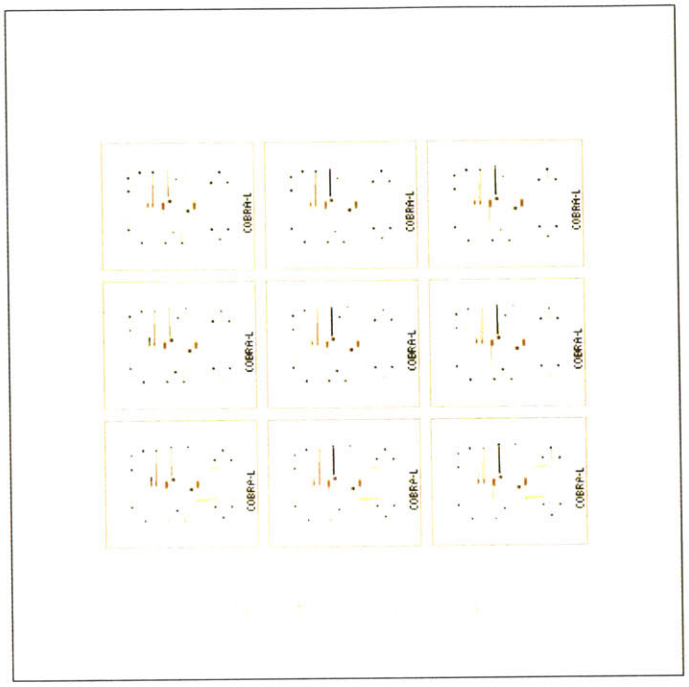

FigureB–9: Cobra-Lite II Controls Layer Mask Layout

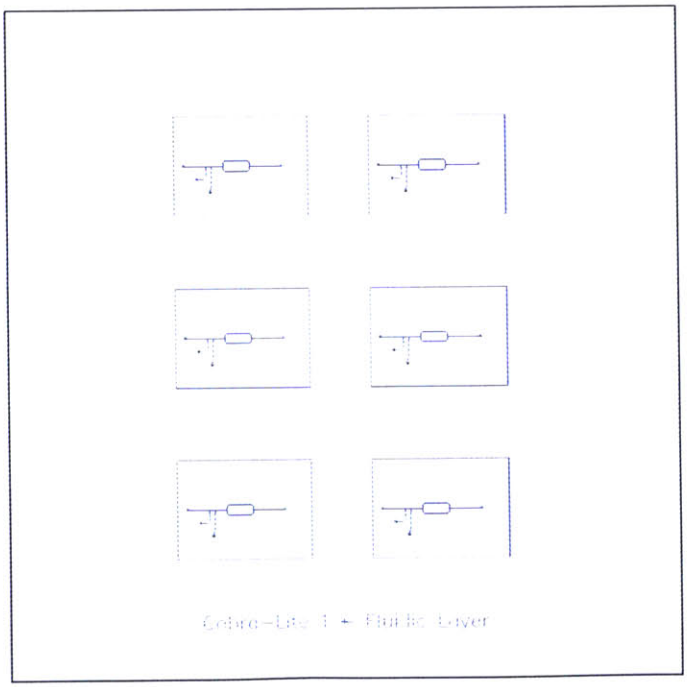

FigureB–10: Cobra-Lite II Fluidic Layer Mask Layout

B.1.3 Final generation microfluidic dies and mask layouts

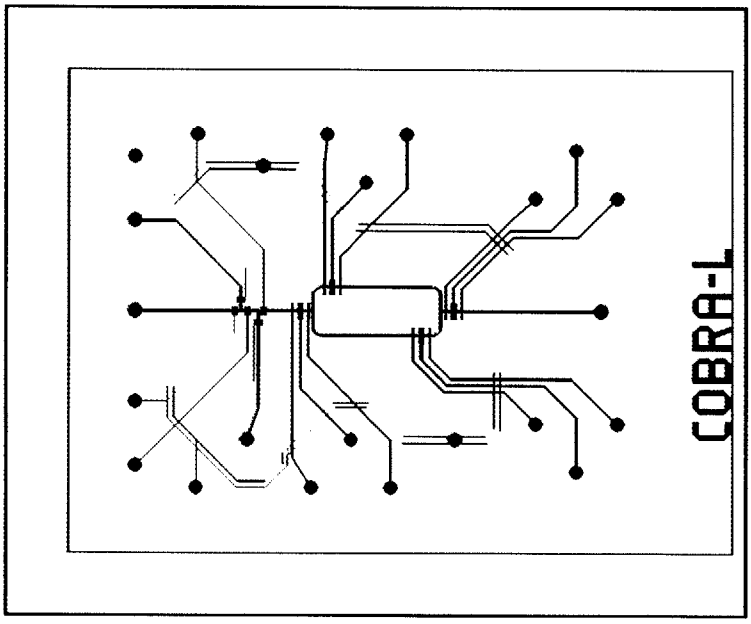

FigureB–11: Cobra-Lite Microfluidics III

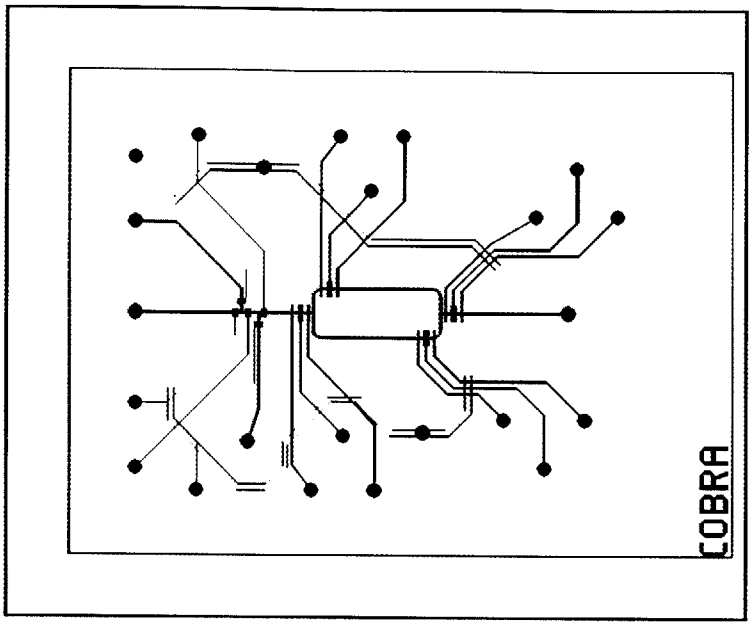

FigureB–12: Cobra Microfluidics III

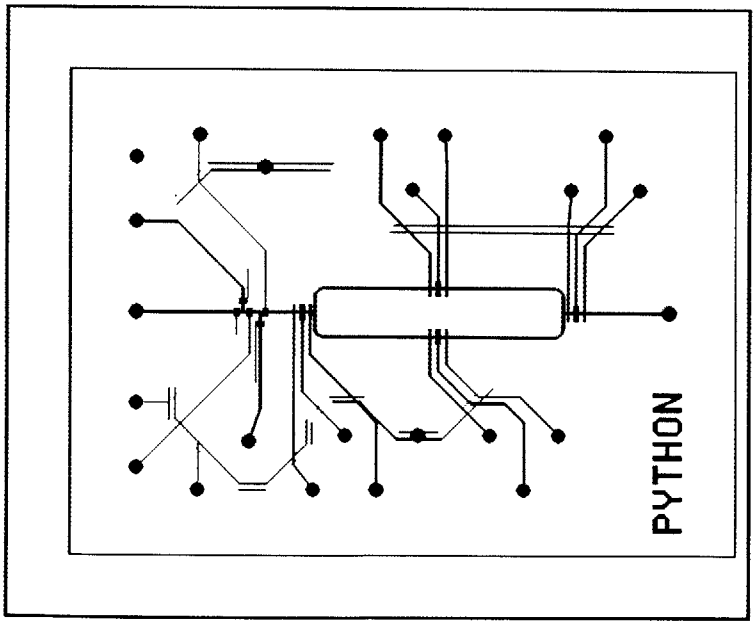

FigureB–13: Python Microfluidics III

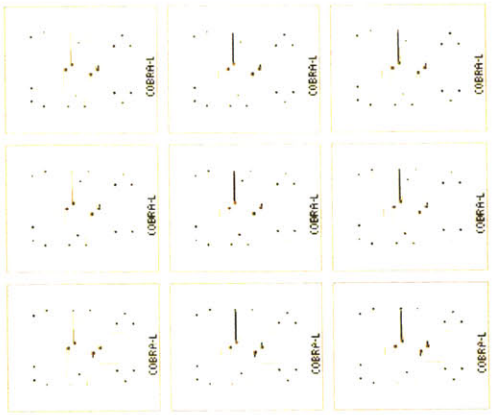

FigureB–14: Cobra-Lite III Controls Layer Mask Layout

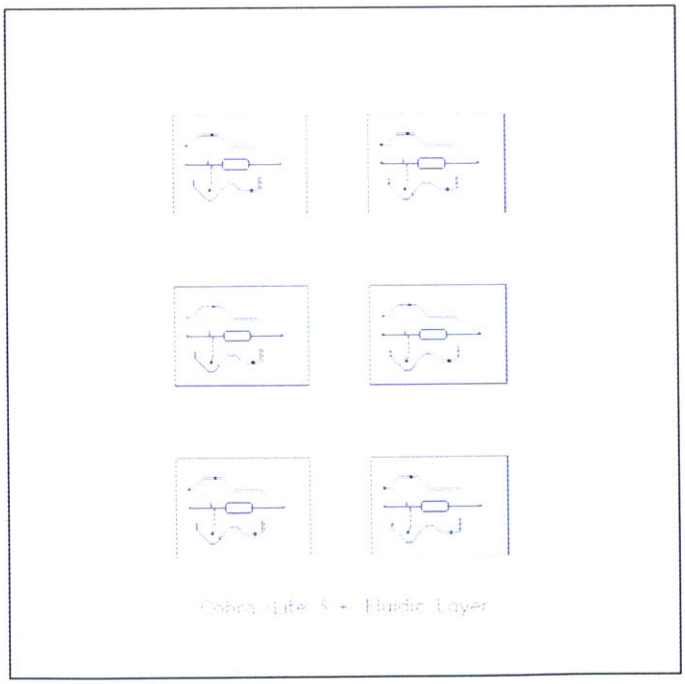

FigureB–15: Cobra-Lite III Fluidic Layer Mask Layout

B.2 Silicon Fabrication

B.2.1 Initial mask set dies

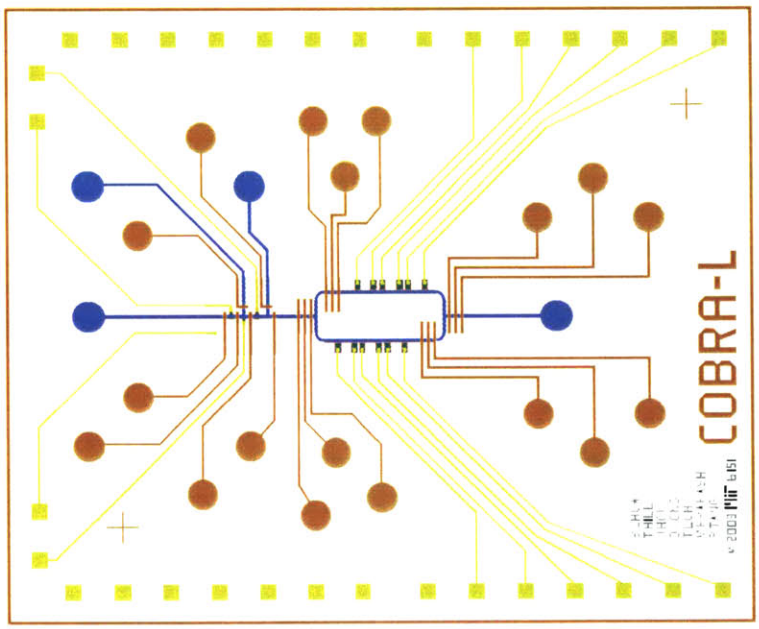

FigureB–16: Initial Cobra-Lite die

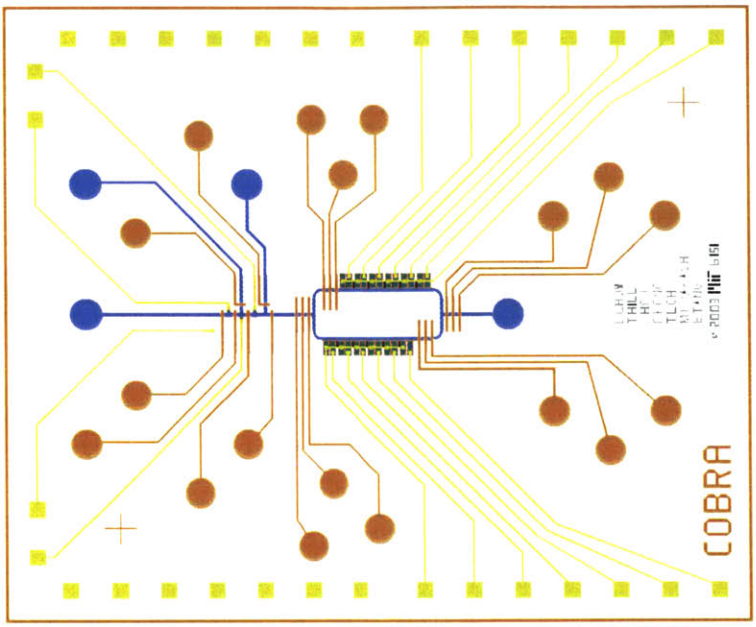

FigureB–17: Initial Cobra die

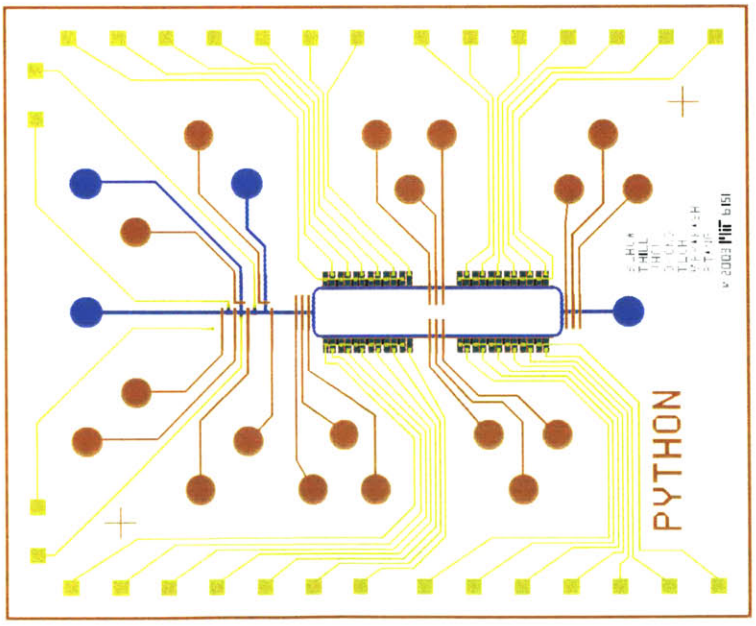

FigureB–18: Initial Python die

B.2.2 Final mask set dies

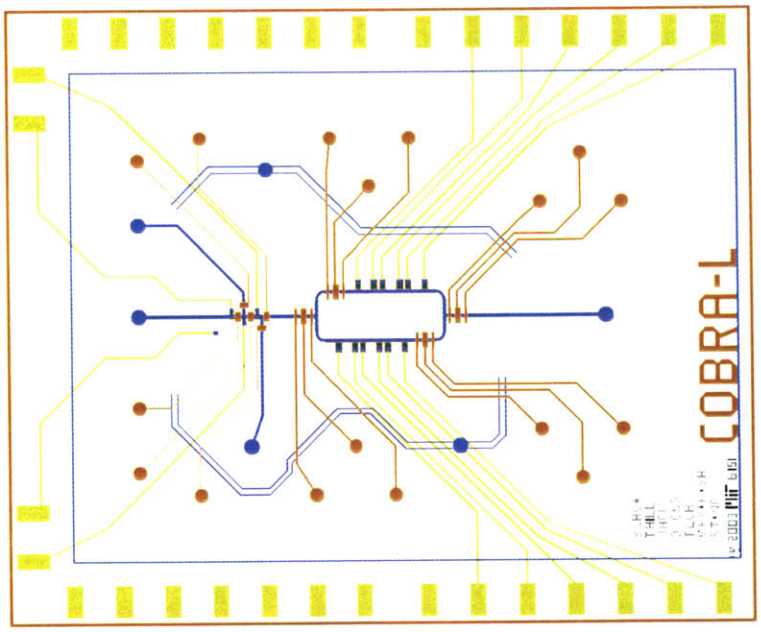

FigureB–19: Final Cobra-Lite die

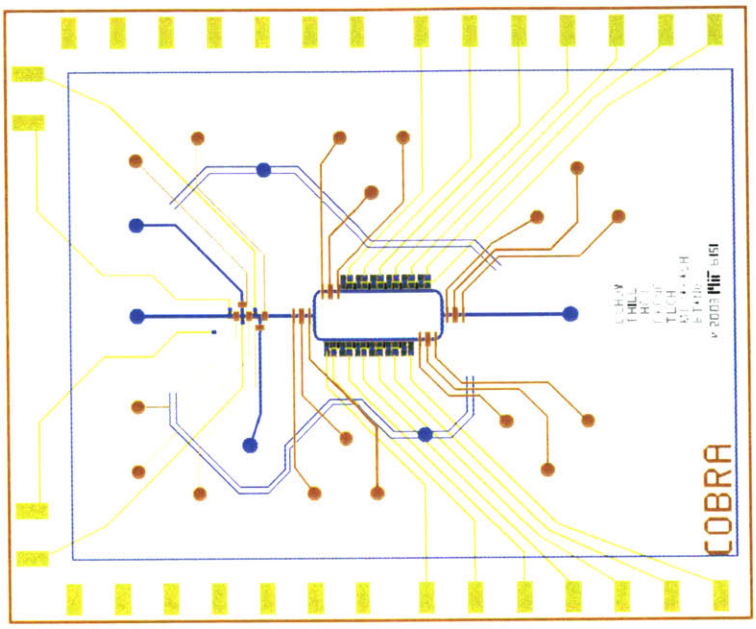

FigureB–20: Final Cobra die

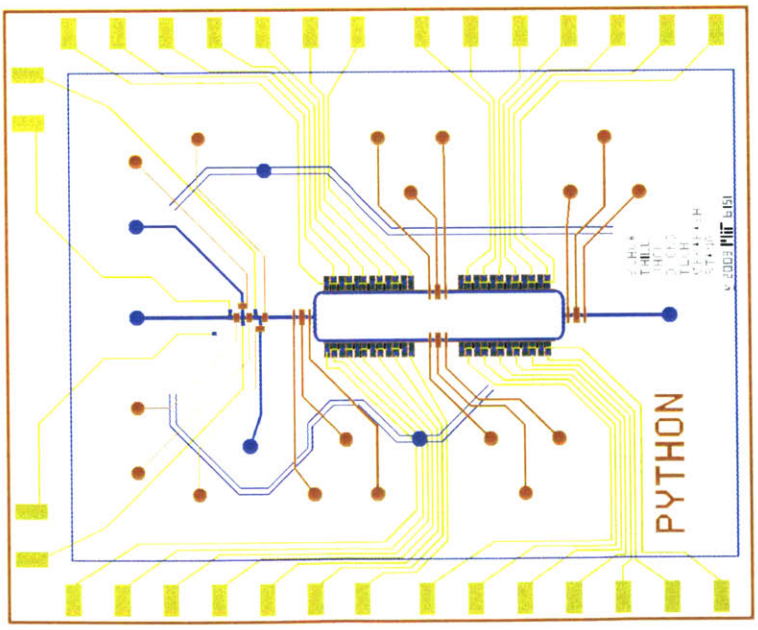

FigureB–21: Final Python die

B.2.3 Wafer layout and other features

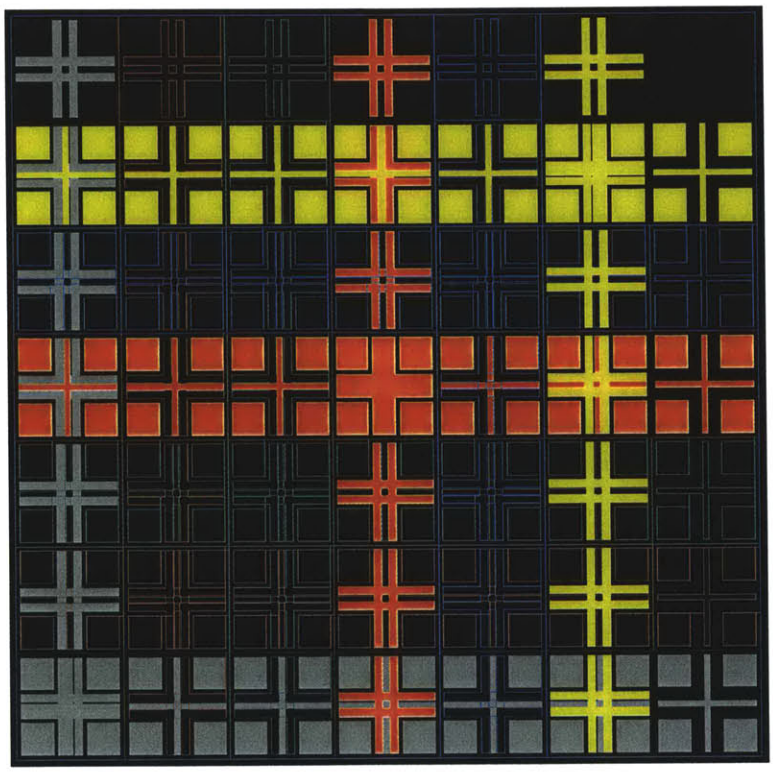

FigureB–22: Alignment Marks

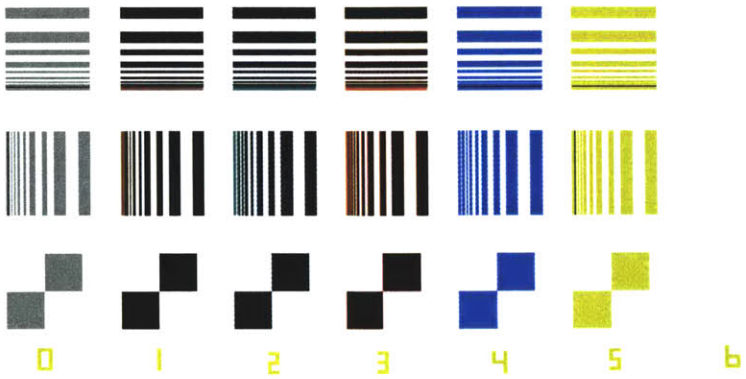

FigureB–23: Lithography inspection patterns

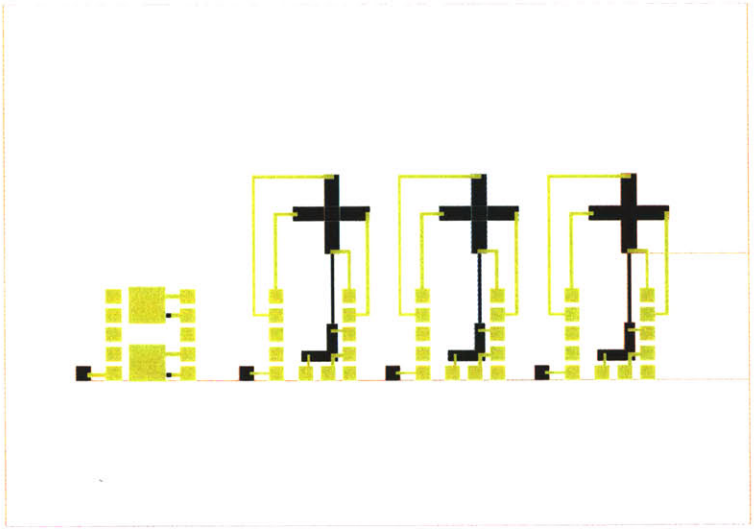

FigureB–24: Implant test structures

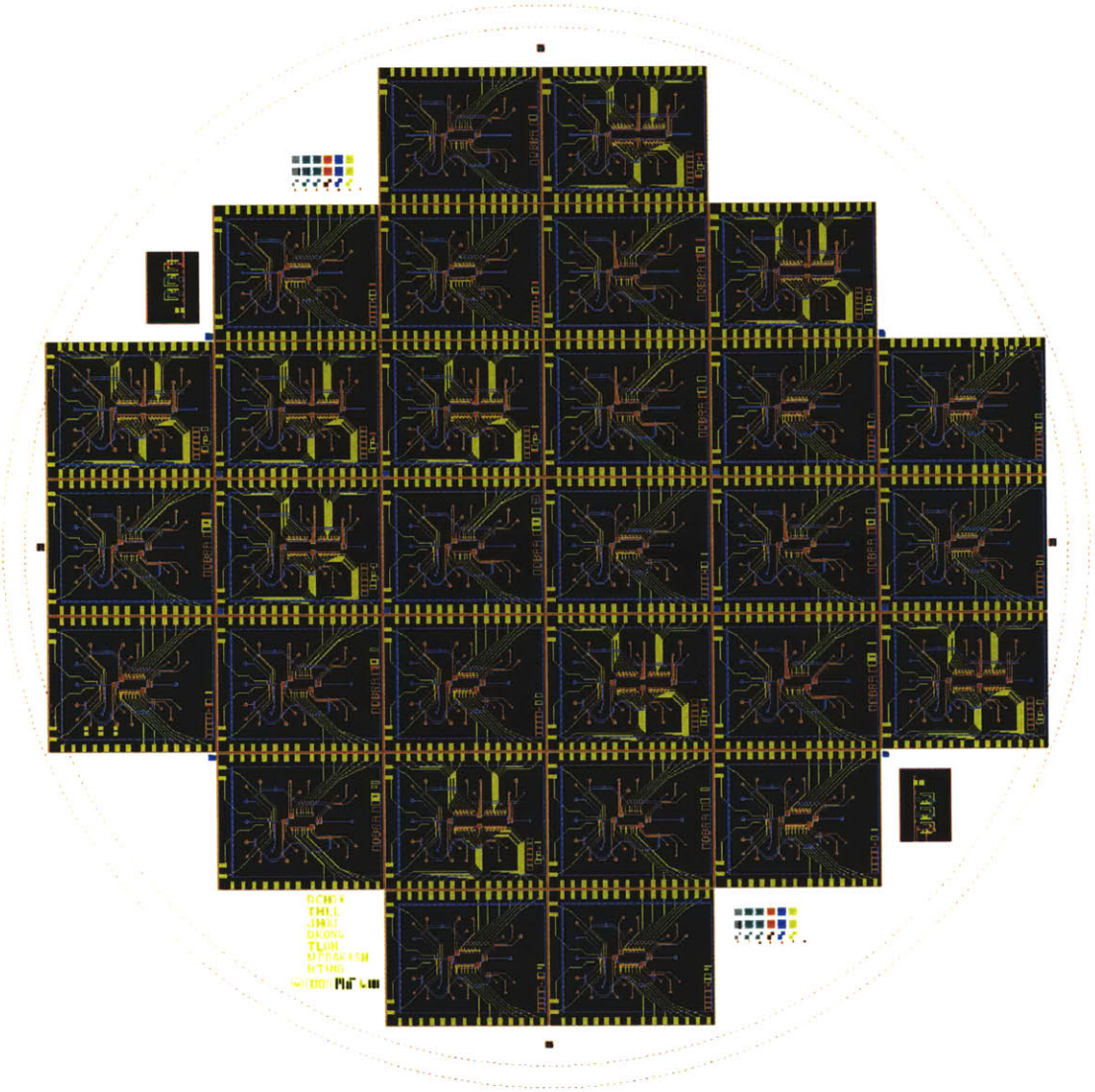

FigureB–25: Device Wafer layout

Appendix C

Matlab Scripts

C.1 Image Processing

C.1.1 acqback.m

```
% ACQBACK - Acquire Background
% Acquires 20 consecutive images and stores the average for background
% noise reduction

% Initialise Variables
CameraID = 0;        % Camera identification number
NumPics = 20;        % Number of consecutive frames acquired
Exposure = 500;      % Exposure time in milliseconds
limits = [0 1299 0 1029];   %[Left Right Up Down] max:[0 1299 0 1029]
temperature = {};    % Leave blank


% Acquire background
%CameraID = CameraInit; %initialise camera
ImageGray = acqimage(CameraID,NumPics,Exposure,limits);
%CameraClose(CameraID); %close camera
ImageGray = mean(ImageGray,3);


% Display and save data
iptsetpref('TruesizeWarning','off')
figure, imagesc(ImageGray), colorbar, truesize, drawnow
title('Background Noise')

save ('backaverage.mat', 'ImageGray', 'temperature')
disp(['File saved: ' pwd '\backaverage.mat' char(10)])

%%%%%%%%%%%%%%%%%%%%%%%%%%%%%%%%%%%%%%%%%%%%%%%%%%%%%%%%%%%%%%%%%%%%%%%%%%%%%%%
```

C.1.2 imfocus.m

```
% IMFOCUS - Displays the image from the CCD
% Press <s> to save image, <esc> to exit script

% Initialise Variables
CameraID = 0;       % Camera identification number
NumPics = 1;        % Number of consecutive frames acquired
Exposure = 30000;       % Exposure time in milliseconds
limits = [0 1299 0 1029];   %[Left Right Up Down] max:[0 1299 0 1029]


h = figure;
%colormap(gray)
colormap(jet)
%iptsetpref('TruesizeWarning','off')
warning off

%CameraID = CameraInit; %initialise camera

while ~ strcmp(get(h,'CurrentCharacter'),char(27))
    ImageGray = acqimage(CameraID,NumPics,Exposure,limits);
    figure(h), imagesc(ImageGray), colorbar, truesize(h), title('CCD Image')
    drawnow

    if strcmp(get(h,'CurrentCharacter'),'s')
        filename = [datestr(now,'yyyymmmdd-HHMMSS') '.mat'];
        save(filename,'ImageGray')
        disp(['File saved: ' filename char(10)])
        set(h,'CurrentCharacter',' ')
    end
end

warning on

%CameraClose(CameraID); %close camera

%%%%%%%%%%%%%%%%%%%%%%%%%%%%%%%%%%%%%%%%%%%%%%%%%%%%%%%%%%%%%%%%%%%%%%%%%%%%%%%%%%%%%%%
```

C.1.3 imcenter.m

```
function ImageCentered = imcenter(ImageInput)

% IMCENTER centers image
% ImageCentered = imcenter(ImageInput,IntensityThreshold,EdgeThresh) centers
% the image matrix input and returns the centered image matrix, ImageCentered
% IntensityTreshhold is the threshold above which a pixel is considered in
% calculations.  The script detects the centers of the channels by the
% maximum intensity (due to the semicircular crossection of the channels)
% across the row or column.


% Initialise variables
xdim = 0;       % x dimensions
ydim = 0;       % y dimensions
center = [0 0]; % Center coordinates: [y x]
edge=[0 0 0 0]; % Center of channel: [up down left right]

yshift = 0;
xshift = 0;
shift = [0 0 0 0;0 0 0 0]; %indexes for shifting [to;from]

[ydim xdim] = size(ImageInput);
center = [round(ydim/2) round(xdim/2)]; %center coordinates
ImageCentered = double(zeros([ydim xdim]));


% Find centers of channels
SumImageRows = sum(ImageInput,2,'double'); %sum each row into a column vector (yshift)
[m,edge(1)] = max(SumImageRows(1:center(1)));   %Up
[m,edge(2)] = max(SumImageRows(center(1):ydim));%Down
edge(2) = edge(2)+center(1)-1;

SumImageCols = sum(ImageInput,1,'double'); %sum each column into a row (xshift)
[m,edge(3)] = max(SumImageCols(1:center(2)));   %Left
[m,edge(4)] = max(SumImageCols(center(2):xdim));%Right
edge(4) = edge(4)+center(2)-1;


% Calculate shift
yshift = center(1) - round((edge(1)+edge(2))/2);
xshift = center(2) - round((edge(3)+edge(4))/2);
shift(1:2,1:2) = CALCULATESHIFT(ydim,yshift); %(to:from,start:end coords)
shift(1:2,3:4) = CALCULATESHIFT(xdim,xshift); %(to:from,start:end coords)
```

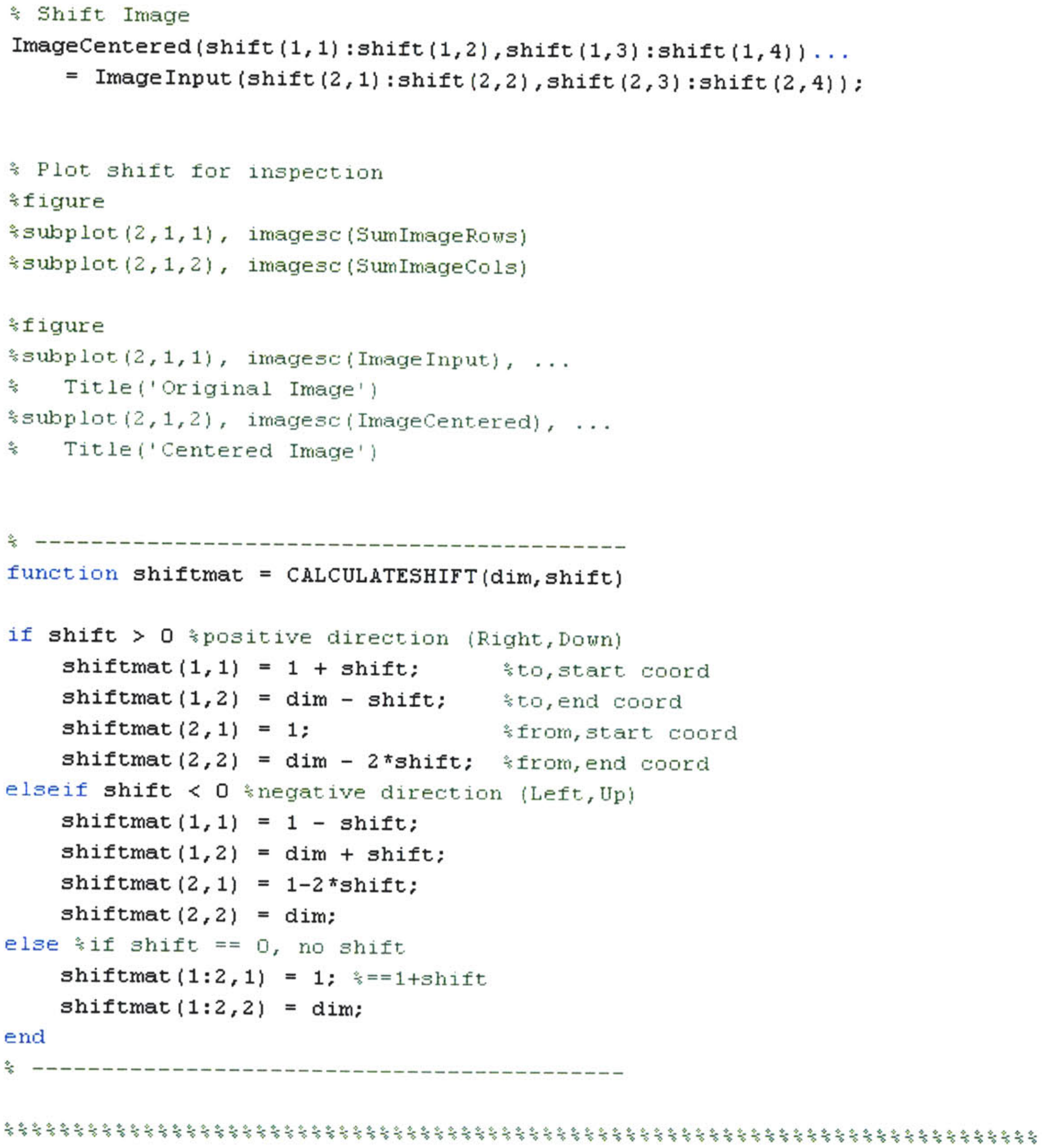

```
% Shift Image
ImageCentered(shift(1,1):shift(1,2),shift(1,3):shift(1,4))...
    = ImageInput(shift(2,1):shift(2,2),shift(2,3):shift(2,4));


% Plot shift for inspection
%figure
%subplot(2,1,1), imagesc(SumImageRows)
%subplot(2,1,2), imagesc(SumImageCols)

%figure
%subplot(2,1,1), imagesc(ImageInput), ...
%   Title('Original Image')
%subplot(2,1,2), imagesc(ImageCentered), ...
%   Title('Centered Image')


% -------------------------------------------
function shiftmat = CALCULATESHIFT(dim,shift)

if shift > 0 %positive direction (Right,Down)
    shiftmat(1,1) = 1 + shift;      %to,start coord
    shiftmat(1,2) = dim - shift;    %to,end coord
    shiftmat(2,1) = 1;              %from,start coord
    shiftmat(2,2) = dim - 2*shift;  %from,end coord
elseif shift < 0 %negative direction (Left,Up)
    shiftmat(1,1) = 1 - shift;
    shiftmat(1,2) = dim + shift;
    shiftmat(2,1) = 1-2*shift;
    shiftmat(2,2) = dim;
else %if shift == 0, no shift
    shiftmat(1:2,1) = 1; %==1+shift
    shiftmat(1:2,2) = dim;
end
% -------------------------------------------

%%%%%%%%%%%%%%%%%%%%%%%%%%%%%%%%%%%%%%%%%%%%%%%%%%%%%%%%%%%%%%%%%%%%%%%%%%%
```

C.1.4 imratio.m

```
% IMRATIO - Loads a reference temperature fluoresence image file and a
% measured temperature fluoresence image file.  It displays an image of the
% ratiometric intensity and calculates the average intensity ratio wrt to
% the reference temperature

clear all

% Initialise Variables
threshold = 150;     % set threshold for calculating average intensity
background = 64.5;   % set background intensity
llimit = 100;            % set boundaries when calculating ratios
rlimit = 1100;       %  make sure to comment out reset below

total = 0;           % total intensity
AverageRatio = 0;    % average intensity calculated
MinRatio = 0;        % minimum intensity
MaxRatio = 0;        % maximum intensity
OriginalDir = pwd;

% Input reference file
[ref_file_in, ref_path_in,FilterIndex] = uigetfile({'*.mat', 'MAT-files (*.mat)'}, ...
    'Open Image MAT-File for Reference Temperature');

if FilterIndex ~= 0 % IF a reference file is input

    cd(ref_path_in)
    [measured_file_in, measured_path_in,FilterIndex] = ...
        uigetfile({'*.mat', 'MAT-files (*.mat)'}, ...
        'Open Image MAT-File for Measured Temperature');


    if FilterIndex ~= 0 % IF a measured file is input

        % Load background noise file
        load([ref_path_in 'backaverage.mat'])
        ImageBack = ImageGray;  % can use background file or average background level

        % Load images and initialise values
        load([ref_path_in ref_file_in])
        ImageGray = double(ImageGray) - ImageBack;
        ReferenceImage = imcenter(ImageGray);
        ReferenceTemperature = temperature;
```

```
load([measured_path_in measured_file_in])
ImageGray = double(ImageGray) - ImageBack;
MeasuredImage = imcenter(ImageGray);
MeasuredTemperature = temperature;

[height,width] = size(MeasuredImage);

clear ImageBack ImageGray temperature  %free up memory
IRDisplay = zeros(height,width);    %for clearer illustration in figure
IRStats = zeros(width*60:1);        %to help reduce memory reallocation


% Reset limits (to scan for the whole image)
%llimit = 1;
%rlimit = width;


% Calculate Intensity Ratio
IntensityRatio = MeasuredImage ./ ReferenceImage;

% Enforce Treshold (replacing for loops with more direct/faster method)
[scanv, scanh] = find(...
    ReferenceImage(:,llimit:rlimit) > threshold); %...
    %& MeasuredImage(:,llimit:rlimit) > threshold);

idx = sub2ind(size(ReferenceImage),scanv,(scanh+llimit)); %convert to linear index

IRStats = reshape(IntensityRatio(idx),1,[]);
IRDisplay(idx) = IntensityRatio(idx);


% Calculate Statistics
n_average = length(IRStats);
AverageRatio = mean(IRStats);
MinRatio = min(IRStats);
MaxRatio = max(IRStats);
StdDev = std(IRStats);
%figure, hist(IRStats,100);
%title(['Ratio Distribution : ' MeasuredTemperature 'C/' ReferenceTemperature 'C' ])
```

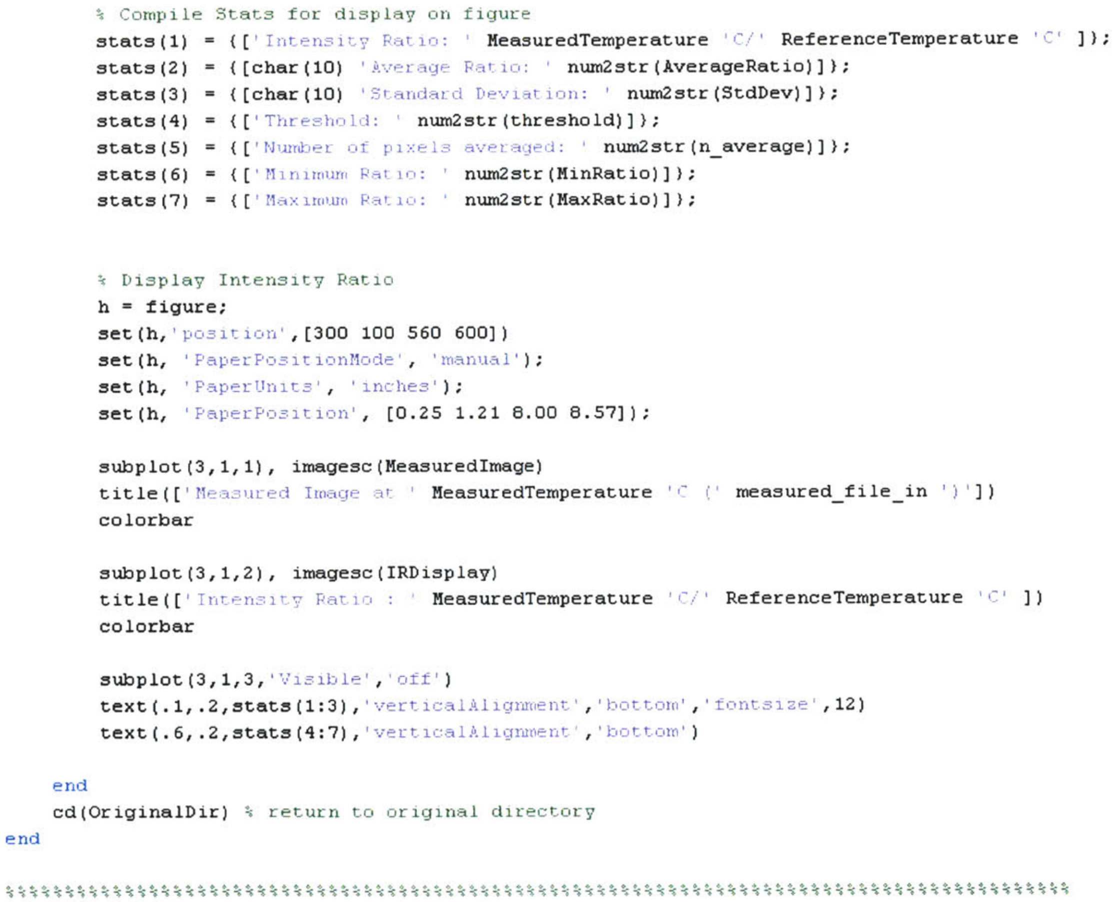

```
        % Compile Stats for display on figure
        stats(1) = {['Intensity Ratio: ' MeasuredTemperature 'C/' ReferenceTemperature 'C' ]};
        stats(2) = {[char(10) 'Average Ratio: ' num2str(AverageRatio)]};
        stats(3) = {[char(10) 'Standard Deviation: ' num2str(StdDev)]};
        stats(4) = {['Threshold: ' num2str(threshold)]};
        stats(5) = {['Number of pixels averaged: ' num2str(n_average)]};
        stats(6) = {['Minimum Ratio: ' num2str(MinRatio)]};
        stats(7) = {['Maximum Ratio: ' num2str(MaxRatio)]};


        % Display Intensity Ratio
        h = figure;
        set(h,'position',[300 100 560 600])
        set(h, 'PaperPositionMode', 'manual');
        set(h, 'PaperUnits', 'inches');
        set(h, 'PaperPosition', [0.25 1.21 8.00 8.57]);

        subplot(3,1,1), imagesc(MeasuredImage)
        title(['Measured Image at ' MeasuredTemperature 'C (' measured_file_in ')'])
        colorbar

        subplot(3,1,2), imagesc(IRDisplay)
        title(['Intensity Ratio : ' MeasuredTemperature 'C/' ReferenceTemperature 'C' ])
        colorbar

        subplot(3,1,3,'Visible','off')
        text(.1,.2,stats(1:3),'verticalAlignment','bottom','fontsize',12)
        text(.6,.2,stats(4:7),'verticalAlignment','bottom')

    end
    cd(OriginalDir) % return to original directory
end

%%%%%%%%%%%%%%%%%%%%%%%%%%%%%%%%%%%%%%%%%%%%%%%%%%%%%%%%%%%%%%%%%%%%%%%%%%%%%%%%%%%%%%%%%
```

C.2 Real-time Spatial Temperature Mapping

C.2.1 acqio.m

```
% ACQIO - Acquire Reference Intensity
% Acquires 20 consecutive images and stores the average for reference image


% Initialise Variables
CameraID = 0;        % Camera identification number
NumPics = 20;        % Number of consecutive frames acquired
Exposure = 500;      % Exposure time in milliseconds
limits = [0 1299 0 1029];   %[Left Right Up Down] max:[0 1299 0 1029]
temperature = 0;


% Acquire background
%CameraID = CameraInit; %initialise camera
ImageGray = acqimage(CameraID,NumPics,Exposure,limits);
%CameraClose(CameraID); %close camera
ImageGray = mean(ImageGray,3);

% Display and save data
iptsetpref('TruesizeWarning','off')
figure, imagesc(ImageGray), colorbar, truesize, drawnow
title('Reference Intensity')

% Input ambient temperature
temperature = str2num(cell2mat(inputdlg( ...
    ['Please input the ambient temperature[C] for this Reference file: '],...
    ['Input Temperature'], 1)));

save ('Ioaverage.mat', 'ImageGray', 'temperature')
disp(['File saved: ' pwd '\Ioaverage.mat' char(10)...
    'Temperature: ' num2str(temperature) char(10)])

%%%%%%%%%%%%%%%%%%%%%%%%%%%%%%%%%%%%%%%%%%%%%%%%%%%%%%%%%%%%%%%%%%%%%%%%%%%%%%%%
```

C.2.2 tmap.m

```
% TMAP - Temperature Mapping
% Displays a temperature map converted from the image aquired from the CCD.
% It takes the average of the frames and find the Intensity Ratio wrt the
% reference image selected.  The Intensity Ratio is converted to a
% temperature map using 'IR2TEMP' or 'TEMPCCURVE'.
% Press <s> to save image, <esc> to exit script

% Initialise Variables
CameraID = 0;        % Camera identification number
NumPics = 1;         % Number of consecutive frames acquired
Exposure = 500;      % Exposure time in milliseconds
limits = [0 1299 0 1029];   %[Left Right Up Down] max:[0 1299 0 1029]
threshold = 100;     % set threshold for intensity

warning('off','MATLAB:divideByZero')
warning off

% Input Reference Image File
[ref_file_in, ref_path_in,FilterIndex] = uigetfile({'*.mat', 'MAT-files (*.mat)'}, ...
    'Load Image MAT-File for Reference Temperature');


if FilterIndex ~= 0 % IF a reference file is input

    % Load background noise
    load([ref_path_in 'backaverage.mat'])
    ImageBack = ImageGray;  % can use background file or average background level

    % Load and initialise Io
    load([ref_path_in ref_file_in])
    Io = double(ImageGray) - ImageBack;
    Io = imcenter(Io);

    clear ImageGray

    % Calculate calibration curve
    CCurve = tempccurve(temperature);

    % Apply threshold
    [scanv, scanh] = find(Io < threshold);
    idx = sub2ind(size(Io),scanv,scanh); %convert to linear index
```

```
    % Initialise figure
    h = figure;
    colormap(tempcolormap(40));
    iptsetpref('TruesizeWarning','off')

%   CameraID = CameraInit; %initialise camera

    while ~ strcmp(get(h,'CurrentCharacter'),char(27))
        % Acquire Image
        It = acqimage(CameraID,NumPics,Exposure,limits) ;
        It = Io;
        It = It - ImageBack;
        It = imcenter(It);

        % Calculate Intensity Ratio
        IRatio = It ./ Io;

        % Convert to Temperature Map using calibration curve
        TempMap = subs(CCurve(2),IRatio);
%       TempMap = ir2temp(IRatio);
        TempMap(idx) = 0;

        % Update Display
        figure(h), image(TempMap), colorbar, title('Temperature Mapping')
        truesize(h), drawnow


        if strcmp(get(h,'CurrentCharacter'),'s')
            filename = [datestr(now,'yyyymmmdd-HHMMSS') '.mat'];
            save(filename,'TempMap')
            disp(['File saved: ' filename char(10)])
            set(h,'CurrentCharacter',' ')
        end
    end

%   CameraClose(CameraID); %close camera
end

warning on

%%%%%%%%%%%%%%%%%%%%%%%%%%%%%%%%%%%%%%%%%%%%%%%%%%%%%%%%%%%%%%%%%%%%%%%%%%%%%%%%
```

C.2.3 tempccurve.m

```
function CCurve = tempccurve(TAmbient)

% TEMPCCURVE - Temperature Calibration Curve
% Scales the initial calibration curve parameters to the ambient
% temperature that the readings are currently being taken in.

% Initialise constants
To = 23.0;  % initial ambient temperature
a = 0.0001; % initial ccurve coefficients
b = -0.0232;
c = 1.4451;

syms T I

f = poly2sym([a b c],T);
%f = sym('0.0001*x^2 - 0.0232*x + 1.4451');

conversioncoef = subs(f,TAmbient);

h = f/conversioncoef;

CCurve = solve(h-I,T);

%%%%%%%%%%%%%%%%%%%%%%%%%%%%%%%%%%%%%%%%%%%%%%%%%%%%%%%%%%%%%%%%%%%%%%%%%%%%%%%%
```

Bibliography

[1] P. Bergveld. Development of an ion-sensitive solid-state device for neurophysiological measurements. *IEEE Transactions on Biomedical Engineering*, 19(70), 1970.

[2] P. Bergveld. Development, operation, and application of the ion-sensitive field-effect transistor as a tool for electrophysiology. *IEEE Transactions on Biomedical Engineering*, 19(342), 1972.

[3] M. A. Burns, B. N. Johnson, S. N. Brahmasandra, K. Handique, J. R. Webster, M. Krishnan, T. S. Sammarco, P. M. Man, D. Jones, D. Heldsinger, C. H. Mastrangelo, and D. T. Burke. An integrated nanoliter dna analysis device. *Science*, 282(5388):484–487, 1998.

[4] H. Chou, M. Unger, and S. R. Quake. A microfabricated rotary pump. *Biomedical Microdevices*, 3(4):323–330, 2001.

[5] B. Chow, T. Hill, J Hou, D. Kong, T. L. Loh, M. Prakash, and B. Tang. *A Realtime Microfluidic PCR Device with Silicon Field-Effect Sensing.* Lab report, 2003.

[6] E. B. Cooper. *Silicon Field-Effect Sensors for Biomolecular Assays.* Thesis, ph.d., Massachusetts Institute of Technology, dept. of electrical engineering and computer science, 2003.

[7] T. M. Finegan. *Remote Three-Dimensional Temperature Sensing Using Planar Laser Induced Fluorescence: Development and Applications to Microwave Heated*

Liquids. Thesis, ph.d., Massachusetts Institute of Technology, dept. of chemical engineering, 2004.

[8] J. Fritz, E. B. Cooper, S. Gaudet, P. K. Sorger, and S. R. Manalis. Electronic detection of dna by its intrinsic molecular charge. *PNAS*, 99(22):14142–14146, 2002.

[9] J. Khandurina, T. E. McKnight, S. C. Jacobson, L. C. Waters, R. S. Foote, and J. M. Ramsey. Integrated system for rapid pcr-based dna analysis in microfluidic devices. *Analytical Chemistry*, 72(13):2995–3000, 2000.

[10] M. U. Kopp, A. J. Mello, and A. Manz. Chemical amplification: Continuous-flow pcr on a chip. *Science*, 280(5366):1046–1048, 1998.

[11] L. J. Kricka and P. Wilding. Microchip pcr. *Analytical and Bioanalytical Chemistry*, 377(5):820–825, 2003.

[12] E. T. Lagally, J. R. Scherer, R. G. Blazej, N. M. Toriello, B. A. Diep, M. Ramchandani, G. F. Sensabaugh, L. W. Riley, and R. A. Mathies. Integrated portable genetic analysis microsystem for pathogen/infectious disease detection. *Analytical Chemistry*, 76(11):3162–3170, 2004.

[13] A. M. Leach, A. R. Wheeler, and R. N. Zare. Flow injection analysis in a microfluidic format. *Analytical Chemistry*, 75(4):967–972, 2003.

[14] J. Liu, M. Enzelberger, and S. Quake. A nanoliter rotary device for polymerase chain reaction. *Electrophoresis*, 23(10):1531–1536, 2002.

[15] D. Ross, M. Gaitan, and L. E. Locasio. Temperature measurement in microfluidic systems using a temperature-dependent fluorescent dye. *Analytical Chemistry*, 73(17):4117–4123, 2001.

[16] P. R. Russo. *Integrated Silicon Field-Effect Sensors and Microfluidics for Biomolecular Detection.* Thesis, m.eng., Massachusetts Institute of Technology, dept. of electrical engineering and computer science, 2004.

[17] P. Scharlin, R. Battino, E. Silla, I. Tunon, and J. L. Pascual-Ahuir. Solubility of gases in water: Correlations between solubility and the number of water molecules in the frist solvation shell. *Pure and Applied Chemistry*, 70(10):1895–1904, 1998.

[18] W. M. Siu and R. S. C. Cobbold. Basic properties of the electrolyte-sio_2-*si* system: Physical and theoretical aspects. *IEEE Transactions on Electron Devices*, ED-26:1805, 1979.

[19] M. A. Unger, H. Chou, T. Thorsen, A. Scherer, and S. R. Quake. Monolithic microfabricated valves and pumps by multilayer soft lithography. *Science*, 288(7):113–116, 2000.